JAERI-M
88-262

STUDY ON THERMO-HYDRAULIC BEHAVIOR DURING REFLOOD PHASE OF A PWR-LOCA

January 1989

Jun SUGIMOTO

日本原子力研究所
Japan Atomic Energy Research Institute

JAERI-Mレポートは，日本原子力研究所が不定期に公刊している研究報告書です。
入手の問合わせは，日本原子力研究所技術情報部情報資料課（〒319-11茨城県那珂郡東海村）あて，お申しこしください。なお，このほかに財団法人原子力弘済会資料センター（〒319-11 茨城県那珂郡東海村日本原子力研究所内）で複写による実費頒布をおこなっております。

JAERI-M reports are issued irregularly.
Inquiries about availability of the reports should be addressed to Information Division Department of Technical Information, Japan Atomic Energy Research Institute, Tokai-mura, Naka-gun, Ibaraki-ken 319-11, Japan.

©Japan Atomic Energy Research Institute, 1988

編集兼発行　日本原子力研究所
印　　刷　いばらき印刷㈱

JAERI-M 88-262

Study on Thermo-hydraulic Behavior during Reflood Phase of a PWR-LOCA

Jun SUGIMOTO

Department of Nuclear Safety Research
Tokai Research Establishment
Japan Atomic Energy Research Institute
Tokai-mura, Naka-gun, Ibaraki-ken

(Received December 7, 1988)

This paper describes thermo-hydraulic behavior during the reflood phase in a postulated large-break loss-of-coolant accident (LOCA) of a PWR. In order to better predict the reflood transient in a nuclear safety analysis specific analytical models have been developed for, saturated film boiling heat transfer in inverted slug flow, the effect of grid spacers on core thermo-hydraulics, overall system thermo-hydraulic behavior, and the thermal response similarity between nuclear fuel rods and simulated rods.

A heat transfer correlation has been newly developed for saturated film boiling based on a 4×4-rod experiment conducted at JAERI. The correlation provides a good agreement with existing experiments except in the vicinity of grid spacer locations.

An analytical model has then been developed addressing the effect of grid spacers. The thermo-hydraulic behavior near the grid spacers was found to be predicted well with this model by considering the break-up of droplets in dispersed flow and water accumulation above the grid spacers in inverted slug flow.

A system analysis code has been developed which couples the one-dimensional core and multi-loop primary system component models. It provides fairly good agreement with system behavior obtained in a large-scale integral reflood experiment with active primary system components.

An analytical model for the radial temperature distribution in a rod has been developed and verified with data from existing experiments. It was found that a nuclear fuel rod has a lower cladding temperature

and an earlier quench time than an electrically heated rod in a typical reflood condition.

Keywords : PWR-LOCA, Reflooding, Thermo-hydraulics, Heat Transfer, Film Boiling, Grid Spacer, Primary System, Simulated Fuel Rod, Thermal Response, Reactor Safety

JAERI－M 88－262

PWRの冷却材喪失事故時再冠水期における熱水力挙動の研究

日本原子力研究所東海研究所原子炉安全工学部
杉本　純

（1988年12月7日受理）

本報告においては，PWRにおける想定事故である大破断冷却材喪失事故（LOCA）時再冠水期における熱水力学的挙動について記述している。原子炉安全解析における再冠水期の熱水力挙動をより良く記述することを目的として，逆スラグ流中の飽和膜沸騰熱伝達，グリッドスペーサの炉心熱水力挙動に及ぼす影響，一次系システム全体の熱水力挙動および核燃料棒と模擬燃料棒の熱的応答の類似性に関し，それぞれ解析モデルを開発した。

原研で行われた4×4本模擬燃料棒実験に基づき，飽和膜沸騰に対する熱伝達相関式を新たに開発した。本相関式による熱伝達率は，グリッドスペーサのごく近傍を除けば，実験データと良く一致することを確かめた。

次に，グリッドスペーサの影響に関する解析モデルを開発した。液滴分散領域における液滴とグリッドスペーサの衝突による分散および逆スラグ流領域におけるグリッドスペーサの上方への蓄水を考慮することにより，グリッドスペーサ近傍の熱水力挙動が良く予測されることが分かった。

炉心と一次系システムのコンポーネントモデルとを結合させることにより，一次系システム挙動解析コードを開発した。本コードは，一次系システムコンポーネントを完備した大規模再冠水実験で得られたシステム挙動を良く予測した。

燃料棒中の半径方向温度分布に関する解析モデルを開発し，既存の実験データを用いてモデルの検証を行った。本解析により，典型的な再冠水条件下では，核燃料棒は実験で用いられる模擬燃料棒に比べ被覆管温度は低く，かつクエンチ時刻も早いことが明らかとなった。

以上，本報告で述べた解析モデルは，今後さらに改良すべき点もあるが，原子炉安全解析の進展に寄与するものと考える。

東海研究所：〒319－11 茨城県那珂郡東海村白方字白根2－4

Contents

目　　次

[Nomenclature]

A	:	Flow area	(m^2)
a	:	Blocking ratio	(-)
C_p	:	Specific heat	(J/kg)
D_e	:	Equivalent hydraulic diameter	(m)
D_h	:	Diameter of holes in upper plenum tie plate	(m)
d	:	Droplet diameter	(m)
d_f	:	Characteristic thickness of fuel	(m)
d_h	:	Thickness of holes in upper plenum tie plate	(m)
d_{SM}	:	Sauter mean diameter ($= \overline{d^3}/\overline{d^2}$)	(m)
E	:	Emissivity	(-)
F_0	:	Fourier number	(-)
g	:	Acceleration of gravity	(m/s^2)
H_{fg}	:	Latent heat of evaporation	(J/kg)
h	:	Heat transfer coefficient	(W/m^2K)
h'	:	Water head	(m)
h_{gap}	:	Gap conductance	(W/m^2K)
K	:	Flow resistance coefficient (K-factor)	(-)
L	:	Wetting perimeter or length	(m)
L_I	:	Horizontal length between downcomer and core	(m)
L_Q	:	Distance from quench front	(m)
M	:	Accumulated mass	(kg)
$\dot{M}$	:	Mass accumulation rate	(kg/s)
N	:	Total number of droplets	(-)
n	:	Average number of droplets after breakup	(-)
P	:	Pressure	(Pa)
P_o	:	System pressure at containment	(Pa)
P_p	:	Peak linear power	(kW/m)
P_{sys}	:	System pressure	(MPa)
Q	:	Heat input into unit volume	(W/m^3)
q	:	Heat generating rate	(kW/m^3)
q_I	:	Heat release rate per unit length from cladding after quenching	(kW/m)
$q_{Gj}^{(t)}$	:	Heat releae rate per unit length from fuel element after quenching at j-th fluid cell	(kW/m)
r	:	Radius	(m)
r_s	:	Gap width of either contact or radiation	(m)

R	:	Thermal resistance	(mK/W)
S	:	Cross-section	(m^2)
T	:	Temperature	(K)
T_o	:	Rewetting temperature	(K)
T_{win}	:	Initial peak clad temperature	(^oC)
t	:	Time	(s)
U, u	:	Velocity	(m/s)
U_{in}	:	Flooding rate	(m/s)
U_o	:	Superficial velocity	(m/s)
V	:	Volume	(m^3)
V_u	:	Volume of upper plenum	(m^3)
v_Q	:	Rewetting velocity	(m/s)
W	:	Mass flow rate	(kg/s)
We_{crit}	:	Critical Weber number	(-)
X	:	Quality	(-)
x	:	Liquid level in downcomer	(m)
y	:	Liquid level in core	(m)
z	:	Distance from upper edge of grid spacer	(m)
z_{GS}	:	Characteristic length for the grid spacer effect in inverted slug flow	(m)
α	:	Void fraction	(-)
δ	:	Wall thickness	(m)
ε	:	Stefan-Boltzmann constant	(W/m^2K^4)
ΔP	:	Differential pressure	(P_a)
ΔT_{sat}	:	Wall superheat	(K)
ΔT_{sub}	:	Inlet subcooling of coolant	(K)
Δt	:	Time step	(s)
ΔU	:	Slip velocity	(m/s)
ΔZ	:	Inclement of elevation	(m)
ΔZ_Q	:	Advanced length of quench front in time step Δt	(m)
λ	:	Thermal conductivity	(W/m K)
η	:	Effective atomization factor	(-)
η_D	:	Downcomer carry-over coefficient	(-)
η_U	:	Upper plenum de-entrainment coefficient	(-)
μ	:	Dynamic viscosity	(Pa.s)
ρ	:	Density	(kg/m^3)
σ	:	Surface tension	(N/m)

τ : Time constant of gradual heat release from rod after quenching (s)

(Subscripts)

A : Downcomer annulas
B : Broken loop
BCN : Broken cold leg nozzle
C : Core
c : Critical, clad
D : Downcomer
ECC : ECC port
ECCLP : ECC injected in lower plenum
FB : Fallback
f : Fluid
g : Gas phase
gap : Gap
h : Hole
I : Inlet (Upper suffix); Intact loop (Lower suffix)
i : i-th intact loop or i-th node
j : j-th fluid cell
L : Primary loop
LP : Lower plenum
ℓ : Liquid phase
max : Maximum
n : time at t
n+1 : time at $t + \Delta t$
N : After quenching
O : Outlet (Upper suffix); Before quenching (Lower suffix)
Q : Quenching
Q^1 : Before quenching
Q^2 : After quenching
R : Radiative
S : System
sat : Saturation
TP : Tie-plate
U : Upper plenum
w : Spacer wall or clad wall
1 : Below grid spacer
2 : Above grid spacer

1. Introduction

1.1 LOCA sequence and reflood behavior

To mitigate the effects of a loss-of-coolant accident (LOCA) in a light water reactor, the reactor is equipped with an emergency core cooling system (ECCS). The ECCS is designed to inject emergency core cooling (ECC) water into the reactor pressure vessel to prevent overheating of the core due to decay heat. The effectiveness of ECCS in a LOCA situation has long been a nuclear safety concern.

Figure 1.1 illustrates the typical LOCA sequence for a pressurized water reactor (PWR)[1]. It is assumed that the accident is caused by a double-ended sudden rupture of the primary loop piping (Large-break LOCA), the most severe case in safety analysis.

In the "blowdown" period shown in Fig. 1.1, the pressure of the primary system decreases rapidly after the accident due to the rapid loss of coolant from the break location. This depressurization simultaneously causes the flashing of water into steam in the primary system.

The ECCS for PWRs consists of a high pressure injection system (HPIS), an accumulator and a low pressure injection system (LPIS). These three independent subsystems are designed to inject ECC water into the pressure vessel when preset pressure values are reached during a LOCA transient. It is assumed that because of system depressurization, ECC water injected during the blowdown period easily bypasses the reactor vessel and flows to the break location.

In the "refill" period shown in Fig. 1.1, after the system has depressurized, the ECC water begins to accumulate in the bottom of the pressure vessel. This is because the steam flow generated by flashing is too low to prevent the ECC water from flowing down the downcomer.

When the water level reaches the bottom of the core, the "reflood" phase begins in the LOCA transient. As shown in Fig. 1.1, the expected cladding temperature at a given elevation gradually increases after the reflood initiation due to decay heat. However the increase is less than during refill because some core cooling is accomplished through flowing steam which contains entrained water droplets. As the reflood process advances, the cladding temperature

reaches a peak value (turnaround point). The cladding temperature then gradually decreases until the time of quench when the cladding is quickly cooled to the saturation temperature.

The reflood phenomena can thus be characterized by high temperature, low pressure and low inlet water velocity compared with the preceding blowdown and refill phenomena. The reflood transient can be regarded as nearly quasi-steady state, except in the vicinity of the quench front where the stored energy is rapidly removed from the fuel cladding. The reflood thermo-hydraulic behavior, however, is so complicated especially in the core region and contains an element of negative feedback in the primary system.

In a reactor safety analysis, one of the most important items is to evaluate the peak cladding temperature during the reflood phase of the LOCA. This is because the fuel cladding is the inner (first) boundary to prevent the release of the fission products to the public. The cladding material is chemically and mechanically vulnerable at high temperature. The ECCS evaluation guideline[2] used for a licensing safety analysis requires that the peak cladding temperature not exceed 1200°C in LOCA situation.

1.2 Previous work and specific items to be discussed

A number of experimental programs have been conducted to investigate thermo-hydraulic behavior during reflood. A series of FLECHT (Full Length Emergency Core Heat Transfer) experiments[3]-[5] was one systematic effort with full length simulated fuel rod bundle. In the licensing analysis for a PWR, the correlations obtained from FLECHT are used for the conservative prediction of quench front elevation, carry-over ratio and heat transfer coefficient. Similar experiments were conducted in Semiscale[6] at Idaho National Engineering Laboratory (INEL), FEBA (Flooding Experiments with Blocked Arrays) experiment[7] in West Germany and at the Japan Atomic Energy Research Institute (JAERI)[8]-[10].

Numerous improvements in experimental techniques have also been accomplished. For example, the author conducted a thermocouple attachment experiment[11] to select a proper attachment method for evaluating temperature behavior during typical reflood conditions.

The selected method has been adopted in large scale reflood tests[10] with about 2,000 rods conducted at JAERI.

A number of analytical models have also been proposed over the years for the quenching mechanism[12], hydraulic behavior[13] and the heat transfer coefficient[14]. Some of them are implemented in the analytical codes used to evaluate thermo-hydraulic behavior during the reflood phase. The TRAC code[15] developed at the Los Alamos National Laboratory (LANL), for example, incorporates a set of heat transfer correlations to predict the entire LOCA behavior using a three-dimensional scheme in the core region. The REFLA code[16] developed at JAERI utilizes thermo-hydraulic correlations for quench velocity, void fraction and film boiling heat transfer based on FLECHT and experiments conducted at JAERI.

The core thermo-hydraulic models used in the TRAC code have been assessed by large scale reflood tests conducted at JAERI by the author[17][18]. The effects of initial cladding temperature on the reflood phenomena were experimentally and analytically studied by the author et al. using the TRAC and REFLA codes[19].

The followings are four specific items discussed in this paper:

(1) Saturated film boiling heat transfer

Figure 1.2 shows the core flow model assumed in the reflood analysis code REFLA[16]. A set of thermo-hydraulic correlations in each flow region and a model of the quench front propagation are implemented in the code. The transition flow region shown in Fig. 1.2 is characterized by saturated water surrounded by an unquenched wall. The slip velocity between vapor and liquid in this region is not large enough to generate and entrain water droplets moving upwards. Since the liquid is considered to be supported by the vapor film on the wall of the flow channel, the heat transfer mechanism in this transition region is similar to film boiling heat transfer.

In this study, this transition region is therefore called the "saturated film boiling" region, or "inverted slug flow" region when the flow pattern is addressed. It is noted that what is called "inverted annular" flow is a case with much lower void fraction than with the inverted slug flow.

Some work has been devoted to develop heat transfer models for the saturated film boiling region expected during reflood. Empirical

heat transfer correlations have been developed with single tube experiments[20], bundle experiments[21] and PWR-FLECHT data[22]. It is important to precisely evaluate saturated film boiling heat transfer, since this flow region is dominant in space and time during a reflood transient. The developed heat transfer scoefficients, however, have not been satisfactory for predicting peak cladding temperatures.

(2) Effect of grid spacers on core thermo-hydraulics

As shown in Fig. 1.3, the position of fuel rods in a light water reactor core fuel bundle is maintained by grid spacers. Under reflood conditions these grid spacers are postulated to act as flow disturbers and heat sinks[23]. It is expected that heat transfer will then be enhanced downstream from the grid spacers and this should result in lower peak cladding temperatures.

In FLECHT and FEBA experiments, the heat transfer enhancement due to grid spacers has been observed in the droplet dispersed flow region. Lee et al.[24] measured the distribution of water droplet diameter near the grid spacers in the air-water flow condition. Heat transfer enhancement and water accumulation above grid spacers have also been observed in the inverted slug flow region by the author et al.[19]

In these experiments, the governing mechanism of the grid spacer effect has not been fully identified, mainly due to the lack of detailed thermo-hydraulic information near grid spacers in a typical reflood condition.

(3) Thermo-hydraulic behavior in primary system

A schematic of the LOCA thermo-hydraulic behavior in the primary system is illustrated in Fig. 1.4. As indicated in the figure, the core flooding rate, which significantly affects core cooling[3][8], is controlled by the balance between the driving head of the downcomer and the back-pressure in the upper plenum. The driving head of the downcomer forces the water into the core, whereas the back-pressure tends to retard the core flooding rate. The back-pressure, maintained mostly by the pressure drop at the pump, is enhanced by the vaporization of droplets in the steam generator tubes. This vaporization is due to a much higher temperature on the secondary side

than the saturation temperature of the primary side during reflood. This enhanced back-pressure effect, called "steam binding", is a unique peculiarity of a PWR-LOCA compared to a BWR-LOCA because a BWR has no steam generator.

The integral system tests conducted with the Cylindrical Core Test Facility (CCTF) at JAERI produced rather simple thermo-hydraulic characteristics in the primary system[10]. The main pressure drop in the primary loop is at the pump location where mostly single-phase vapor is flowing and system responses can be regarded as nearly quasi-steady state. This simple situation makes it easy to construct system component and flow models, and then to couple those models with the core thermo-hydraulic model for the analysis of the overall system thermo-hydraulic behavior.

(4) Thermal response similarity between simulated heated rods and nuclear fuel rods

In most LOCA experiments, electrically heated rods are used for simulating fuel rods. As shown in Fig. 1.5, a nuclear fuel rod (for current PWRs and BWRs) has a gap between the Zircaloy cladding and the fuel pellets. An electrically heated rod consists of non-Zircaloy cladding, heater element and insulator and has no gap. The rod geometry and physical properties of the materials used are thus considerably different between electrically heated and nuclear fuel rods. The typicality of non-nuclear rods is therefore a concern for the safety evaluation of reactors when applying experimental results to a nuclear reactor.

There are a limited number of works on the typicality of a simulated heated rod in a typical reflood transient condition[25]-[28]. In addition, little attention has been paid to the coupling between experiments and analysis.

1.3 Objective of this study

The objective of this study is to clarify the characteristics of the thermo-hydraulic behavior, both in the core and the other portions of the primary system, during the reflood phase of a PWR-LOCA. For better prediction of the reflood transient in a nuclear safety

analysis, the following items discussed above, are investigated in this study:

(1) Characteristics of saturated film boiling heat transfer in the core region

(2) Effect of grid spacers on core thermo-hydraulics

(3) Characteristics of the thermo-hydraulic behavior in the primary system

(4) Thermal response similarity between a nuclear fuel rod and a simulated heated rod

In order to achieve this objective, an analytical model for each item was developed based on the physical understanding of the reflood phenomena or simple model experiments. The model developed was then compared with bundle or integral experiments for evaluation of the model.

The specific thermo-hydraulic items investigated, (1) through (4) above, are presented in detail in chapters 2 through 5, respectively. The conclusions of this study are given in chapter 6.

References

(1) Ohi nuclear power plant, Application form of reactor installation permission, Kansai Electric Power Co.(in Japanese)(1986).
(2) Examination Guides on Reactor Safety Evaluation, Scientific and Technology Agency of Japan (in Japanese).
(3) Cadek, F.F., et al.: WCAP-7665, (1971).
(4) Waring, J.P., et al.: WCAP-8583, (1975).
(5) Lee, N., et al.: WCAP-9891 (1981).
(6) Peterson, A.C., et al.: TREE-NUREG-1001 (1976).
(7) Ihle, P., et al.: Presented at Int. Mtg. on Thermal Nuclear Reactor Safety, Chicago (1982).
(8) Murao, Y., et al.: JAERI-M 6982 (in Japanese)(1977).
(9) Sugimoto, J., et al.: JAERI-M 8169 (in Japanese)(1979).
(10) Murao, Y., et al.: JAERI-M 82-073 (1982).
(11) Sugimoto, J.: JAERI-M 985 (in Japanees)(1977).
(12) Murao, Y.: J. Nucl. Sci. Technol., 14[12], 875-885 (1978).
(13) Murao, Y. and Iguchi, T.: J. Nucl. Sci. Technol. 19[8], 613-627 (1982).
(14) Murao, Y. and Sugimoto, J.: J. Nucl. Sci. Technol., 18[4], 275-284 (1981).
(15) Liles, D., et al.: LA-8709-MS, NUREG/XR-2054, (1981).
(16) Murao, Y.: J. Nucl. Sci. Technol., 16[11], 802-817, (1979).
(17) Sugimoto, J.: LA-8471-MS, NUREG/CR-1991, (1981).
(18) Sugimoto, J.: JAERI-M 82-166, (1982).
(19) Sugimoto, J. and Murao, Y.: J. Nucl. Sci. Technol., 20[8], 645-657 (1983).
(20) Yu, K.P. and Yadigaroglu, G.: ASME paper 79-HT-48, ASME/AICHE 18th National Heat Transfer Conf., San Diego, (1979).
(21) Sudo, Y.: J. Nucl. Sci. Technol., 17[7], 516-530 (1980).
(22) Yeh, H.C., et al.: Nucl. Technol., 46 [MID-DEC. 1979), (1979).
(23) Yao, Y., et al.: ASME paper 80-WA/HI-62, (1980).
(24) Lee, S.L., et al.: Presented at 10th Water Reactor Safety Information Mtg., Gaithersburg, (1982).
(25) Piggott, B.D.G., et al.: Nucl. Eng. Des., 41, 165-173 (1977).
(26) Dhir, V.K., et al.: EPRI-NP-1277, (1979).
(27) Nishida, M.: KfK 3786B, (1984).
(28) Ihle, P., et al.: Presented at 1st Int. Workshop on Fundamental Aspects of Post-dryout Heat Transfer, Salt Lake City, (1984).

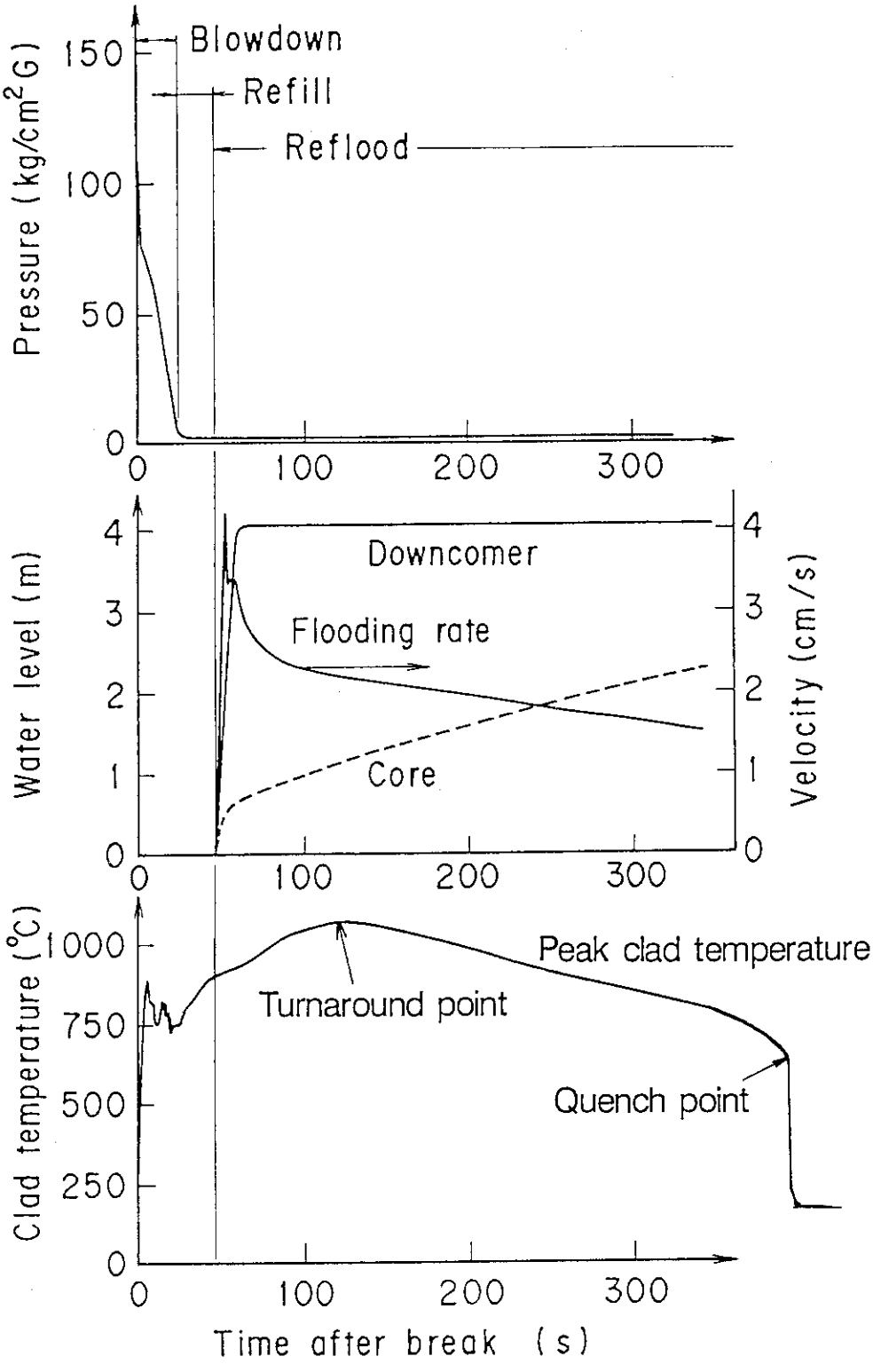

Fig. 1.1 Typical LOCA sequence for PWRs[1]

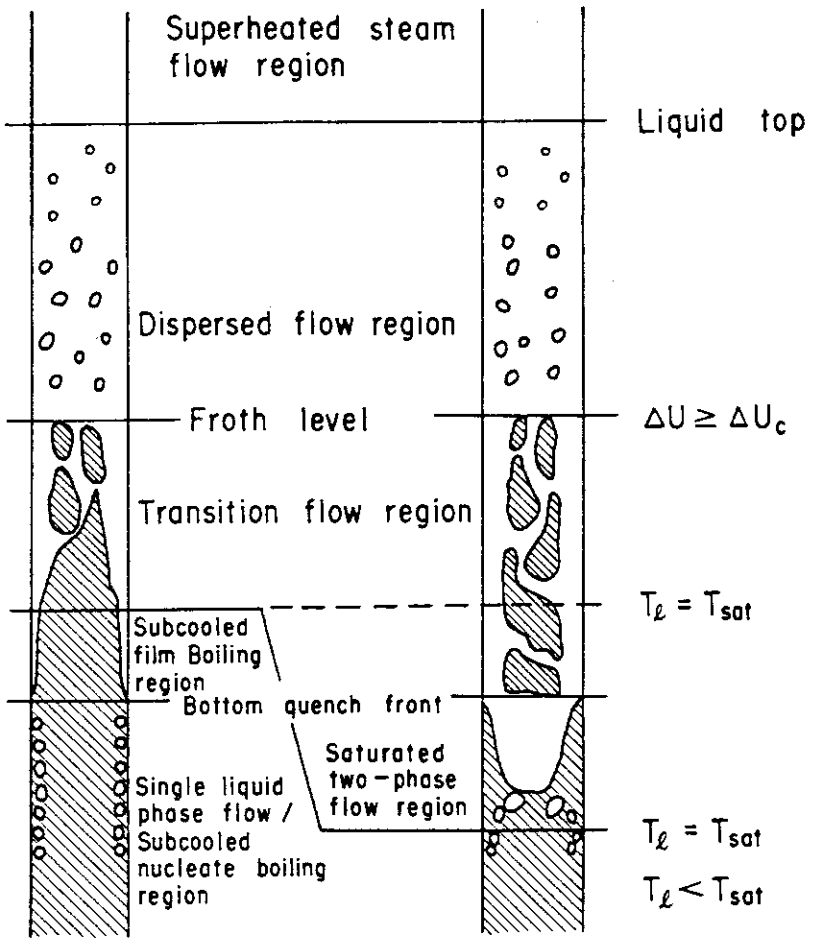

Fig. 1.2 Flow model assumed in REFLA code[16]

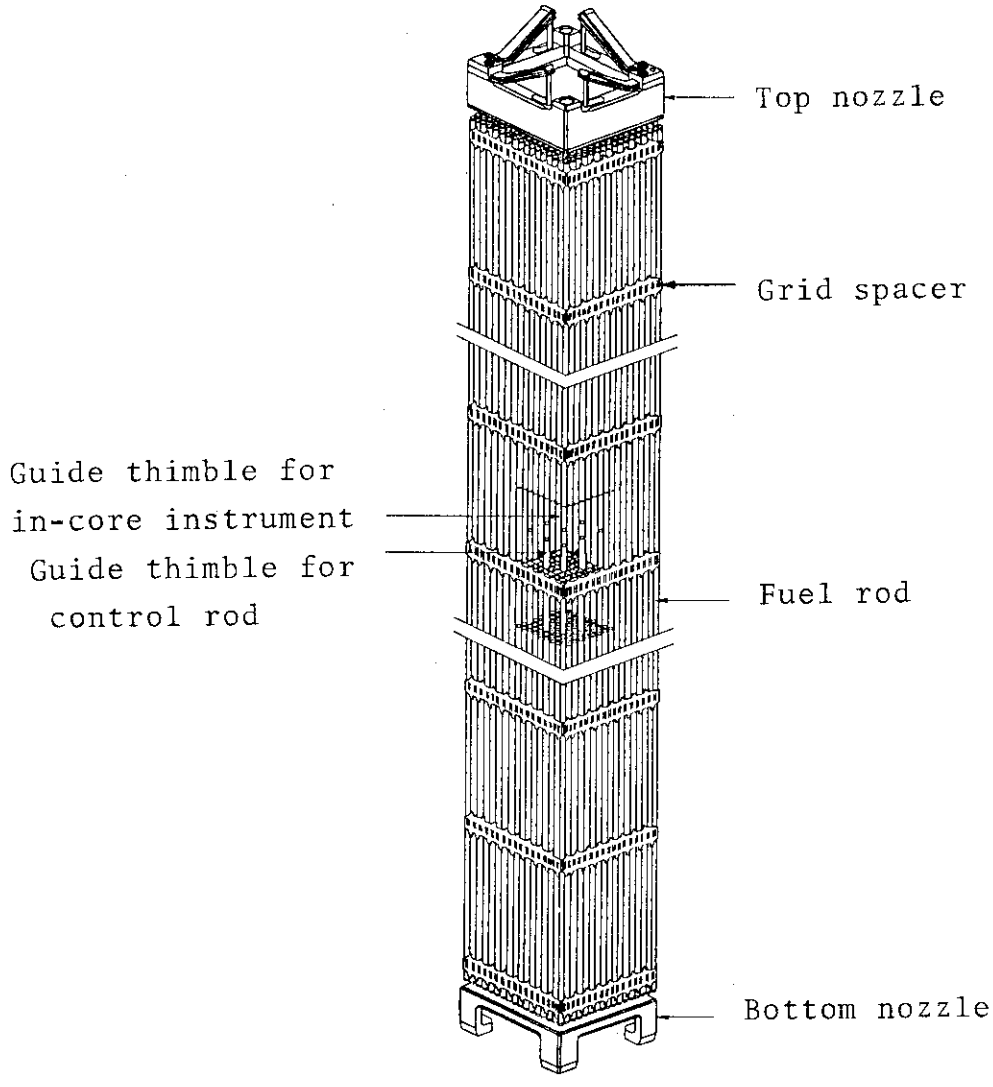

Fig. 1.3 Typical fuel rod bundle used in PWR[1]

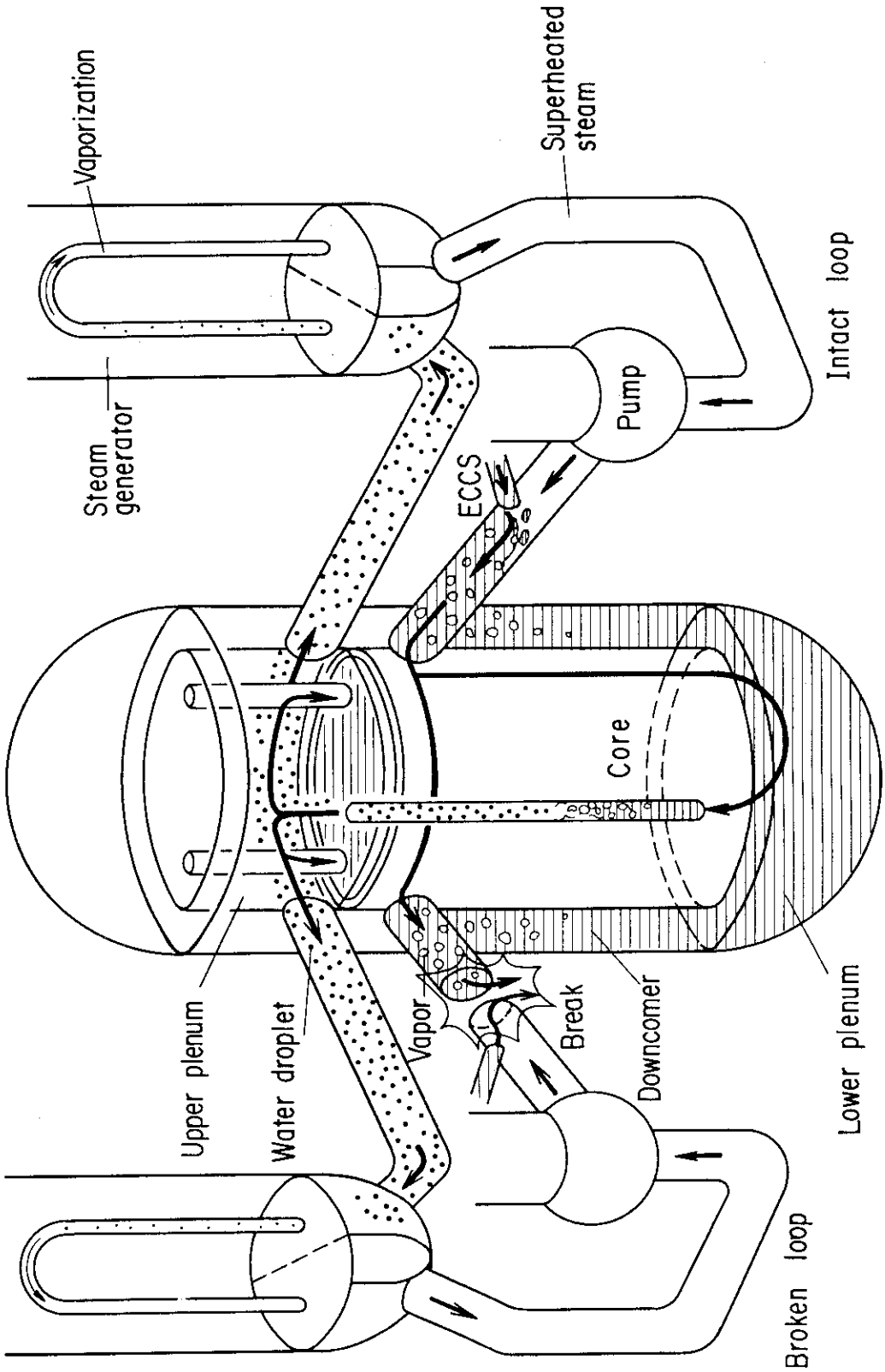

Fig. 1.4 Schematic of thermo-hydraulic behavior in primary system during reflood

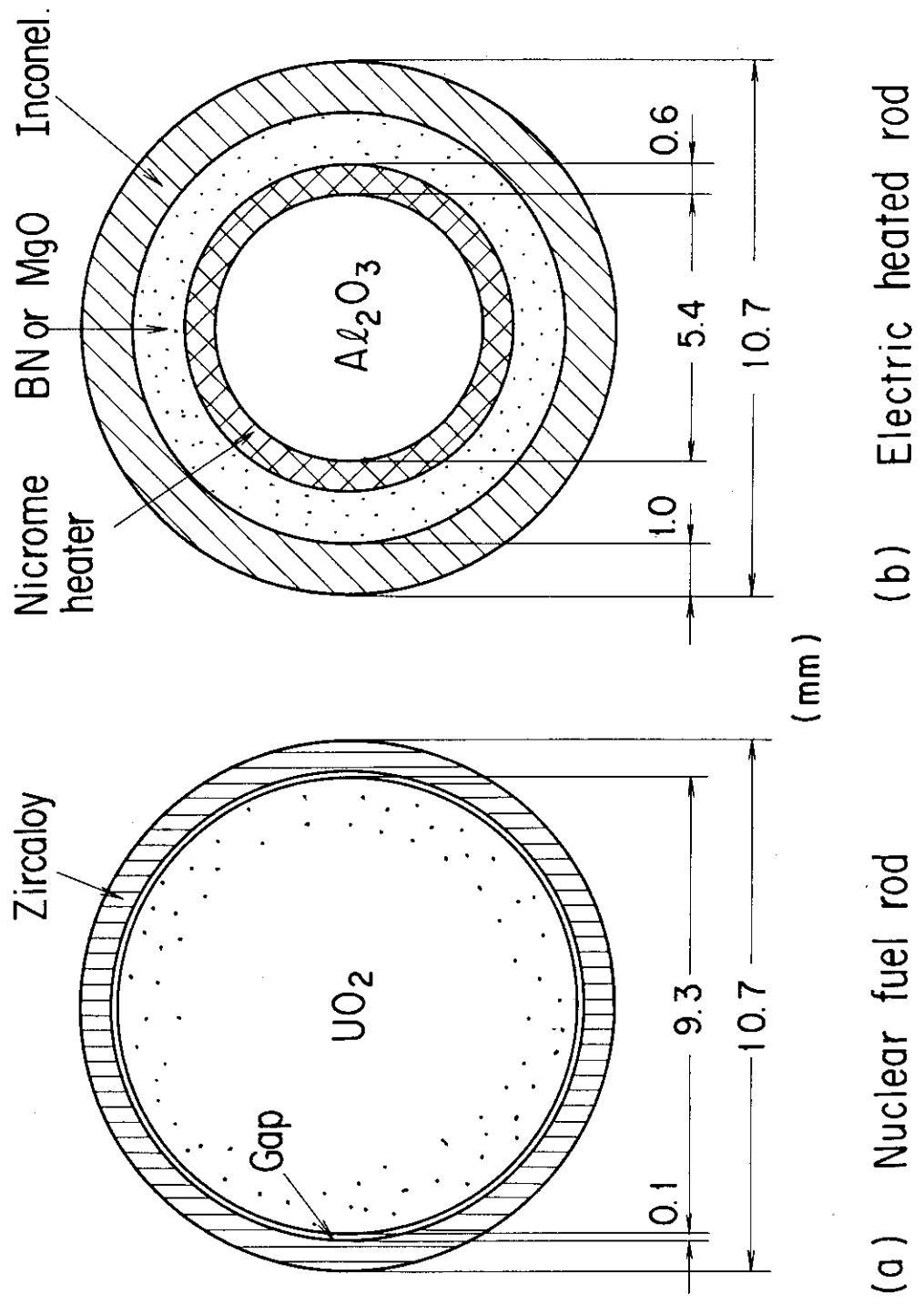

Fig. 1.5 Comparison between nuclear fuel rod and electrically heated rod

2. Correlation of Saturated Film Boiling Heat Transfer[1][12]

2.1 Introduction

A saturated film boiling or a transition flow region shown in Fig. 1.2 is characterized by saturated water surrounded by the unquenched wall. The slip velocity between vapor and liquid in this region is not large enough to generate water droplets upwards in the core subchannel. Since the liquid is considered to be supported with the vapor film on the wall of the flow channel, the heat transfer mechanism in this region would be similar to that of a film boiling region.

From a point of nuclear safety analysis, it is important to predict the saturated film boiling heat transfer coefficient with enough accuracy. This is because that this region is predominant in space and time during reflood transient. The predictability of the heat transfer coefficient, however, has not been satisfactory in evaluating the peak clad temperature.

In the present paper, the heat transfer coefficient h is defined as

$$h = q / \Delta T_{sat} \qquad (2\text{-}1)$$

where q is the heat flux and ΔT_{sat} is the superheat of heated rod. In evaluating the superheat ΔT_{sat}, the saturation temperature is used for fluid ($\Delta T_{sat} = T_w - T_{sat}$).

The followings are the critical review by Murao[1] for the previous work concerning the heat transfer coefficient in a typical reflood condition:

Clement et al.[2] concluded that none of the correlations using an instability wave length gave good prediction from ERSEC experiments and analysis. Uging the wave length as the distance from the quench front, they have obtained the best fit for the local Bromley type correlation. It was shown that the heat transfer coefficient decreases as quality increases and the measured factor of the Bromley type correlation was in the scattered range from 1.0 to 0.5. Ellion's correlation[3] and the modified Bromley's correlation were also found in the scattered range.

In the heat transfer model of the CLADFLOOD code[4], the heat transfer coefficient for the transition flow region is calculated using a modified form of Ellion's correlation:

$$h = 0.537[\lambda_g^3 \rho_g \rho_\ell H_{fg} g/L_Q \mu_g \Delta T_{sat}]^{1/4} (1/X)^{2.07\sqrt{U_{in}}} , \qquad (2\text{-}2)$$

where L_Q is the distance from the quench front and X the quality. The modification was made based on PWR-FLECHT experiment[5] and the code was successfully applied to other PWR-FLECHT experiments.

Based on a single tube reflooding experiment conducted at the University of California-Berkeley, Yu & Yadigaroglu[6] developed a correlation for the heat transfer immediately downstream of the quench front as follows:

$$h = h_Q \exp(-\alpha L_Q) , \qquad (2\text{-}3)$$

where h_Q and α are functions of flooding rate, quench front velocity and local quality.

An empirical reflood heat transfer correlation[7], called FLECHT correlation, was developed by using the PWR-FLECHT data based on upward flooding experiments. For the quasi-steady period, the following correlation was derived:

$$h = 261.2\ [1-\exp(-9.84U_{in})]\ 0.714+0.286[1-\exp(-0.16843P/U_{in}^2)]$$

$$+ 215.9\exp(-5.9U_{in})\exp(-3.937L_Q) . \qquad (2\text{-}4)$$

Sudo[8] developed an empirical correlation for the heat transfer coefficient of the saturated and subcooled film boiling regimes under the simulated reflood conditions. The correlation is written as

$$h = h_{sat}(1 + 0.025\Delta T_{sub}) + 3/4h_R , \qquad (2\text{-}5)$$

where

$$h_{sat} = 0.94[\lambda_g^3 \rho_g (\rho_\ell - \rho_g) H'_{fg} g/L_Q \nu_g \Delta T_{sat}]^{1/4} , \qquad (2\text{-}6)$$

$$h_R = \varepsilon E (T_w^4 - T_{sat}^4)/\Delta T_{sat} ,$$

$$H'_{fg} = H_{fg}[1 + 0.4C_p \Delta T_{sat}/H_{fg}]^2 ,$$

and L_Q is the distance from the quench front. This correlation for the saturated film boiling is similar to Ellion's correlation except for the factor 0.94 and the use of H_{fg}. Equation (2-6) predicted h_{sat} well for the case of high flooding rate, but not satisfactory for the case of low flooding rate.

In the present chapter described are the reflood experiment conducted at JAERI, a new heat transfer correlation developed with this experiment, and the evaluation results of the proposed correlation. In the derivation of the present correlation, consideration was paid for the use of local parameters at the point of interest (e.g. local void fraction) rather than the macroscopic parameters (e.g. core inlet liquid velocity). This is for the wider and more flexible use of the correlation from a point of safety analysis of the reactor.

2.2 Experiment

(1) Test apparatus

The experimental apparatus, called a JAERI's small scale reflood test facility, is designed to investigate the thermo-hydraulic behavior during reflood[9]. The experimental apparatus shown in Fig. 2.1 consists of a test section housing with a 4x4 rod bundle, an upper plenum with a water separator, a lower plenum, a coolant injection system and additional supporting systems. The core flow area is about 1/2,100 scale of a 1,000 MWe class PWR.

In the test section, a full length, electrically heated 16-rod Inconel-600-clad bundle is mounted with egg-crate type grid spacers in a square lattice. A chopped-cosine axial power profile approximated with a step-wise function and a flat radial power profile are used. The axial peaking factor is 1.66. The total power was kept constant during the test. The heated rods were designed for a maximum temperature of 1,200°C using boron nitride insulation. In Table 2.1, the main specifications of the test facility are listed.

Instrumentation of the experiment includes numerous thermocouples buried in grooves on the outside surface of the heater-rod cladding[10], fluid temperature thermocouples, flow meters, differential pressure transducers and supplied power to the rods. The

signals from the detectors are recorded on a digital magnetic tape for data reduction by a computer.

The test procedure is as follows: The rod bundle and its housing are preheated to the desired initial temperature. The reflooding is initiated by injecting the water into the test section. The relevant parameters of the present experiments are listed in Table 2.2. The parametric effect tests were run basically with one parameter varied from the base case conditions.

(2) Data evaluation

The heat transfer coefficient is evaluated with HETRAP code[11] using the clad surface temperature transient of the heated rods and supplied electrical power. The void fraction is evaluated from the differential pressure measurement assuming the frictionless flow in the central steam core and a linear void distribution. The quench front propagation is evaluated with measured quench times by a linear interpolation.

Figure 2.2 shows an example of evaluated void fraction. Shown in the figure are the location of the differential pressure (DP cells measurement), elevations of the thermocouples (T/Cs) and axial power distribution.

Figure 2.3 shows an example of the quench front propagation. The quench front propagates rapidly near the bottom and top of the core, while the quench front propagates slowly and almost constantly at the elevations through T/Cs 2 to 5. Since the quench velocity changes discontinuously near T/Cs 2 and 5 locations, the data from T/Cs 3U through 4L elevations were used for the present study.

(3) Heat transfer characteristics

Figure 2.4 shows the heat transfer coefficient and void fraction at 4L (1.5 m from the bottom) elevation, and the distance from the quench front. As shown in the figure, the heat transfer coefficient h closely depends on the distance from the quench front L_Q. The h increases with decreasing L_Q from 0 - 40s, and h gradually increases with gradual decrease of L_Q between 40 to -150s, and finaly h sharply increases when L_Q reaches zero (i.e. near quench point) at 160s. This suggests that the heat transfer coefficient h before the quenching would be mainly affected by the term,

$$h_{sat} \propto L_Q^{-a} \quad , \quad a > 0 \ . \tag{2-7}$$

From the observation of the void fraction, the followings are found:

a) The heat transfer coefficient h is nearly zero between 0 to 20s when the flow can be assumed to be a single phase vapor ($\alpha \sim 1$)

b) The h sharply increases between ~20 to ~30s when α sharply decreases i.e. the water fraction ($1 - \alpha$) sharply increases.

c) The h gradually increases between ~30 to ~160s when ($1 - \alpha$) gradually increases,

All these show that the heat transfer coefficient h is also closely related to ($1 - \alpha$) before the quenching.

The flow pattern suggested by the void fraction is classified into three major parts; a single phase vapor, a dispersed flow with water droplets, and a transition flow with water slugs. These three regions almost correspond to above a), b) and c), respectively. It is noted that the regions a) and b) last only short and the region c) is predominant in space and time during reflood, and also the peak clad temperature usually realizes in this third region.

Figure 2.5 shows the effect of the clad temperature on the heat transfer coefficient. Shown in the figure are the initial clad temperature To at the reflood initiation and the turnaround temperature Tmax. The heat transfer coefficient is slightly higher with higher clad temperature from 0 to 160s of the transient. This is explained by the radiative heat transfer h_R expressed with well-known formula,

$$h_R \propto \frac{T_w^4 - T_{sat}^4}{T_w - T_{sat}} \tag{2-8}$$

In the range of the present experiment, however, the effect of radiative term h_R is not dominant compared with the term shown in Eq. (2-7).

2.3 Heat transfer correlation[12]

Based on the above experiment conducted at JAERI, a new heat

transfer correlation has been developed for the saturated film boiling region by the author. The measured or evaluated parameters such as the heat transfer coefficient, void fraction, and the location of quench front were utilized for the derivation and the evaluation of the correlation.

In the previous section, it is shown that the heat transfer coefficient in the saturated film boiling region is primarily affected by the distance from the quench front with the secondary effect of void fractin and clad temperature. At the first step, the heat transfer coefficient h is assumed to be expressed as the sum of the Bromley-type convective film boiling heat transfer and the radiative heat transfer;

$$h = (1 - \alpha)^{a} h_{sat} + (1 - \alpha)^{b} h_{R} \qquad (2\text{-}9)$$

where α is the void fraction, h_{sat} the convective heat transfer coefficient, h_R the radiative heat transfer coefficient.

In Eq. (2-9) the saturation convective heat transfer coefficient h_{sat} and radiative heat transfer h_R are assumed to be expressed as,

$$h_{sat} = 0.94[\lambda_g^{3} \rho_g \rho_\ell H_{fg} g / L_Q \mu_g \Delta T_{sat}]^{1/4} \quad , \qquad (2\text{-}10)$$

$$h_R = \varepsilon E (T_w^{4} - T_{sat}^{4}) / (T_w - T_{sat}) \quad , \qquad (2\text{-}11)$$

respectively, considering the smooth transition from Eq. (2-9) to Sudo's correlation, Eq. (2-5), when both the subcooling ΔT_{sub} and void fraction α decrease to zero.

When the void fraction α increases near unity, on the contrary, the heat transfer coefficient h in Eq. (2-9) decreases to zero. In this case the convective heat transfer in a single phase superheated vapor flow should alternatively be evaluated with conventional correlation. In reality, when the void fraction increases to unity, the flow pattern should change from inverted slug flow to dispersed flow as illustrated in Fig. 1.2. The heat transfer transition is therefore considered to be continuous when increased to unity.

It should be noted that the void fraction in the typical reflood transient before quenching is in the range from about 0.7 to 0.9. Also

the experiments, which the present correlation depends upon, were conducted with the pressure in the range from 0.1 to 0.4 MPa and with the core inlet velocity from 1.4 to 7.5 cm/s. For the practical use in the reactor safely analysis, the predictability of the heat transfer correlation is important.

At the second step, the tentative exponents a and b in Eq. (2-9) are to be determined using some experimental data. It is assumed that Eq. (2-9) holds at two different time steps t_1 and t_2, i.e.,

$$\left.\begin{aligned} h_1 &= (1-\alpha_1)^a h_{sat1} + (1-\alpha_1)^b h_{R1} , \\ h_2 &= (1-\alpha_2)^a h_{sat2} + (1-\alpha_2)^b H_{R2} , \end{aligned}\right\} \qquad (2\text{-}12)$$

where sufixes 1 and 2 denote the times at t_1 and t_2, respectively.

A set of Eq. (2-12) is solvable concerning the two unknown parameters of a and b. Figure 2.6 shows such an example of numerically solved sets of (a, b) with automatically shifted time increment for the measered heat transfer coefficient history. It is noted that the void fraction α and the location of quench front L_Q at each time step were evaluated with the differential pressure measurement and the clad temperature response (interpolation of quench point along the core), respectively, in calculating the parameters in Eq. (2-12).

The solved sets of (a, b) shown in Fig. 2.6 scattered in a fairly wide range in (a, b) - plane, mainly due to the oscillatory behaviors of both differential pressure (and hence α)and temperature measurement (and hence h). Although the range of b varies from about 0 to 1.5, the range of a falls in a fairly narrow range between about 0.15 to 0.45. In the present work, regarding Eq. (2-12) as the heat transfer coefficient with some error, the following set of (a, b) is selected on an average as indicated in dotted lines in Fig. 2.6.

$$a = 0.25 \quad , \qquad b = 0.5 \qquad (2\text{-}13)$$

The correlation (2-9) is now written as,

$$h = (1 - \alpha)^{1/4} h_{sat} + (1 - \alpha)^{1/2} h_R \qquad (2\text{-}14)$$

It is noted that an analytical derivation of the above correlation was later accomplished by Murao using the simplified assumptions for the saturated film biling flow region[1].

2.4 Evaluation of proposed correlation

To evaluate the proposed correlation Eq.(2-14) for the transition flow region, selected data of the small scale reflood experiments[9] conducted at JAERI, PWR-FLECHT experiments and large scale reflood test conducted at JAERI were compared with the present correlation by Murao and the author[1][12][15].

(1) Data evaluation

In evaluating both experiments and the proposed correlation, the following procedures were used:

In an early stage of the reflood transient the water level stays between the measuring locations of the differential pressure, causing an erroneous void fraction. Hence, the evaluated void fraction is used for the time after the upper differential pressure transducer detected the water level.

The emissivity E is assumed to be 0.65. It is chosen as an averaged reference value (heavily oxidized: 0.9, slight oxidized: 0.4) for the Ni-Cr alloy (Inconel-600) cladding[13].

(2) Comparison of measured and predicted heat transfer coefficients

Figure 2.7 shows the calculated results by Murao[1] with Eqs.(2-2) (2-4), (2-6), (2-14), the modified Bromley correlation incorporating the distance from the quench front L_Q and the base case measurement, at T/C 4L elevation. It is shown that the present correlation and the FLECHT empirical correlation give good prediction. It is noted that the FLECHT correlation, in which the experiments were conducted with power decay, could be applicable to the JAERI's constant-power experiment. The FLECHT correlation shown in Eq.(2-4) has a relatively complex form including the parameters such as U_{in}, P and L_Q. In a steady state condition, the local flow parameters can be estimated with the inlet flow parameters. In a transient condition according to Murao[1], however, the local flow parameters would be described with the time-dependent void fraction from the inlet to the

point of interest. Therefore, the FLECHT correlation, which is expressed with inlet flow parameters, would not be preferable for the transient case.

It is noted that the present correlation give slight underestimation just before the quenching from about 120 to 160 S. This corresponds to the shift of exponent a in Eq.(2-9) from 0.5 to a smaller value as suggested by Fig. 2.6. This effect neglected in the present modeling would be considered for much better prediction in the future.

(3) Elevation effect

Figures 2.8(a) and (b) show the comparison of the calculated and measured heat transfer coefficients at the system pressures of 0.196 and 0.098 MPa, respectively. The agreement between the calculation and measurement is approximate within 15% except at 4M elevation. The measured heat transfer coefficients at the 4M elevation are lower than the calculation in an early transient when the heat transfer coefficient is relatively low. The heat transfer coefficients at 4U and 4M elevations are shown in Figs. 2.9(a) and (b). The trend of heat transfer histories at other elevations are similar to that at 4U elevation. In the case of 4M elevations, the heat transfer coefficient history has no relatively flat portion, which appeared in the case of 4U. The trend of the heat transfer history is different from those of the other locations.

This descrepancy was not explainable at the time when the present correlation was developed. It is noted that the 4M thermocouple is located only 35×10^{-3} m below the downstream grid spacer and about 565×10^{-3} m above the upstream grid spacer. The 3U thermocouple is located at the second closest to the downstream grid spacer and similar characteristics are observed as shown in Figs. 2.8(a) and (b). This condition may have influenced the heat transfer characteristics near the grid spacer location, which will be described in chapter 3.

(4) Parametric effects on heat transfer coefficient

The calculated heat transfer coefficient was compared with the measurement in order to investigate the parametric effect such as flooding rate, initial clad temperature, linear power, system pressure and inlet subcooling of the coolant. The agreement between the

calculation and the measurement are almost within ±20%, except in the case of high flooding rate (>7.5x10^{-2} m/s) as shown in Fig. 2.10.

It is noted that for the case of low flooding rate (1.4 x 10^{-2} m/s) the calculation tends to underestimate the measurement when the heat transfer coefficient is low and to overestimate it when the heat transfer coefficient is high. This trend already mentioned with Fig. 2.7. is enhanced for the low flooding case, and hence it would further be investigated to much better prediction.

Figure 2.11 shows the comparison of the calculated and measured heat transfer coefficients for all experimental conditions at 4L, 4M, 4U, 3L and 3U elevations. The hatched region includes all curves except the three highest and lowest curves. It is found that the present correlation is applicable for a practical evaluation of the heat transfer coefficient in the transition flow region within an error range of about ±30%. Generally poor predictions were observed in the cases of high flooding rates (10x10^{-2} m/s) and high system pressure (0.392 MPa).

(5) Comparison with FLECHT results

Figures 2.12(a) and (b) show the comparison of the calculated and measured heat transfer coefficients of Runs 3709 and 5342, respectively of the FLECHT low flooding series[14]. The measured data at 5G8 and 5G9 noted in the data report were used for the present comparison. The figures show that a fairly good agreement is obtained between the calculation and the measurement within an error range of 20% at most.

The above two cases were run with faily low flow housing temperature (nearly saturated temperature). It should be noted that the present correlation gives too small heat transfer coefficient for the case of high flow housing temperature. This is because that the reported void fraction is almost unity during reflood transient. This might indicate the importance of both the precise evaluation method of the void fraction and the effect of flow housing temperature.

(6) Comparison with large-scale reflood experiment

Figure 2.13 shows the comparison of the calculated and measured heat transfer coefficients of JAERI's large-scale reflood experiment[15]. The data was obtained with the Cylindrical Core Test

Facility (CCTF) with about 2,000 heated rods in the simulated core (More details of CCTF are described in 4.3 of the present paper).

As shown in the figure, the present correlation provides also a good agreement with the experiment for the large size core. Although the calculated heat transfer coefficient is slightly underestimated just before the quenching, the overall parametric effect of initial clad temperature is well predicted with the present correlation. This effect is also well simulated with REFLA code which incorporates the present correlation[16].

2.5 Summary

(1) A correlation of a heat transfer coefficient for a saturated film boilding region has been developed based on the 4x4 rod experiment conducted at JAERI. This region corresponds to the transition region between the quench front and the dispersed flow region. The correlation is formulated as Eq. (2-14). The major applicable conditions of the correlation are the flooding rate between 1.4 to 7.5 cm/s, pressure between 0.1 to 0.4 MPa and void fraction between 0.7 to 0.9.

(2) The present correlation gives good prediction for both JAERI's small scale reflood experiment and FLECHT experiment within the error range of about ±20% with a little exception. It was later found that this correlation also provides good prediction for the large scale reflood experiment conducted at JAERI.

(3) The prediction for near the grid spacer location, however, was not satisfactory with the present correlation. This suggests that the core thermo-hydraulics could be affected by the existence of the grid spacers during reflood, which will be discussed in chapter 3.

(4) The present correlation has the qualitative trends to give an overestimation when the heat transfer coefficient is low and to give an underestimation when it is high. This effect would further be investigated for much better prediction.

References

(1) Murao, Y. and Sugimoto, J.: J. Nucl. Sci. Technol., 18 [4], 275 ~284 (1981).
(2) Clement, P., et al.: 5th Annual Water Reactor Safety Research Information Meeting, Washington, Nov. 1977.
(3) Ellion, M.E.: Jet Propulsion Lab. Memo 20-80 C.I.T., (1954).
(4) Goldemund, M.H.: CREST Specialist Meeting on Emergency Core Cooling for Light Water Reactors, Munich, 18～20 Oct., 1972.
(5) Cadek, F.F, et al.: WCAP-7665, (1971).
(6) Yu, K.P., Yadigaroglu, G.: ASME paper 79-HT-48, ASME/AICHE 18th National Heat Transfer Conf., San Diego., Calif., Aug. 1979.
(7) Yeh, H.C., et al.: Nucl. Technol., 46 [MID-DEC. 1979], (1979).
(8) Sudo, Y.: J. Nucl. Sci. Technol., 17[7], 516～530 (1980).
(9) Sugimoto, J., et al.: JAERI-M 8169, (in Japanese), (1979).
(10) Sugimoto, J.: JAERI-M 6985, (in Japanese) (1977).
(11) Malang, S.: ORNL-TM-4555, (1974).
(12) Sugimoto, J., et al.: Presented at Fall Meeting of Japan Atomic Energy Society, Osaka, Oct. 1979.
(13) Touloukian, Y.S., DeWitt, D.P.: "Thermophysical Properties of Matter", Vol. 7, p.972 (1970), IFI/Plenum.
(14) Rosal, E.R., et al.: WCAP-8651, (1975).
(15) Sugimoto, J., et al.: JAERI-M 83-026, (1983).
(16) Sugimoto, J. and Murao, Y.: J. Nucl. Sci. Technol., 20[8], 656-667(1983).

Table 2.1 Main specification of small scale reflood test facility

Bundle geometry	
Arrangement	4 x 4-rod (square pitch)
Outer diameter of rod	10.5×10^{-3} m
Pitch	13.8×10^{-3} m
Heated length	3.6 m
Housing crosssection	60×10^{-3} m^2
Heater rod design	
Type	Indirect heating
Clad thickness	1.3×10^{-3} m
Clad material	Inconel-600
Outer diameter of heating element	6.4×10^{-3} m
Material of heating element	Nichrome
Axial peaking factor	1.66
Attached thermocouple	0.5×10^{-3} m O.D. ungrounded type

Table 2.2 Test conditions of referred small scale reflood experiments

System pressure (MPa)	0.098, <u>0.196</u>, 0.392
Linear peak power (kW/m)	1, <u>2.0</u>, 2.8
Flooding rate (10^{-2} m/s)	1.4, <u>4</u>, 7.5, 10
Inlet subcooling (^{o}C)	<u>20</u>, 35
Initial maximum clad temperature (^{o}C)	<u>400</u>, 550, 700

Note: Underline indicates the value of the base case.

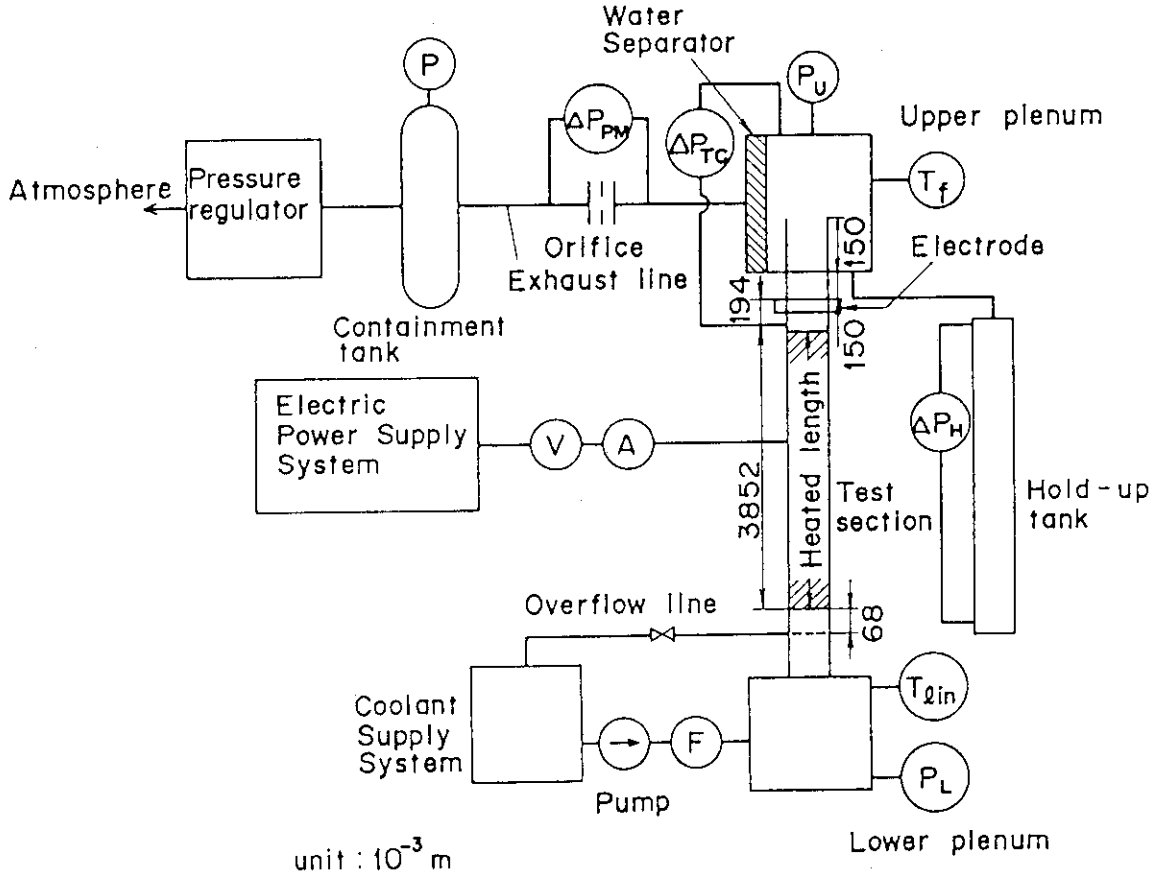

Fig. 2.1 Schematic of exprimental apparatus

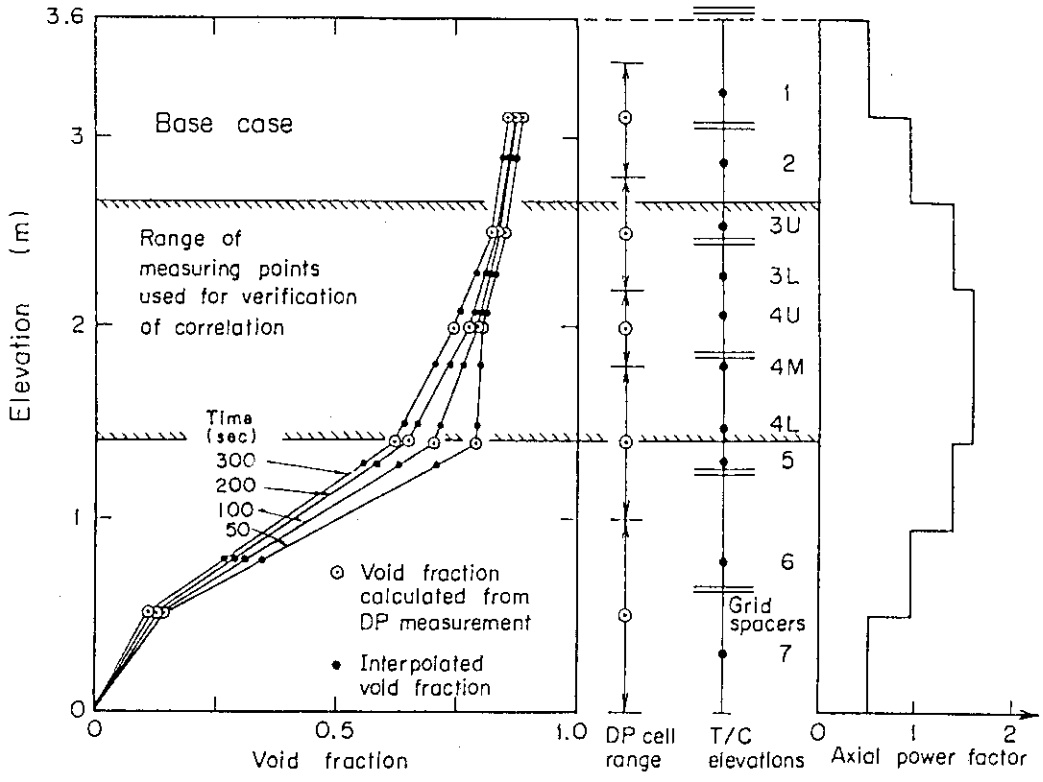

Fig. 2.2 Example of void fraction distribution and evaluation range of the present correlation

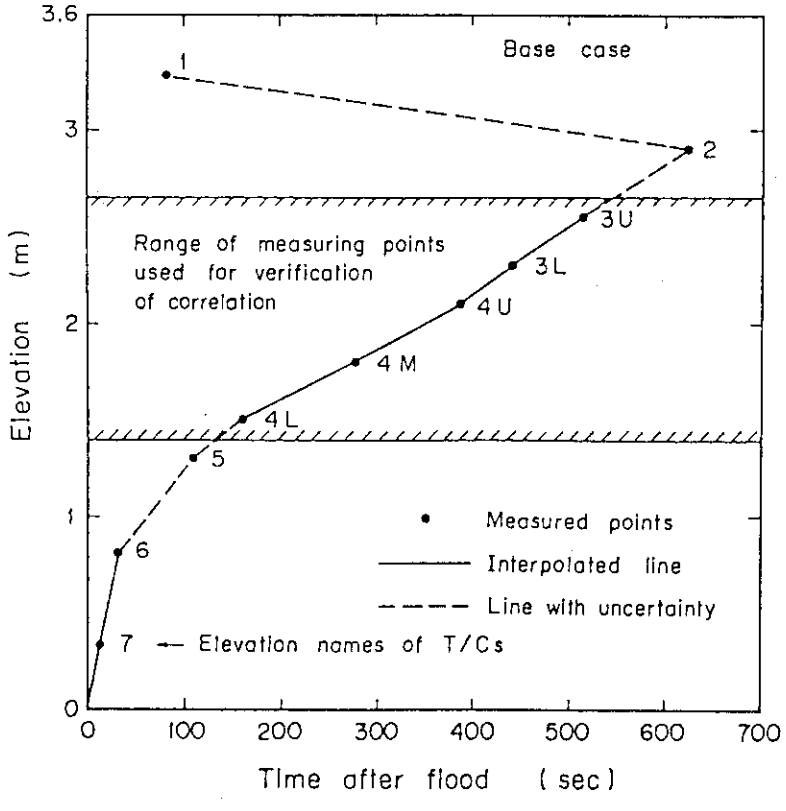

Fig. 2.3 Example of quench front propagation and evaluation range of the present correlation

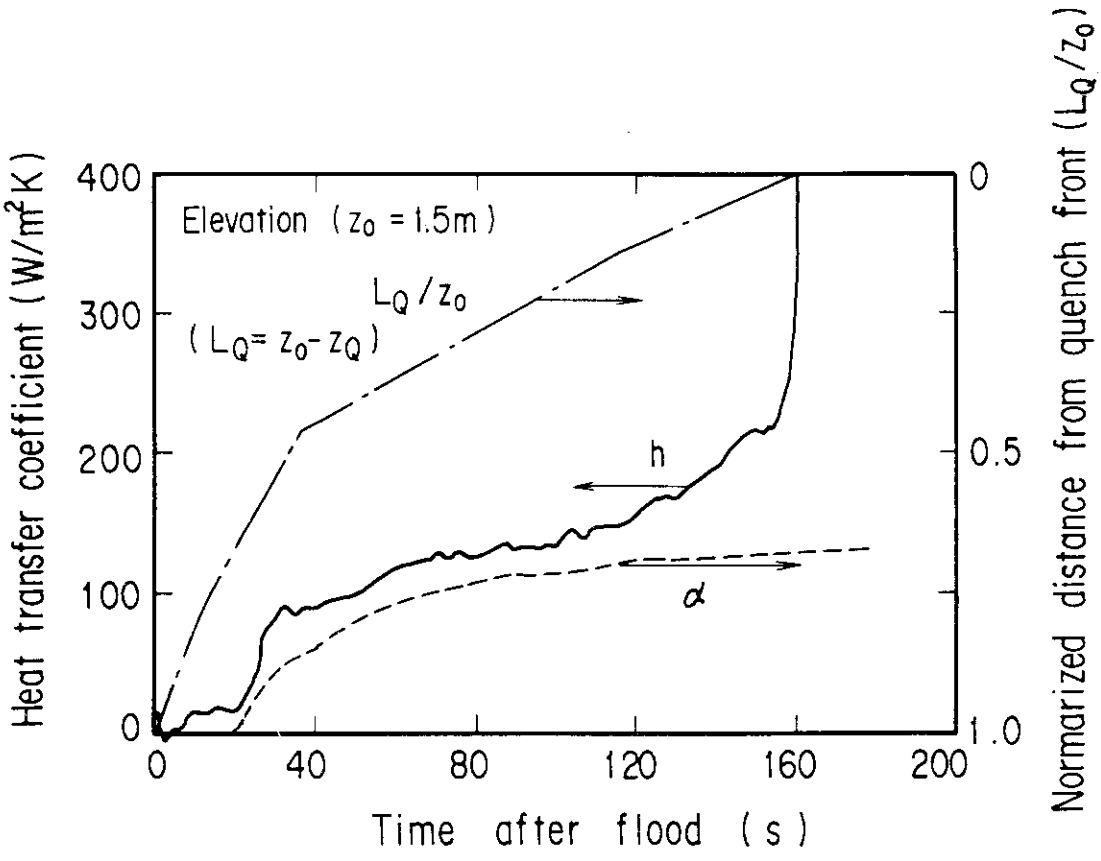

Fig 2.4 Histories of heat transfer coefficient, distance from quench front and void fraction

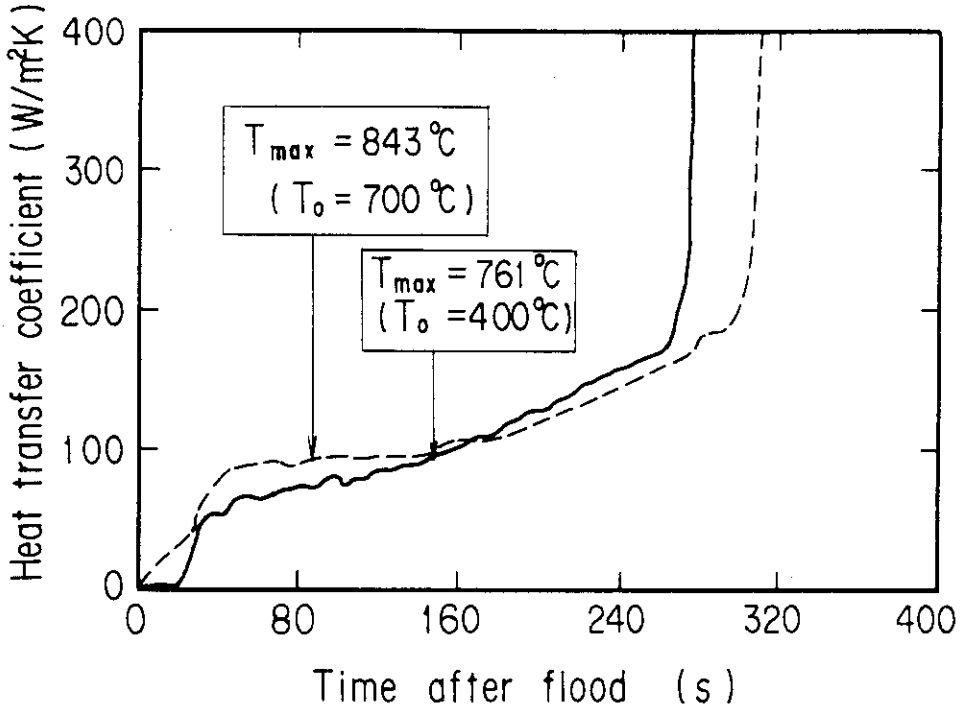

Fig. 2.5 Effect of clad temperature on heat transfer coefficient

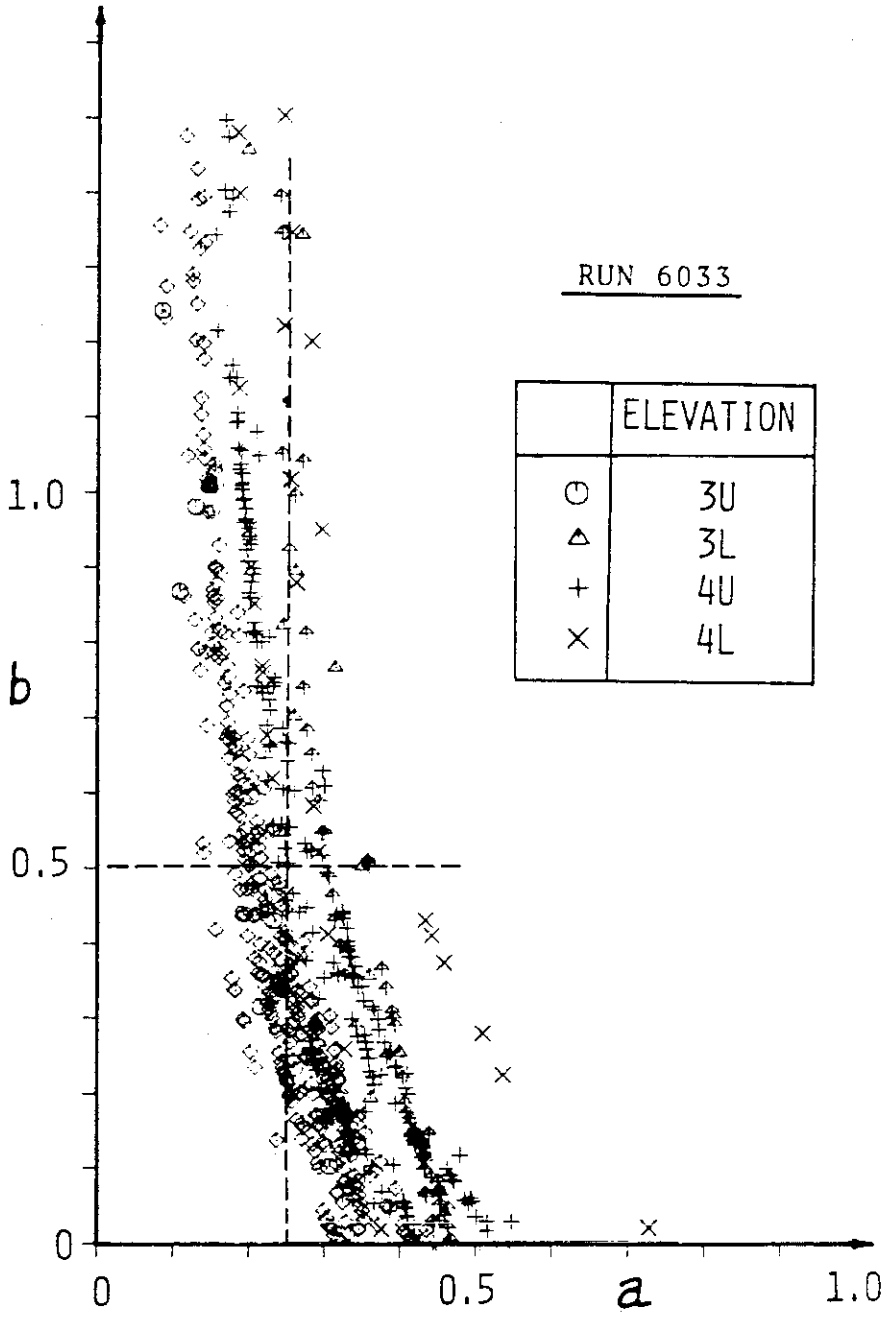

Fig. 2.6 Example of numerically solved sets of (a,b)

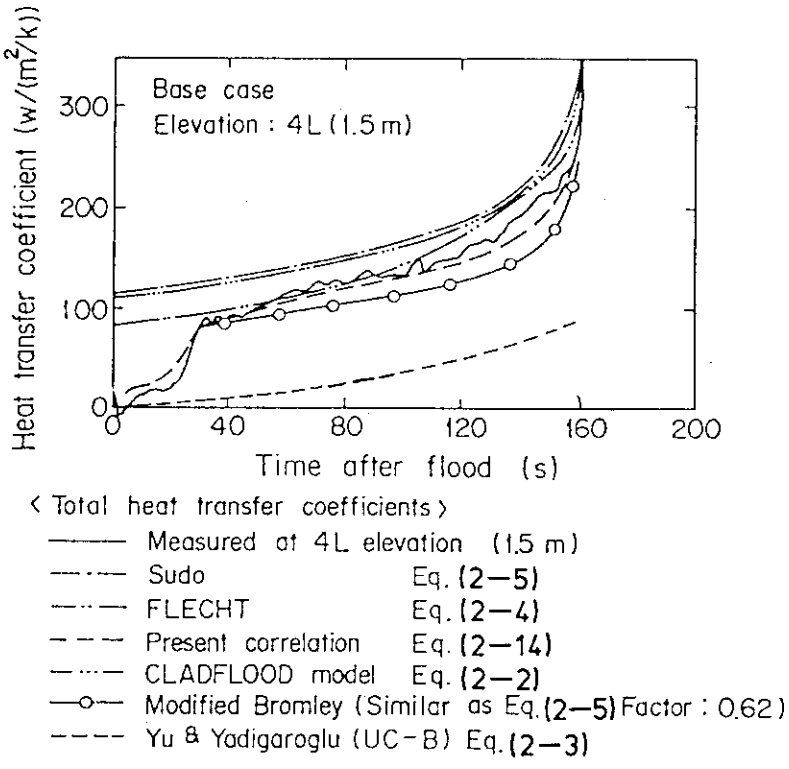

Fig. 2.7 Comparison of calculated and measured heat transfer coefficients[1]

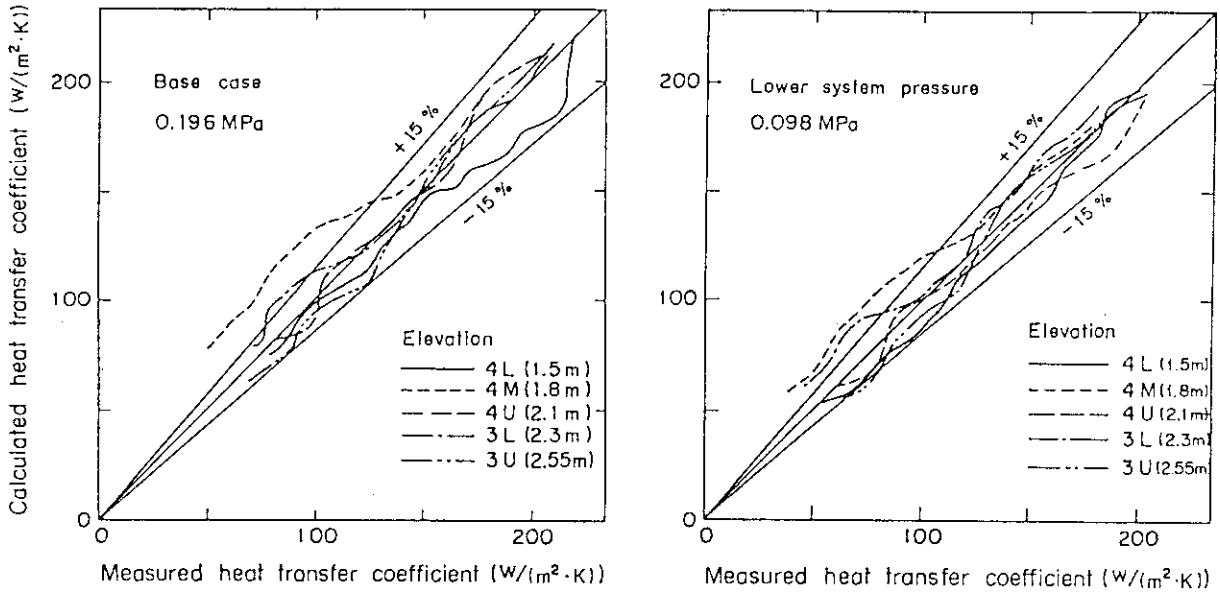

Fig. 2.8 Comparison of calculated and measured heat transfer coefficients (effect of elevation)[1]

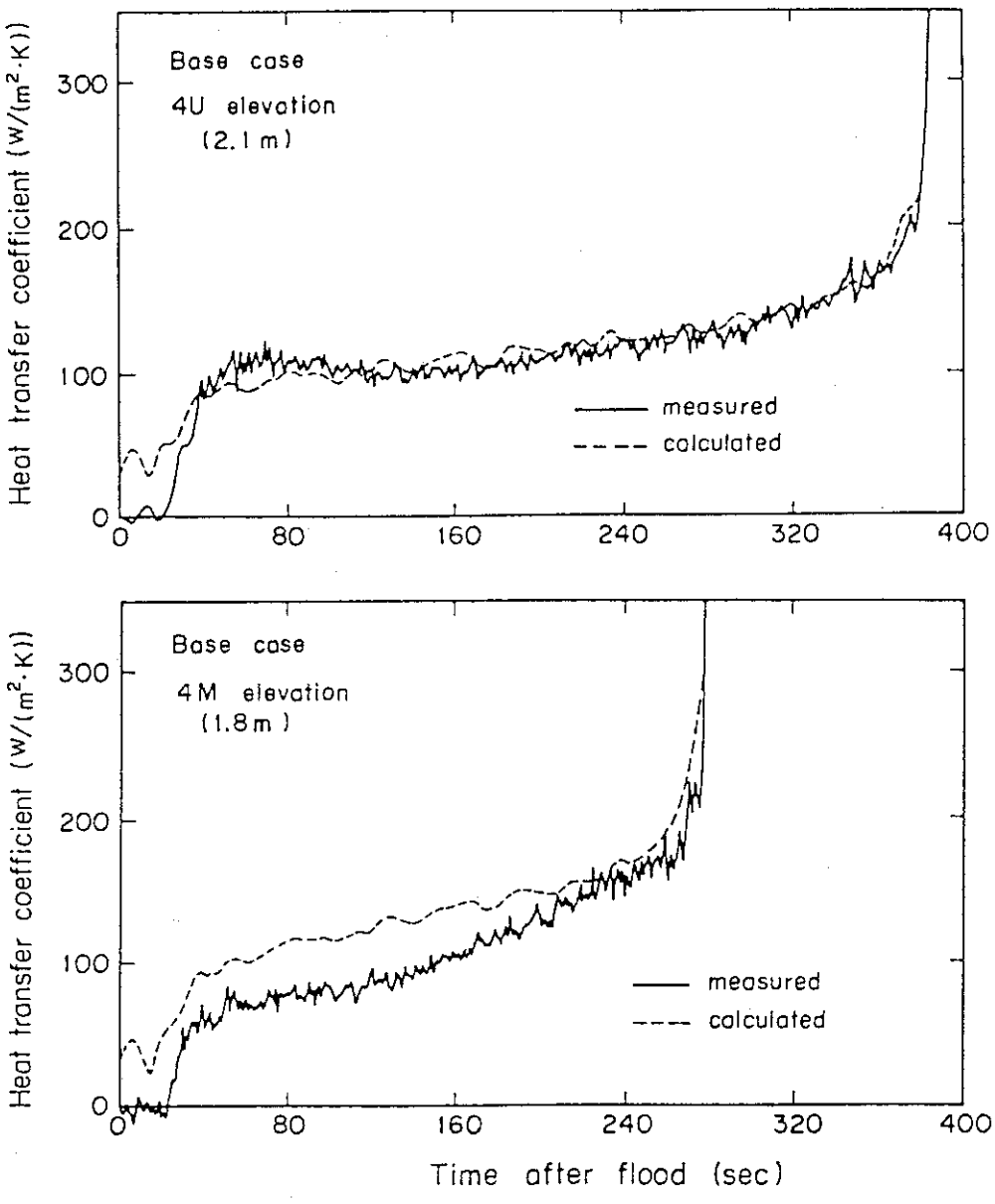

Fig. 2.9 Comparison of calculated and measured heat transfer coefficient histories[1]

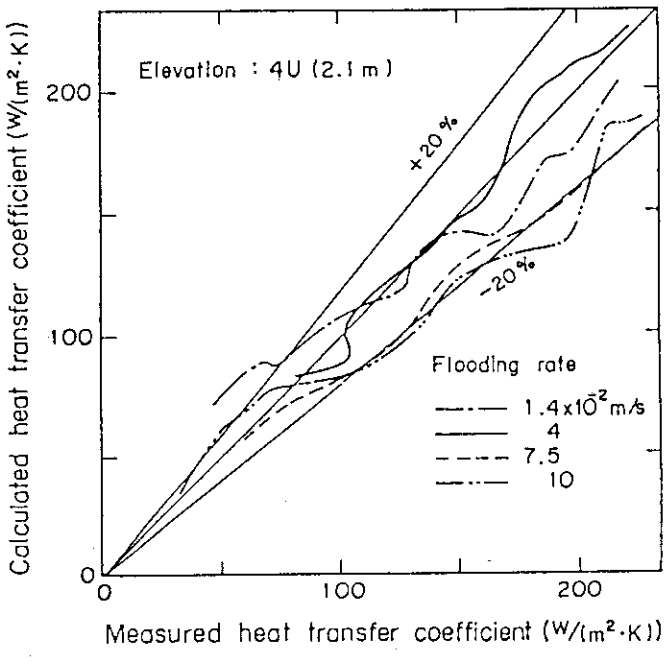

Fig. 2.10 Comparison of calculated and measured heat transfer coefficients (effect of flooding rate)[1]

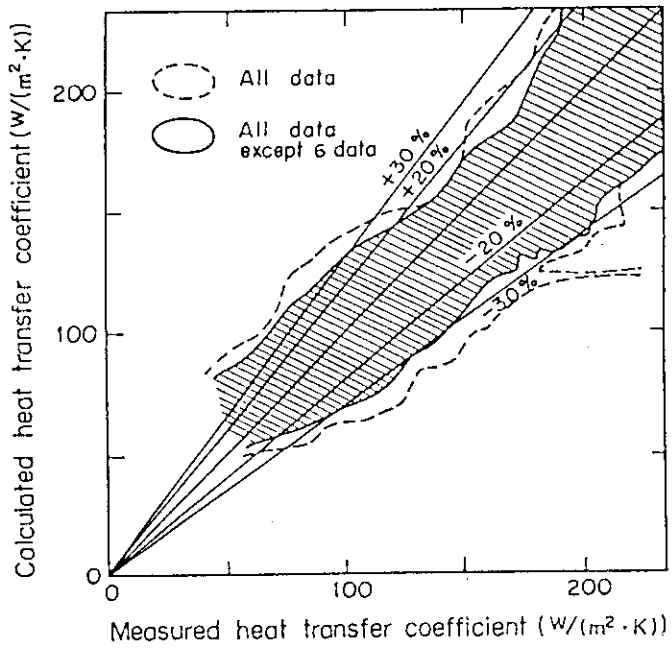

Fig. 2.11 Comparison of calculated and measured heat transfer coefficients of all data[1]

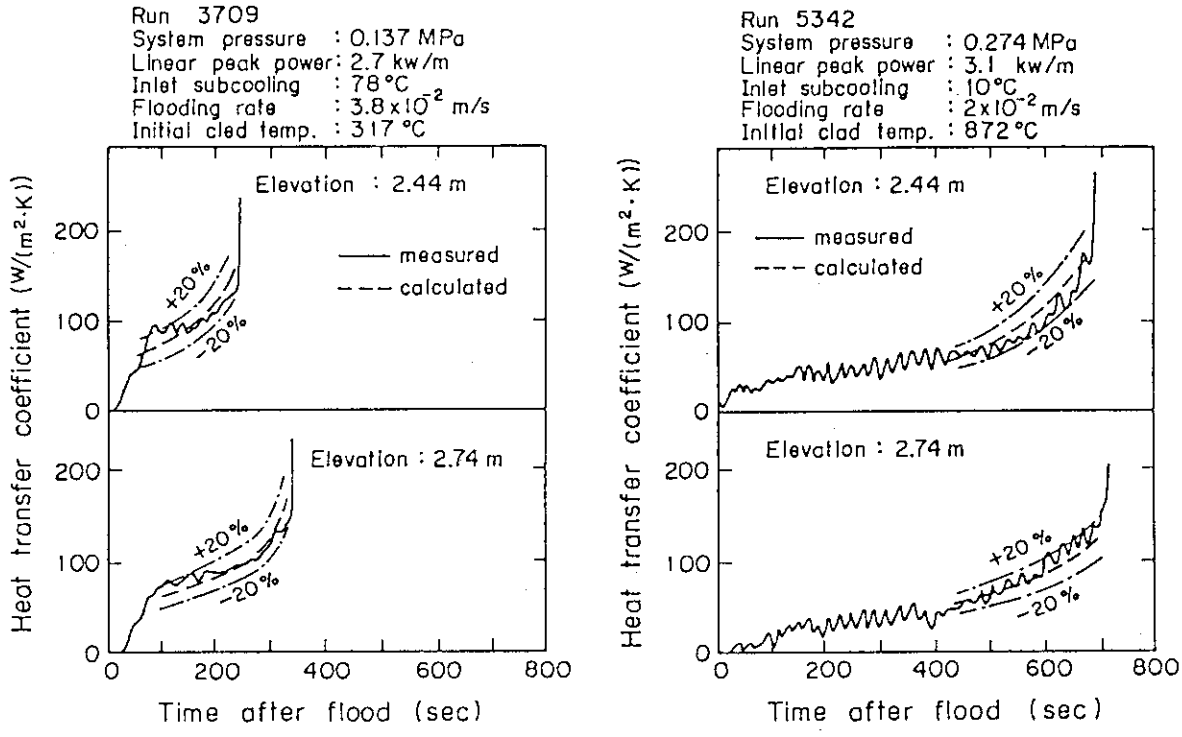

Fig. 2.12 Comparison of calculated and measured heat transfer coefficient histories (FLECHT experiment)[1]

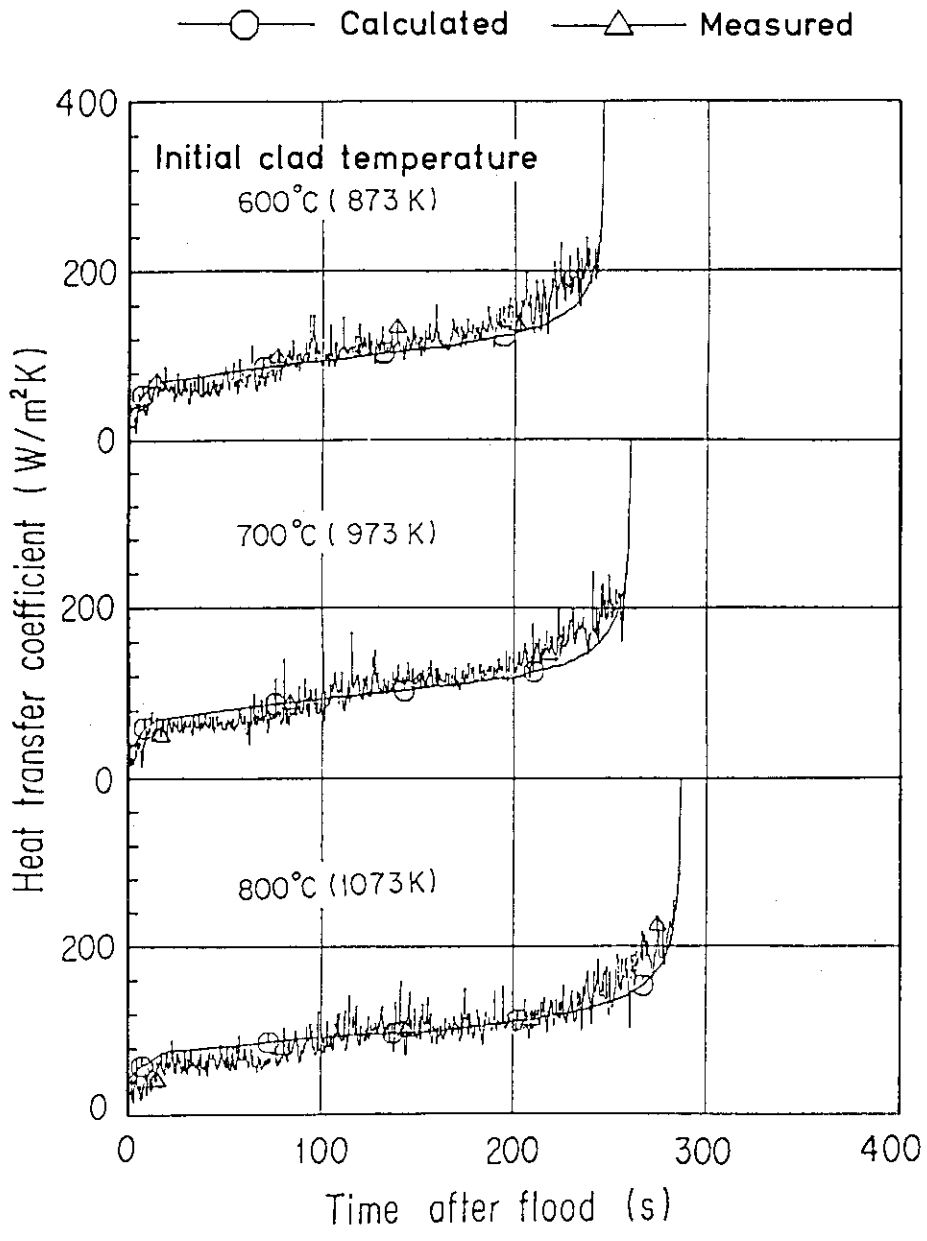

Fig. 2.13 Comparison of calculated and measured heat transfer coefficient histories at midplane (CCTF experiment)[15]

3. Effect of Grid Spacers on Core Thermo-hydraulics[1][2]

3.1 Introduction

In a light water reactor core, a relative fuel rod position is maintained by grid spacers as already shown in Fig. 1.3. In a typical reflood condition with the high-voided two-phase flow and high temperature, the grid spacers are supposed to act as flow disturbers or heat sinks. It is expected that this will cause a heat transfer enhancement downstream the grid spacer, resulting in the lowering of the peak clad temperature.

Figure 3.1 shows such an example of the axial temperature distribution obtained in FEBA experiment[3] in West Germany. It is observed that the temperature tends to be lower in the region above the grid spacer than in the same region without the grid spacer.

Figure 3.2 shows the axial heat transfer coefficient distribution obtained in FLECHT experiment[4]. Again the heat transfer is found to be enhanced downstream the grid spacer, i.e., above the grid spacer location. This heat transfer enhancement is dominant in the region where the local power is high and hence the temperature is high.

Figure 3.3 shows the detailed axial distribution of the heat transfer coefficient above the grid spacer obtained in JAERI's reflood experiment[2]. It is found that the enhancement of the heat transfer above the grid spacer is almost inversely proportional to the distance from the grid spacer at most time of the reflood transient. Especially, the heat transfer coefficient just above the grid spacer were found to be 20～50% higher than that just below the grid spacer in the inverted slug flow region.

Furthermore as already discussed in chapter 2, the developed heat transfer coefficient for the saturated film boiling (Eq. (2-14)) does not exceptionally give a good prediction near the grid spacer location. Although the breakup behaviors of water droplets have been reported in some literatures[5], the governing mechanism of the above seen effect of grid spacers has not been fully identified. It is considered that this is mainly due to the lack of detailed thermo-hydraulic information near grid spacers.

In this chapter presented is an analytical model developed for describing the effect of grid spacers on core thermo-hydraulics. The

flow observation and the model experiment have been conducted to establish the model. The experimental data in a typical reflood condition have then been compared with calculation to evaluate the present analytical model.

3.2 Flow observation and model experiment

(1) Flow observation

In order to provide a physically reasonable model for the effect of grid spacers on core thermo-hydraulics, a flow observation in a typical reflood condition has been made using a full length 6x6 rod bundle test section described in section 3.4. The 16mm movie camera with about 3 μs strobe light was utilized for the recording of the observed flow through the central viewing window attatched on the flow housing.

Photo 3.1 shows an example of the observed flow at the core midplane through the 50 mm window obtained in a 15x15 type rod bundle experiment[1] described in section 3.4. Case A and B correspond to the runs with the grid spacer locations A and B shown in Fig. 3.4, respectively. The Case A is the location below the grid spacer, whereas Case B is the location just above the grid spacer by shifting the grid spacer downwards.

Before about 10 s of the reflood transient, the flow is identified as a single phase vapor. The water droplets begin to appear in the vapor flow at about 10 s of the transient as shown in Photo 3.1. This droplet dispersed flow continues up to about 30 s. The water droplets become larger, and the united droplets can semetimes be observed in the later part of the dispersed flow region. The flow then becomes an inverted slug flow with large oscillating water slugs as shown in ④ in Photo 3.1 through the end of the transient.

Figure 3.5 shows the distribution of the water droplet diameter in the dispersed flow region. The droplet diameter was calibrated with the rod diameter of 10.7 mm. The distribution just below the grid spacer is shown by a solid line, while the distribution just above the grid spacer is shown by a broken line. The droplet diameter tends to be smaller just above the grid spacer (Case B) than below the

grid spacer (Case A). It is considered that this decrease of the droplet diameter is primarily due to the breakup of the impinging droplets by the edge of the grid spacer.

The distribution of the droplet diameter can well be described with a Γ-distribution function shown in a smoothed line in Fig. 3.5. The Γ-distribution is written as

$$\frac{\Delta N}{N} = \frac{\tau^{\tau}}{\Gamma(\tau)} \left(\frac{d}{\bar{d}} \right)^{\tau-1} \exp\left(-\tau \frac{d}{\bar{d}} \right) \frac{\Delta d}{\bar{d}} \quad , \tag{3-1}$$

where

ΔN : Number of droplets with diameter from $d-\Delta d/2$ to $\bar{d}+\Delta d/2$

N : Total number of droplets, $\Gamma(\tau)$: Gamma function

d : Average droplet diameter, σ_n : Standard deviation.

Photo 3.2 shows another example of the observed flow at the core midplane near the central grid spacer obtained in a 17x17 type rod bundle experiment[2]. In this experiment, described also in section 3.4, the flow near the grid spacer could be observed through the long viewing window (200 mm long).

At a first stage of transient, the flow was identified as a single-phase vapor as in Photo 3.1. The flow then became a water-droplet dispersed flow. It is noted that in this region, the onset of the water accumulation was observed after the complete rewetting of the grid spacer wall, which was indicated by a thermo-couple attached to the grid spacer wall.

The water accumulation above the grid spacer advanced upward to form nearly inverted slug flow above the grid spacer. The flow below the grid spacer eventually became a similar inverted slug flow. This inverted slug flow which contains large oscillating water slugs lasted to the end of the transient.

Figure 3.6 shows a typical void fraction distribution near the grid spacer, derived from a differential pressure measurement by neglecting frictional and accelerational pressure losses. The void fraction in the inverted slug flow region above the grid spacer increases almost exponentially with the distance from the grid spacer, as shown in Fig. 3.6. Hence, the heat transfer enhancement just above the grid spacer in inverted slug flow is primarily due to this increased water accumulation above the grid spacer, causing better film boiling heat transfer.

Figure 3.7 compares the distribution of water droplet diameter between just below and above grid spacer in the dispersed flow region. The droplet diameter, which was measured from the 16 mm film taken at the viewing window, again tends to be smaller just above the grid spacer than below the grid spacer. It is considered that this decrease of the droplet diameter is primarily due to the breakup of the impinging droplets by the edge of grid spacers.

(2) Model experiment

The decrease of the average diameter of water droplets above the grid spacer shown in Figs. 3.5 and 3.7 could be attributed to the breakup phenomena of water droplets. In order to confirm this phenomena and to further construct a mechanstic model, a simple water breakup experiment was conducted.

Figure 3.8 shows the experimental rig arrangement. A water droplet which is upflow in a reflood situation is simulated by a falling water droplet in an atmospheric pressure and temperature conditions. Since the droplet diameter thus determined by the surface tension is relatively large (~4 mm), a rather thick plate (1.5 mm) simulating the grid spacer wall was used. The breakup process of the falling water droplets was recorded either by a streak camera or a 16 mm movie camera with about 3 s strobe light.

Photo 3.3 shows some examples of the trace of the water droplet obtained with the streak camera. The picture was taken with an opened shutter, the motor-drive film winding mechanism and a strobe light.

It has been shown that the water droplet tends to be split into two major portions. The velocity of the droplet after the break is only slightly retarded by the impingment.

Photo 3.4 shows some examples of the picture taken by the 16 mm movie camera with the strobe light just after the breakup occurred. The water droplets are sometimes split into several droplets with similar size. A fairly many fine droplets could also be observed besides the larger size of droplets. Some fraction of the initial droplet was found to be left on the plate wall, but it is considered that this would be strongly restricted by the hot wall in a reflood condition.

As a summary from the present model experiment, it is considered that the water droplet in the dispersed flow, if it hits the edge of

the grid spacer wall, tends to be split into several smaller size of droplets.

3.3 Analytical model

(1) General flow model

Based on the findings from the flow observation and model experiment discussed in the previous section, a thermo-hydraulic model for predicting the behavior near the grid spacer was developed. Figure 3.9 shows the schematic diagram of the present flow model near grid spacers.

The flow is assumed to be a single-phase vapor at first until the vapor velocity exceeds a critical value to generate water droplets. The flow then becomes a droplet dispersed flow along the core when the vapor velocity and hence the vapor-to-water relative velocity is higher than the critical value. The average diameter of water droplets above the grid spacer is smaller than that below the grid spacer due to the breakup by the spacer wall. At the same time it is also assumed that the quenching of the spacer wall advances in this dispersed flow region due to the impinging water droplets.

It is considered that once the spacer wall is quenched completely, a water film on the wall is easily re-entrained in the flow. This will then cause a relatively water-enriched flow above the grid spacer, forming a larger size of water droplets suspending in the region above the grid spacer. This situation is enhanced by the counter-current flow limitation (CCFL) since the reduced flow area at the grid spacer location accelerates the vapor flow. It is therefore assumed that just after the complete quenching of the spacer wall, a water accumulation initiates to form an inverted slug flow above the grid spacer.

The flow in the region near above the quench front is also inverted slug flow. The heat transfer coefficient in this inverted slug flow is generally larger than that in the dispersed flow. The transition from the dispersed to inverted slug flow is determined by the Weber number criteria as described below. This inverted slug flow condition lasts at the end of the transient with increasing water fraction in the core subchannel.

(2) Single-phase vapor region

In a single-phase vapor region, the flow downstream the grid spacer is disturbed and accelerated by the grid spacers, resulting in the enhanced heat transfer. The pressure drop and the heat transfer enhancement of the grid spacers in a single-phase liquid have been studied for the design requirement[6]. This heat transfer enhancement is described by the correlation developed by Yao et al.[7],

$$h_2 = h_1(1 + 5.55\ a^2\ e^{-z/7.7De}) \ , \tag{3-2}$$

where h_2 and h_1 are the heat transfer coefficient with and without grid spacers, respectively, a the blocking ratio of the grid spacer, Z the distance from upper edge of the grid spacer and De the hydraulic diameter.

(3) Dispersed flow region

In a dispersed flow, the rewetting of the grid spacer wall initiates. The rewetting velocity, v_Q, of the grid spacer is described with Yamanouchi's correlation[8]:

$$v_Q = \frac{1}{\rho\ Cp}\sqrt{\frac{\lambda\ h_0}{\delta}} \cdot \frac{To - Tsat}{Tw - To} \ . \tag{3-3}$$

where the spacer wall temperature, T_w, is assumed to be equal to the clad temperature. Since the heat capacity of the grid spacer is much smaller than that of the heated rod, the heat storage process of the grid spacer is neglected in the present model.

The average droplet diameter above the grid spacer was found to be smaller than that below the grid spacer as already shown in the previous section. In the present modeling, this is assumed to be caused by the brekup of the water droplet when it collides with the blocking surface of the grid spacer.

The effective atomization factor η due to the grid spacer is defined as,

$$\eta = d_{SM2}/d_{SM1} \ , \tag{3-4}$$

using Sauter mean diameter d_{SM}, which is the thermo-hydraulic mean diameter conserving the void fraction and the surface area, given by

$$d_{SM} = \overline{d^3}/\overline{d^2} \quad . \tag{3-5}$$

In Eq. (3-4), suffixes 1 and 2 denote the droplet just below and above the grid spacer, respectively. The mathematical mean diameter $\overline{d}$ is expressed as,

$$\overline{d} = \frac{1}{N} \sum_{i=1}^{N} d_i = \frac{1}{N} \sum_{j=1}^{M} \nu_j d_j \quad , \tag{3-6}$$

where N is the total number of the droplet in the concerning volume, d_i the i-th droplet diameter and ν_j the number of droplet of the j-th diameter class in totally M diameter classes.

In order to estimate the effective atomization factor η, it is assumed that the probability of the droplet breakup is equal to the blocking ratio a of the flow channel and the water droplet is split into n smaller droplets with same diameters. First, the mass conservation across the grid spacer requires the following for the collided droplet:

$$d_{2_j} = n^{-1/3} d_{1_j} \quad . \tag{3-7}$$

Since the total number of droples after breakup is (1-a)N+anN,

$$\overline{d_2^2} = \frac{1}{(1-a)N + anN} \sum_{j=1}^{N} \{(1-a)\nu_j d_{1_j}^2 + an\nu_j d_{2_j}^2\} \quad . \tag{3-8}$$

where a is the blocking ratio of the grid spacer.
Using Eq. (3-7),

$$\overline{d_2^2} = \frac{1 + (n^{1/3}-1)a}{1 + (n-1)a} \overline{d_1^2} \quad . \tag{3-9}$$

Similarly,

$$\overline{d_2^3} = \frac{1}{1 + (n-1)a} \overline{d_1^3} \quad . \tag{3-10}$$

Therefore, η in Eq. (3-4), is written as

$$\eta = \frac{1}{1 + (n^{1/3}-1)a} \quad . \tag{3-11}$$

The wall-to-vapor heat transfer enhancement due to the disturbance of the vapor flow by the grid spacer is again described by

the correlation (3-2).

(4) Inverted slug flow

In the inverted slug flow region, the void fraction increases exponentially to the saturated value $\bar{\alpha}$ with the distance from the grid spacer, z, using the effective length of heat enhancement z_{GS} as,

$$\alpha = \bar{\alpha} \left(1 - e^{-z/z_{GS}} \right) \tag{3-12}$$

where $\bar{\alpha}$ is calculated with the method proposed by Murao et al.[9] using the modified Cunnigham-Yeh and Lockhart-Martinelli correlations:

$$\bar{\alpha}=[1+(U_{go}+U_{\ell o})/\Delta U-\{1+2(U_{\ell o}-U_{go})/\Delta U+(U_{go}+U_{\ell o})^2/\Delta U^2\}^{\frac{1}{2}}]/2 \ , \tag{3-13}$$

where $\Delta U = U_{go}/\min(\alpha_{CY},\alpha_{LM})$

$$\alpha_{CY} = 0.925(\rho_g/\rho_\ell)^{0.239}(U_{go}/U_{bcr})^{a}$$

$$U_{bcr} = 1.53(\sigma \cdot g/\rho_\ell)^{0.25}$$

$$a = \begin{cases} 0.67 & (U_{go}/U_{bcr} < 1) \\ 0.47 & (U_{go}/U_{bcr} \geq 1) \end{cases}$$

$$\alpha_{LM} = 1 + 0.84(U_{\ell o}/U_{go})^{0.64}(\rho_\ell/\rho_g)^{0.28}(\mu_\ell/\mu_g)^{0.07}$$

The heat transfer enhancement in the inverted slug flow is expressed with the correlation by Murao and Sugimoto[10] for the saturated film boiling described in chapter 2 using α in Eq. (3-12) as,

$$h = 0.94(1-\alpha)^{\frac{1}{4}}[\lambda_g{}^3 \rho_g \rho_\ell H_{fg}\, g/L_Q \mu_g (T_w - T_{sat})]^{\frac{1}{4}} \tag{3-14}$$

$$+ \varepsilon E(1-\alpha)^{\frac{1}{2}} (T_w^4 - T_{sat}^4)/(T_w - T_{sat}) \tag{(2-14)}$$

The water accumulation above the grid spacer can initiate after the complete rewetting of the spacer wall. The transition boundary from inverted slug flow to dispersed flow in the unquenched region between grid spacers is described with the critical Weber number criteria[11] as;

$$We = \rho_g \Delta U^2 d \ / \ \sigma > We \ crit \ . \tag{3-15}$$

3.4 Test description

1) Experimental apparatus

The experimental apparatus, shown in Fig. 3.10, consists of a test section, an exhaust line with an orifice and a pressure regulating system, a carry-over tank to measure separated water, and an ECC water supply system. The test section consists of a 6x6 heater rod bundle, lower and upper plena, and a flow channel housing.

The schematic of the test section and the heater rod are shown in Fig. 3.11. Two types of rod bundle geometry are tested in the present study; One is a 15x15 type geometry with 10.7 mm rod outer diameter, 14.3 mm pitch, and 3.60 m heated length. The other is a 17x17 type geometry with 9.5 mm rod outer diameter, 12.6 mm pitch, and 3.66 m heated length. Specific items are compared in Table 3.1 between 15x15 and 17x17 type rod geometries. It is noted that main design features of 17x17 rod geometry are the same as those of heated rods used in the Cylindrical Core Test Facility (CCTF) at JAERI[12], except for the reduced rod diameter.

The rod bundle is supported with seven grid spacers connected to four non-heated rods at the corners. The wall thickness and height of the grid spacers are 0.8 mm and 40 mm, respectively. The sectional differential pressures and the rod surface temperatures are measured along the test section. The flow housing is equipped with several viewing windows to observe the flow inside the rod bundle.

2) Experimental procedure

The experimental procedure is as follows:

(1) The coolant circulates through the lower plenum to the overflow line before the test; the flow rate, the coolant temperature, and housing wall temperature are adjusted to the specified values during this period.

(2) The electric power is supplied to the heated rods and the data recording is initiated. The recording of the visual flow data with a 16 mm movie camera with strobe light is also initiated.

(3) The coolant injection into the test section is initiated by closing the overflow valve when a clad temperature at the midplane reaches a pre-set value at reflood initiation.

(4) The supplied power is kept constant and the pressure in the

containment tank is maintained constant by exhausting the generated vapor during the test.

(5) When all the clad temperatures indicate quenching of the rods, the power supply and the data recording are stopped, terminating the test.

3) Experimental conditions

The experimental conditions of the present tests which are considered to cover the typical reflood conditions of a PWR-LOCA are shown in Table 3.2

3.5 Evaluation of proposed model

The grid spacer model described above was implemented in the REFLA code[11] to evaluate the model by comparing the calculation with experiments.

(1) 15x15 rod geometry

Reflood experiments for 15x15 rod geometry were first conducted to investigate the overall characteristics of the effect of grid spacers on core thermo-hydraulics.

In the calculation, the main features of the grid spacer effect were modeled such as vapor flow acceleration, water breakups in the dispersed flow and increased water accumulation above the grid spacers in the inverted slug flow.

In the present calculation, the effective atomization factor η in Eq.(3-4) was set to 0.8 and the characteristic length Z_{GS} in Eq.(3-12) was set to 0.15 (m) based on the experimental result[1].

Figure 3.12 shows the measured and the calculated temperature histories at the midplane just above the grid spacer. Also shown in the figure is the calculation without the present grid spacer model. Although the peak clad temperature is slightly underestimated, the overall temperature transient is much better predicted with the present grid spacer model than the calculation without the model. It is noticed that the sooner quench time and the lower quench temperature are also well predicted with the model.

The axial temperature distribution at 100 s along the test

section is shown in Fig. 3.13. The calculation without the grid spacer model tends to overestimate the temperature in the region of the high power level. The early quenching observed above 3.3 m elevation is not predicted by the codes due to the lack of the top-down quenching model. The calculation with the grid spacer model, however, gives better agreement with the experiment, especially in the region just above the grid spacer.

(2) 17x17 rod geometry

Reflood experiments for 17x17 rod geometry were then conducted with more detailed instrumentation[2]; The axial temperature and pressure distributions were measured up to every 2 cm near the grid spacer locations. The wall temperature of the grid spacer was measured in a more reliable manner than the method used for 15x15 rod geometry. In the calculation, therefore, the grid spacer effect described in 3.2 were fully modeled for 17x17 rod geometry. In the present calculation, the effective atomization factor, η, in Eq. (3-4) was set to 0.8, the effective length of the grid spacer Z_{GS} in Eq. (3-12) was selected to 0.10 (m) based on the experimental results shown in Figs. 3.3 and 3.7. The critical Weber number in Eq. (3-15) of 0.1 was used based on the study by Murao[12].

Figure 3.14 shows the measured and calculated temperature histories at 1.015 m elevation. It is shown that the overall temperature transient, including turnaround and quench temperatures, is well predicted with the present model for a relatively low elevation.

Figure 3.15 shows the measured and calculated temperature histories at 1.83 m (midplane) elevation. This location is about 7 cm below the lower edge of the central grid spacer. The temperatue before about 80 s of the transient is well predicted with the code, but the temperature after about 80 s is somewhat underestimated. This suggests that the heat transfer is slightly less in 17x17 rod geometry than 15x15 rod geometry, mainly due to a thinner rod-to-rod pitch. It is noted that the calculated quench temperature agrees well with the experiment.

Figure 3.16 shows the measured and calculated temperature histories at 1.96 m elevation, i.e., about 2 cm above the upper edge of the central grid spacer. The calculation gives good agreement with

the experiment before about 120 s of the transient. Especially the temperature transient near the turnaround, which is strongly affected by the grid spacer at this elevation, is well predicted with the present model. The temperature after about 120 s of the transient is again a little underestimated.

Figure 3.17 shows the calculated and measured axial temperature distribution along the core at 100 and 200 s of the transient. The comparison between the calculation and the experiment in the later transient is not so good as in the early transient. This is probably due to the overestimated heat transfer coefficient in the inverted slug flow region. However, the overall tendency, especially the local heat transfer enhancement downstream the grid spacer, is predicted well by the code. This indicates that the present model concerning the effect of grid spacers is quite reasonable.

(3) Discussion

The present model for the droplet breakup in the dispersed flow is rather simple and the model for the water accumulation above the grid spacer in the inverted slug flow is semi-empirical.

The calculated radiative heat transfer estimated with the second term in Eq. (3-14) is comparably small, but it can be enhanced by the rewetted or cooled grid spacer when the rod surface temperature is extremely high. The observed decrease of the droplet diameter above the grid spacer could be related to the de-entrainment or the re-entrainment of the droplets by the grid spacer surface, which is not considered in the present modeling. The further investigation, therefore, would be required for the more mechanistic modeling.

In both 15x15 and 17x17 rod bundle geometries, it was found that the effect of grid spacers on the core thermo-hydraulics has been comparatively well predicted with the present model. For 17x17 rod bundle geometry, however, the heat transfer coefficient just below the grid spacer tended to be somewhat slightly overestimated compared with 15x15 rod bundle geometry. It is considered that the experimental differences between 15x15 and 17x17 rod bundle geometries such as axial power profile shown in Fig. 3.11 or the structure of the flow housing might have caused this thermo-hydraulic difference.

3.6 Summary

(1) From the flow observation in a typical reflood condition, the flow regions were identified as a single-phase vapor, a droplet dispersed flow, and a transition inverted slug flow above the quench front. In the dispersed flow, the diameter of the water droplets was smaller above the grid spacer than below the grid spacer. The water accumulation above the grid spacer initiates after the rewetting of the grid spacer wall. In the inverted slug flow, the water accumulation above the grid spacer was larger than below the grid spacer.

(2) A model experiment has been conducted to observe the water droplet breakups expected in the dispersed flow. It was found that the water droplet, if it hits the edge of the grid spacer wall, tends to be split into several smaller size of droplets.

(3) A thermo-hydraulic model for flow and heat trnasfer near the grid spacers was developed based on the findings from the flow observation and the model experiment: Water droplets are broken up due to the impingment on the spacer wall, resulting in the increased heat transfer from the vapor to the droplets. The rewetting of the spacer advances in the disperesed flow. Water accumulation above the grid spacer initiates after the complete rewetting of the spacer wall to form the inverted slug flow. Finally, the water accumulation above the grid spacer decreases exponentially with the distance from the grid spacer.

(4) The present analytical model has been assessed with the existing experiments. The thermo-hydraulic behavior near the grid spacer was well predicted with the present model for both 15x15 and 17x17 rod bundle geometries. Especially the calculated temperature behavior near the turnaround just above the grid spacer, which was not predicted with the previous model, gave good agreement with the experiment.

(5) A further work would be required for more mechanistic modeling of the flow concerning the effect of grid spacers, and for a trend giving somewhat overestimated heat transfer coefficient for 17x17 rod bundle geometry than 15x15 rod bundle geometry.

References

(1) Sugimoto, J. and Murao, Y.: J. Nucl. Sci. Technol., 21[2], 103~114 (1984).
(2) Sugimoto, J., et al.: Presented at 3rd Int. Conference on Reactor Thermal Hydraulics, New Port, (1985).
(3) Ihle, P., et al.: Presented at Int. Mtg. on Thermal Nuclear Reactor Safety, Chicago, (1982).
(4) Conway, C.E., et al.: NRC/EPRI Rep., Nol. 1, (1977).
(5) Lee, S.L., et al.: Presented at 10th Water Reactor Safety Information Mtg., Gaithersburg, (1982).
(6) Rehme, K.: Nucl. Technol., 17[15], 15~ 23 (1973).
(7) Yao, Y., et al.: ASME paper 80-WA/HI-62, (1980).
(8) Yamanouchi, A.: J. Nucl. Sci. Technol., 5[11], 547~ 558 (1968).
(9) Murao, Y. and Iguchi, T.: J. Nucl. Sci. Technol., 18[8], 613 627 (1982).
(10) Murao, Y. and Sugimoto, J.: J. Nucl. Sci. Technol., 18[4], 275 284 (1981).
(11) Murao, Y.: J. Nucl. Sci. Technol., 16[11], 803~817 (1979).
(12) Murao, Y., et al.: J. Nucl. Sci. Technol., 17[9], 705~719 (1982).

Table 3.1 Comparison of main specifications between 15x15 and 17x17 rod bundle geometries

Bundle geometry	PWR bundle 15x15	Experiment (6x6)	PWR bundle 17x17	Experiment (6x6)
Pitch (mm)	14.3	14.3	12.6	12.6
Heated length (mm)	3.66	3.60	3.66	3.66
Number of heated rod	204	32	264	32
Number of non-heated rod	21	4	25	4
Outer diameter of heated rod (mm)	10.7	10.7	9.5	9.5
Clad material of heated rod	Zircaloy-4	Inconel 600	Zircaloy-4	Inconel 600
Insulating material in heated rod	(UO_2)	MgO	(UO_2)	MgO(or BN)
Outer diameter of non-heated rod (mm)	13.8	13.8	12.2	12.2

Table 3.2 Experimental conditions

(a) Tests with 15x15 rod bundle geometry

System pressure	P_{sys}	(MPa)	0.1, 0.2
Linear peak power	P_p	(kW/m)	1.6, 1.8, 2.0
Flooding rate	U_{in}	(m/s)	0.04, 0.06
Initial peak clad temperature	T_{win}	(^{o}C)	400, 550
Inlet subcooling	ΔT_{sub}	(K)	20

(b) Tests with 17x17 rod bundle geometry

System pressure	P_{sys}	(MPa)	0.1, 0.2
Linear peak power	P_p	(kW/m)	1.3, 1.6
Flooding rate	U_{in}	(m/s)	0.015 0.072
Initial peak clad temperature	T_{win}	(^{o}C)	550 750
Inlet subcooling	ΔT_{sub}	(^{o}C)	20
Flow housing temperature	T_H	(^{o}C)	120, 440
Tie plate blocking ratio	a_{TP}	(-)	0, 0.35, 0.68

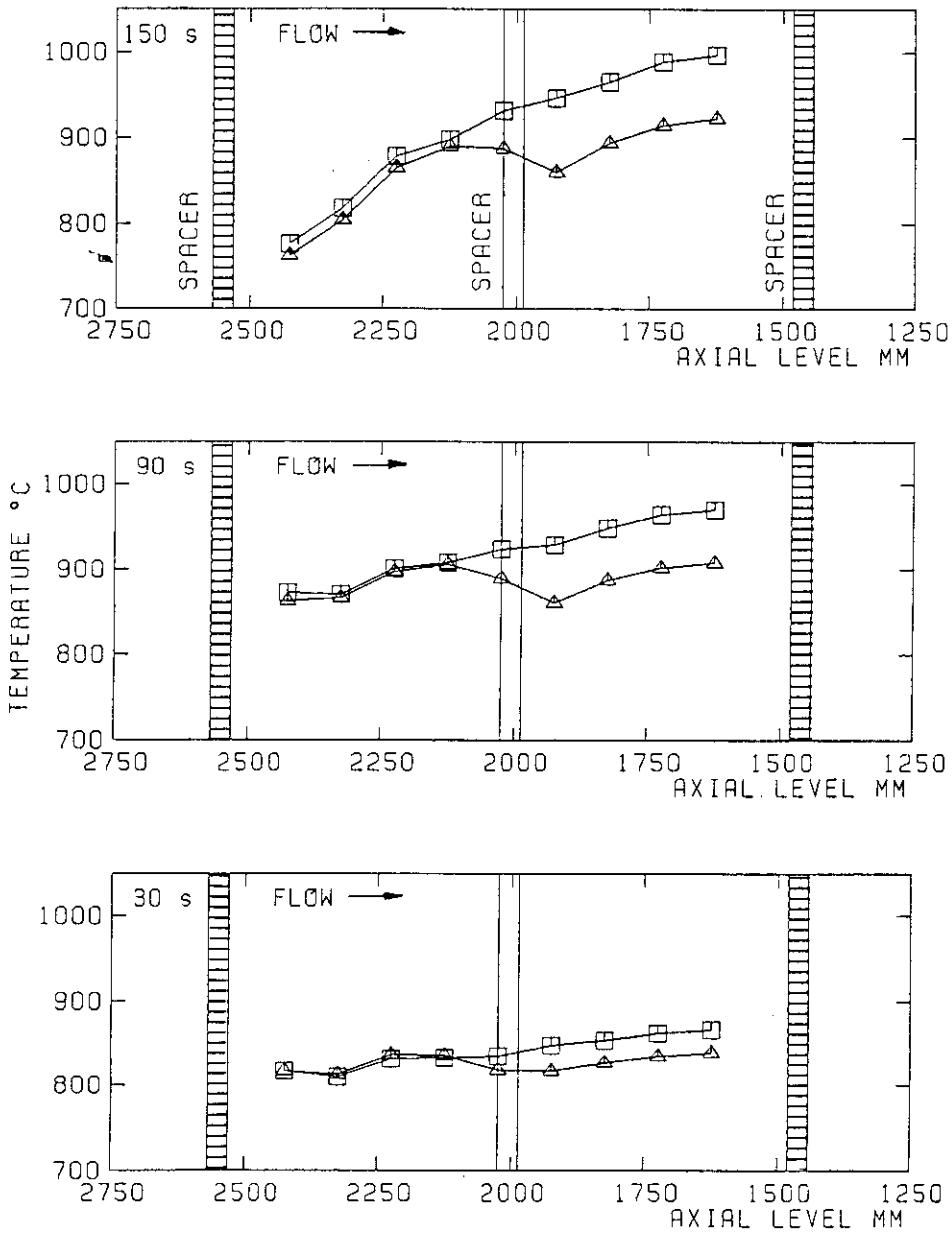

Flooding Rate　3.8 cm/s
System Pressure　2.1 bar

△ Test Series I
Test No. 223
(7 Grid Spacers)

□ Test Series II
Test No. 234
(6 Grid Spacers, without Spacer at Bundle Midplane)

Fig. 3.1　Effect of grid spacer on axial temperature distribution (FEBA experiments[3])

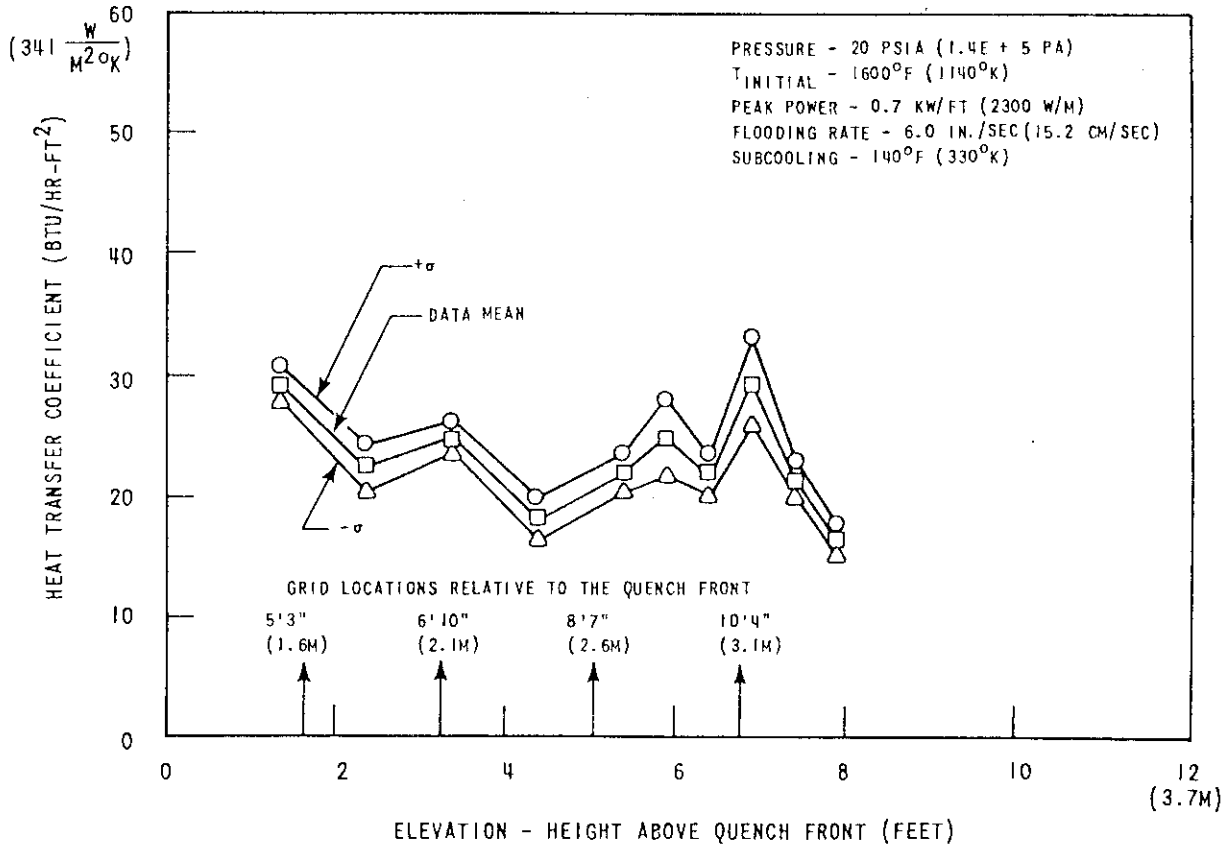

Fig. 3.2 Effect of grid spacer on axial heat transfer coefficient distribution (FLECHT experiments[4])

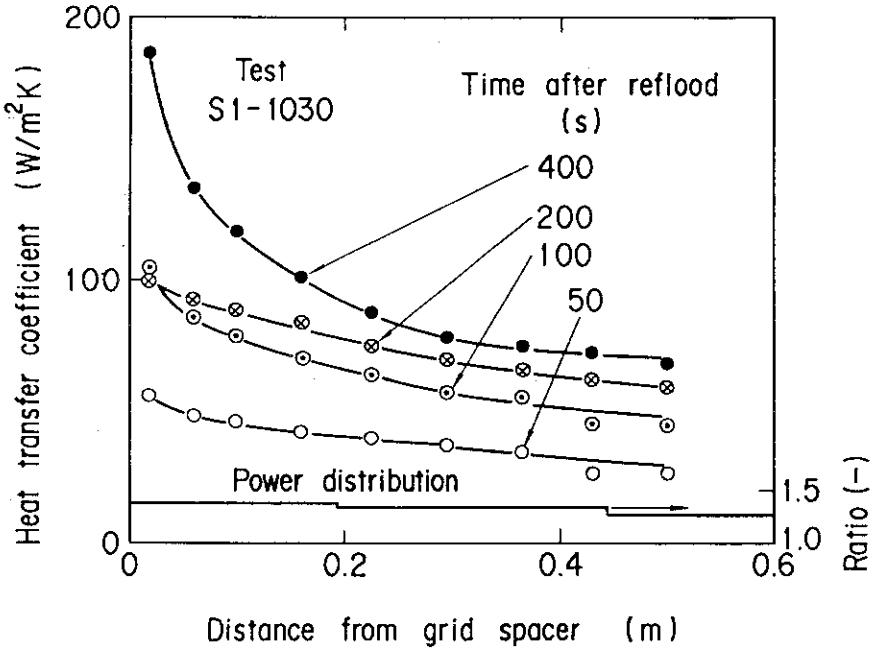

Fig. 3.3 Effect of grid spacer on axial heat transfer coefficient distribution (JAERI's experiments[2]).

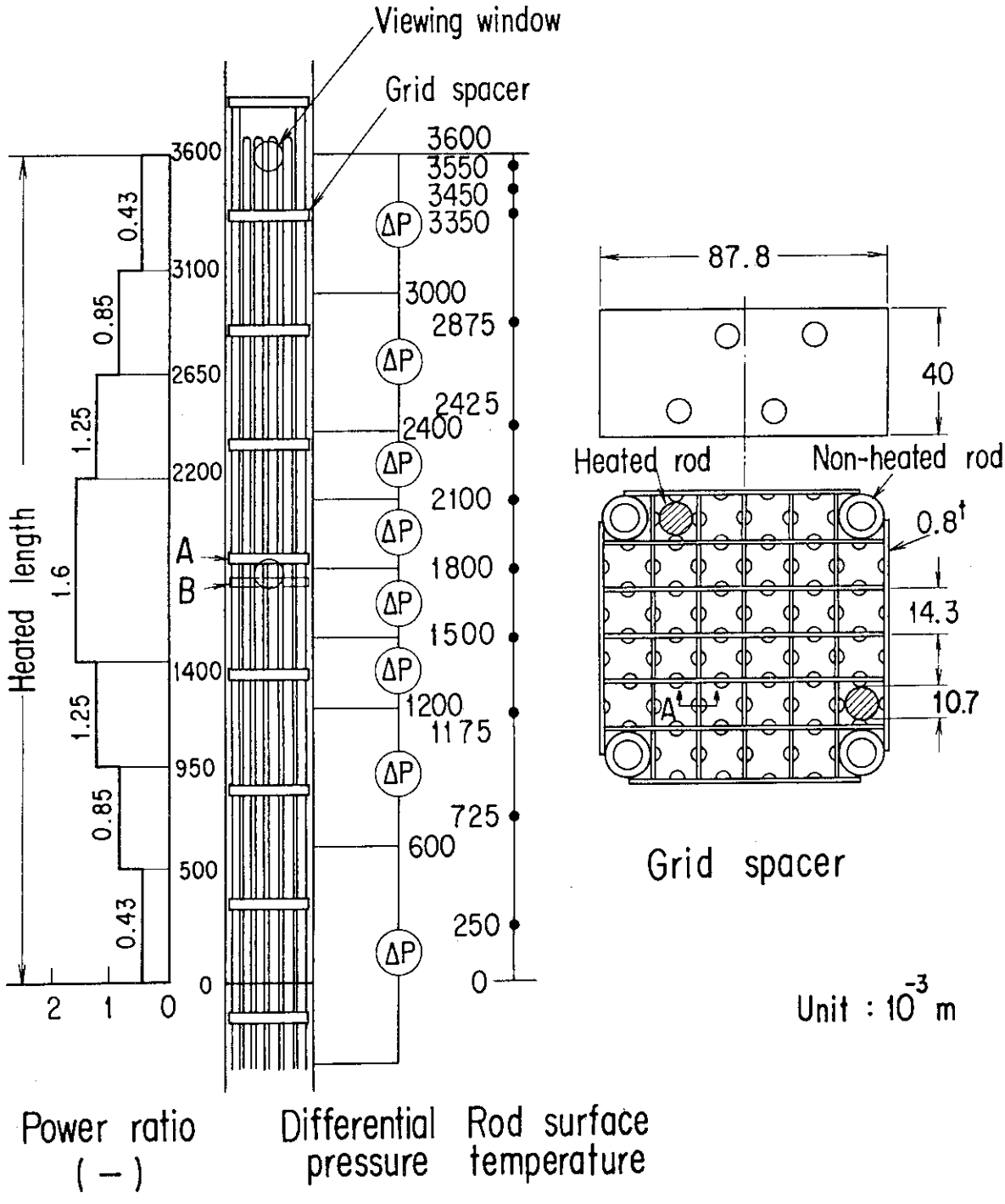

Fig. 3.4 Location of central grid spacer in Cases A and B, and details of grid spacer (15x15 rod bundle geometry)

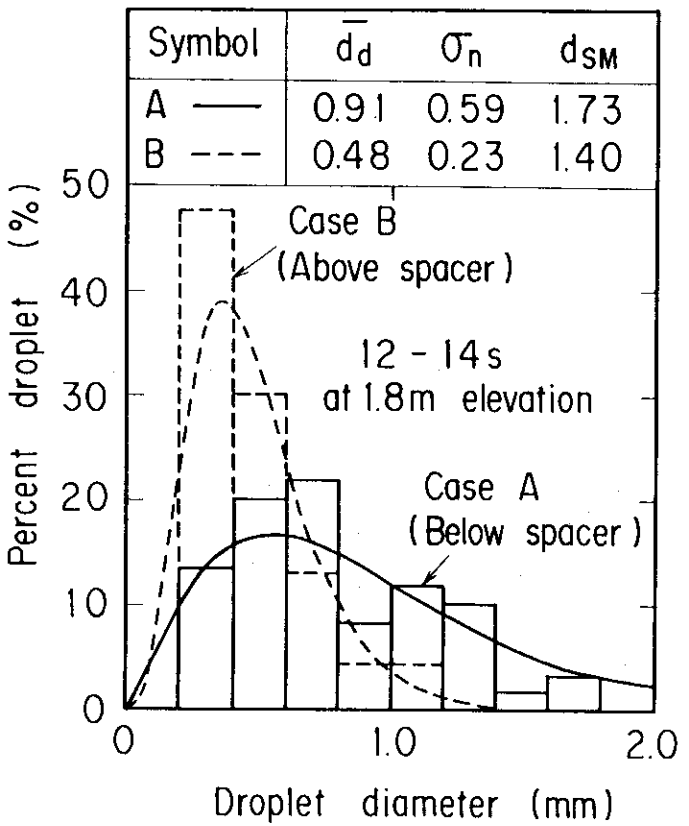

Fig. 3.5 Comparison of droplet diameter distributions between Case A and B (15x15 rod bundle geometry)

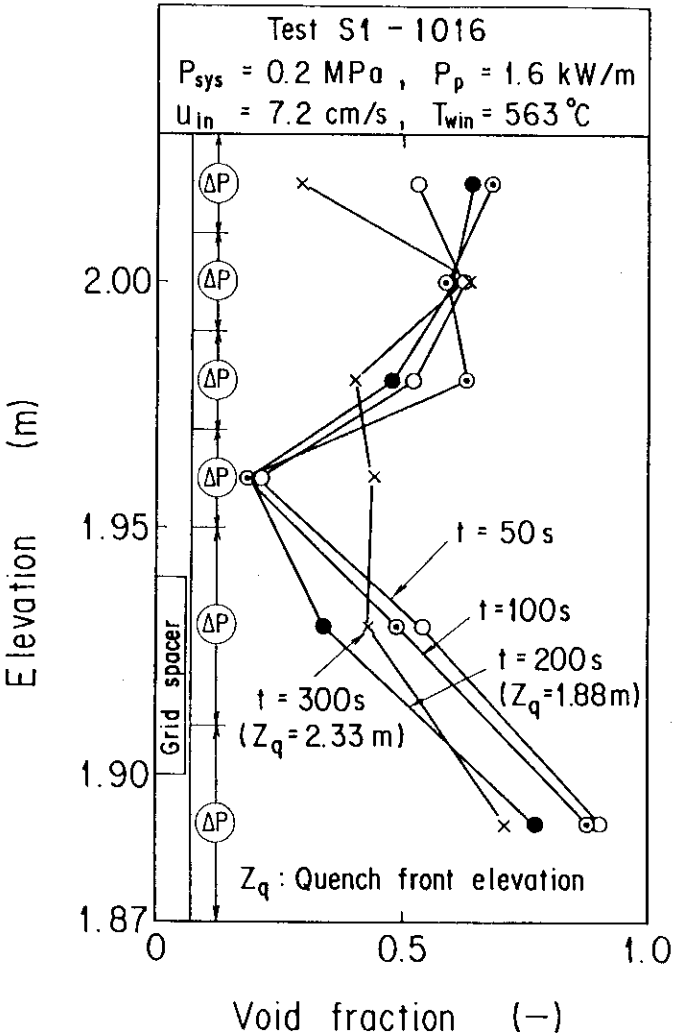

Fig. 3.6 Axial void fraction distribution near the central grid spacer (17x17 rod bundle geometry)

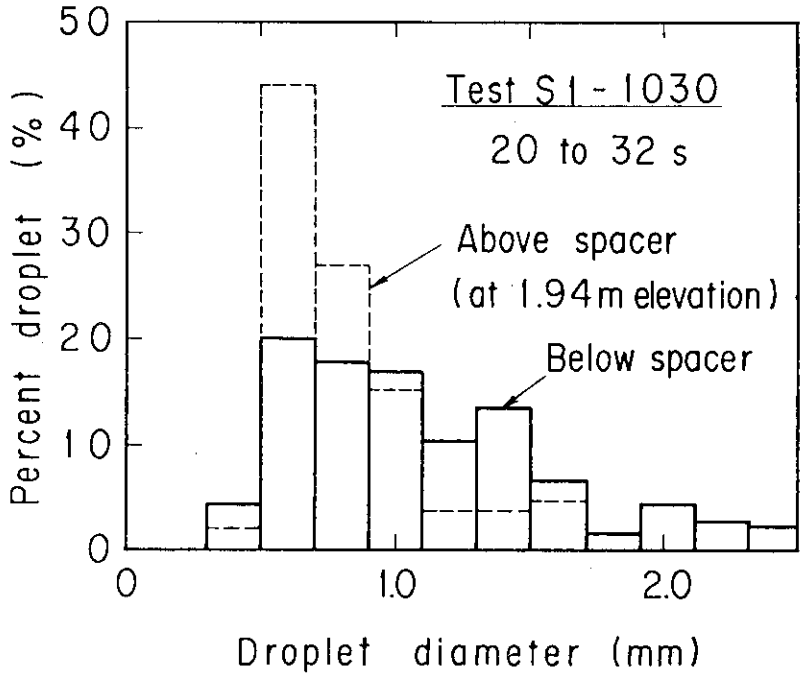

Fig. 3.7 Comparison of droplet diameter distributions between below and above the central grid spacer (17x17 rod bundle geometry)

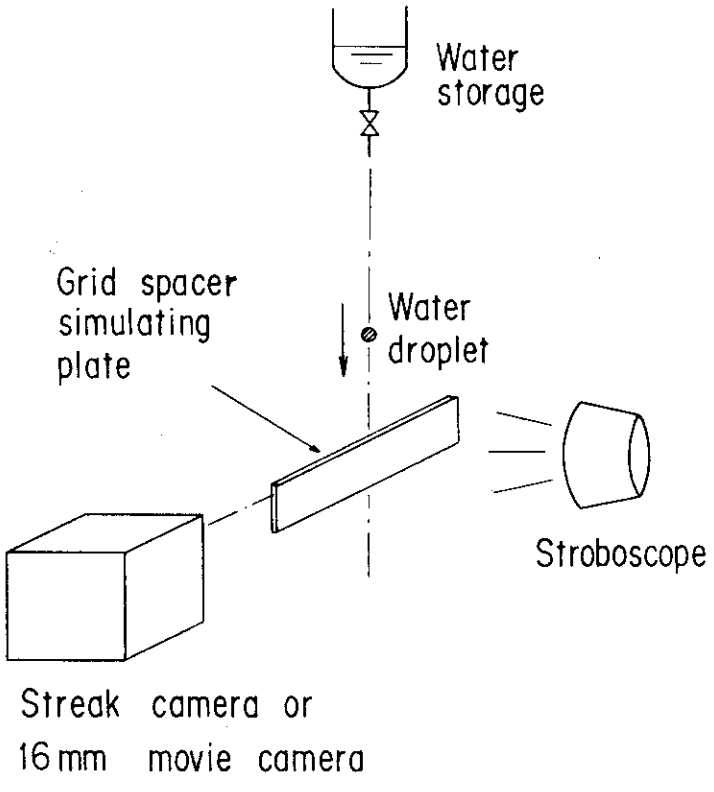

Fig. 3.8 Schematic of test rig arrangement of model experiment

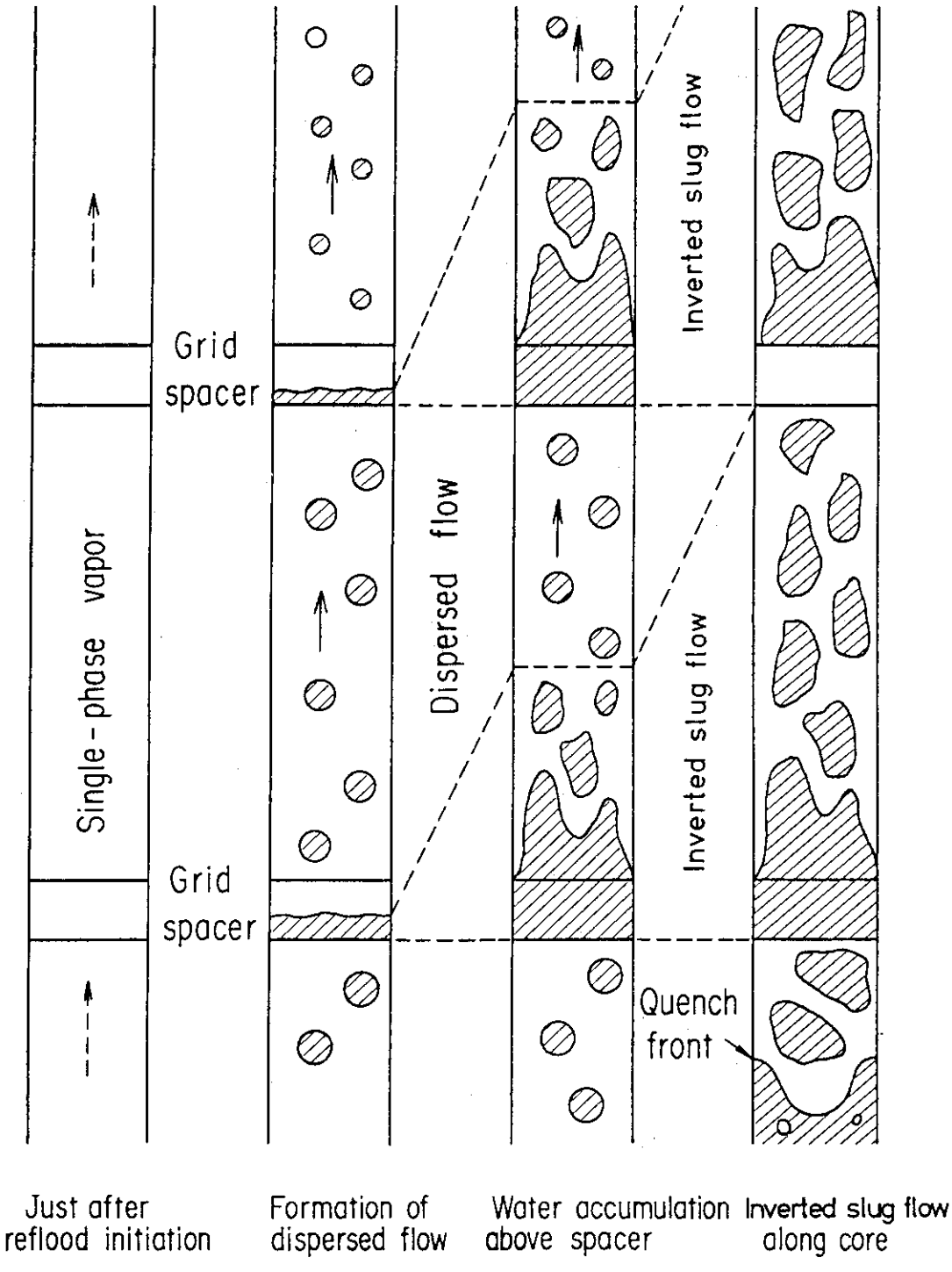

Fig. 3.9 Flow model near grid spacers in dispersed and inverted slug flows

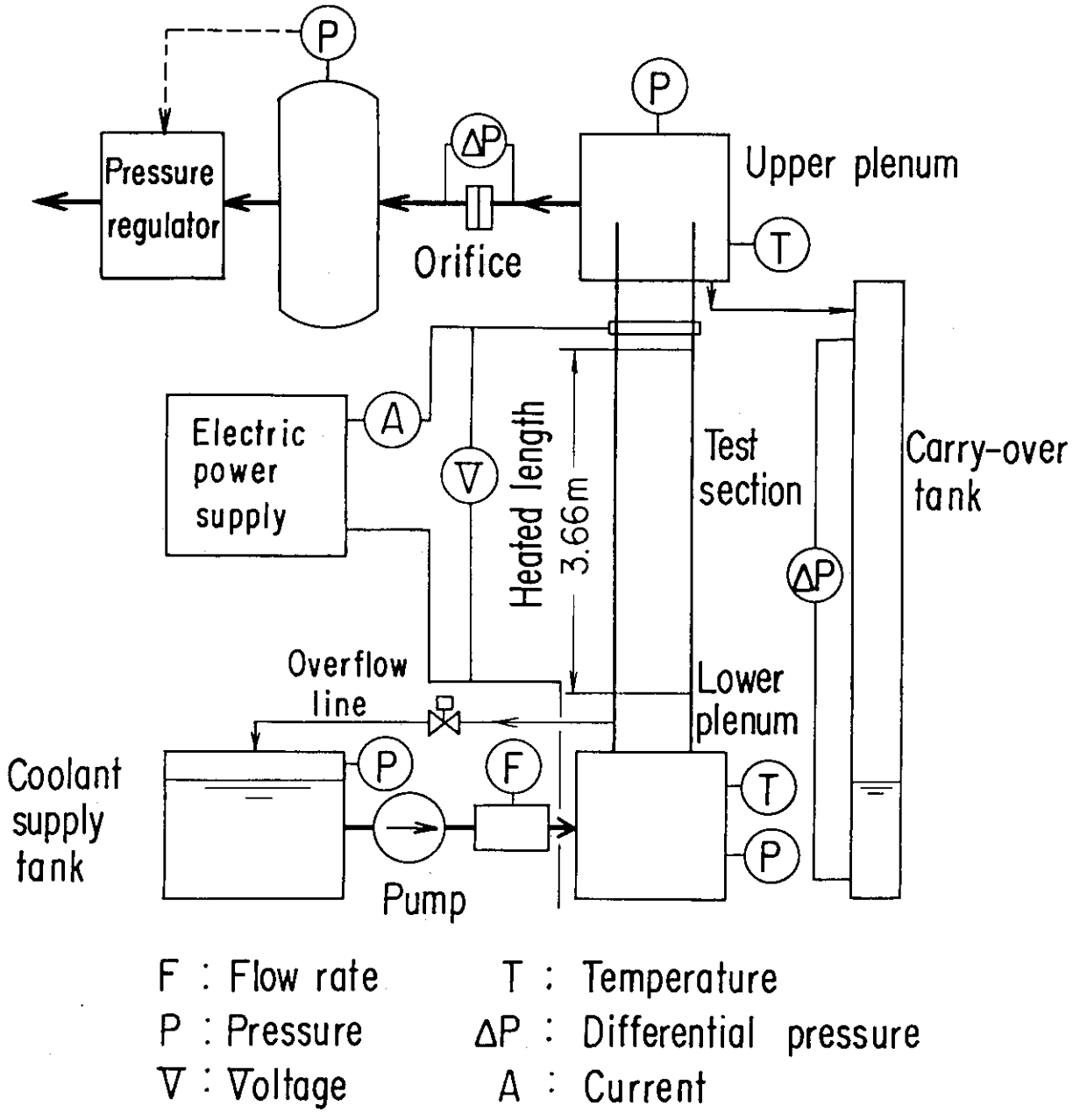

Fig. 3.10 Schematic of experimental apparatus

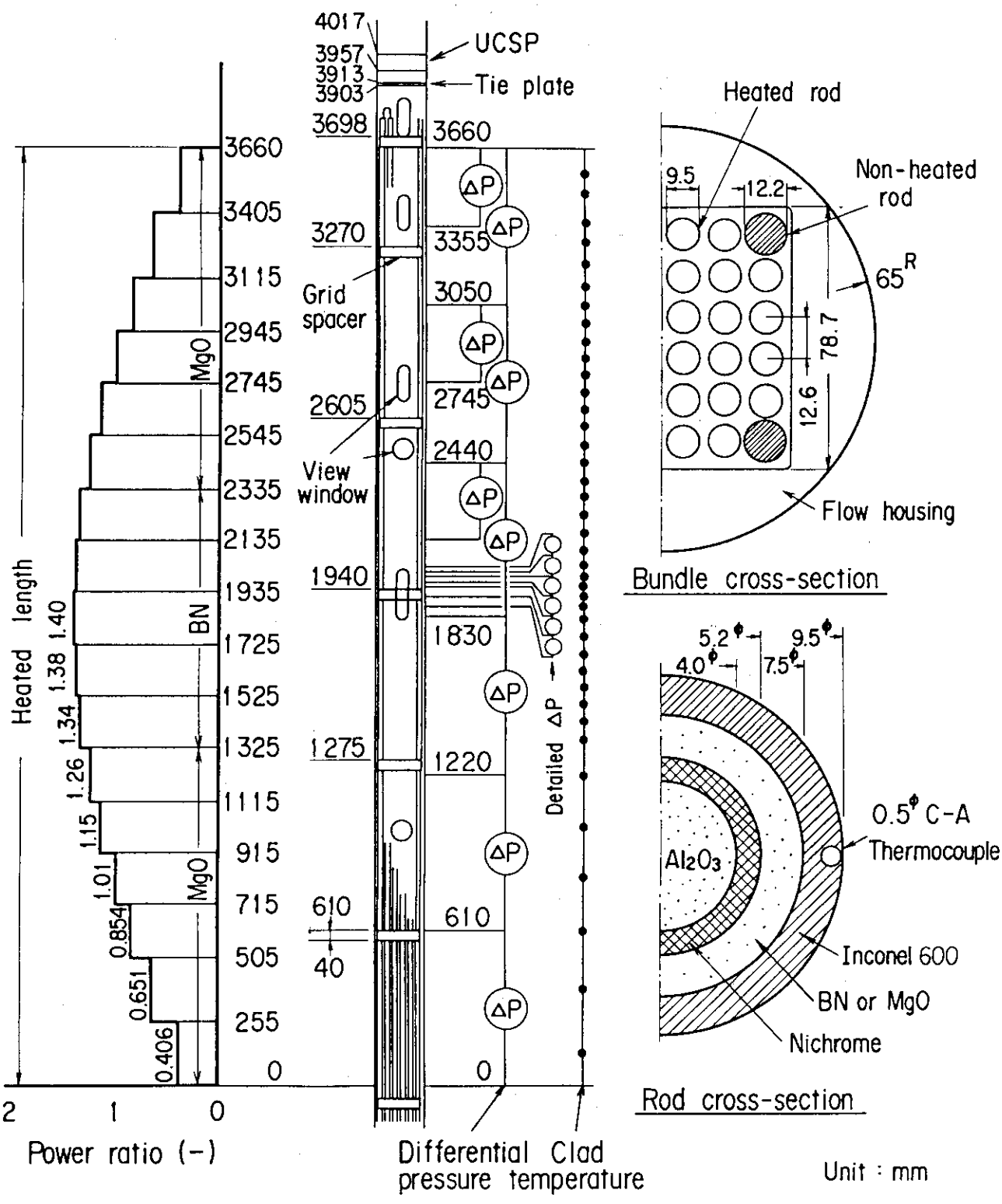

Fig. 3.11 Tet section and heater rod bundle

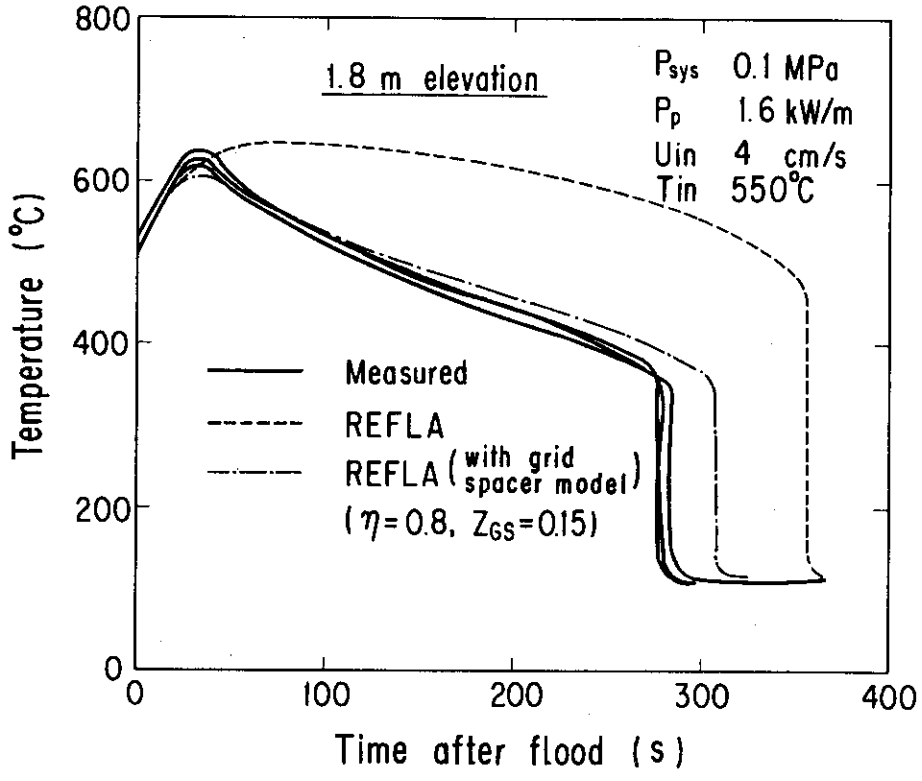

Fig. 3.12 Comparison of calculated and measured temperature histories at midplane above grid spacer (15x15 rod bundle geometry)

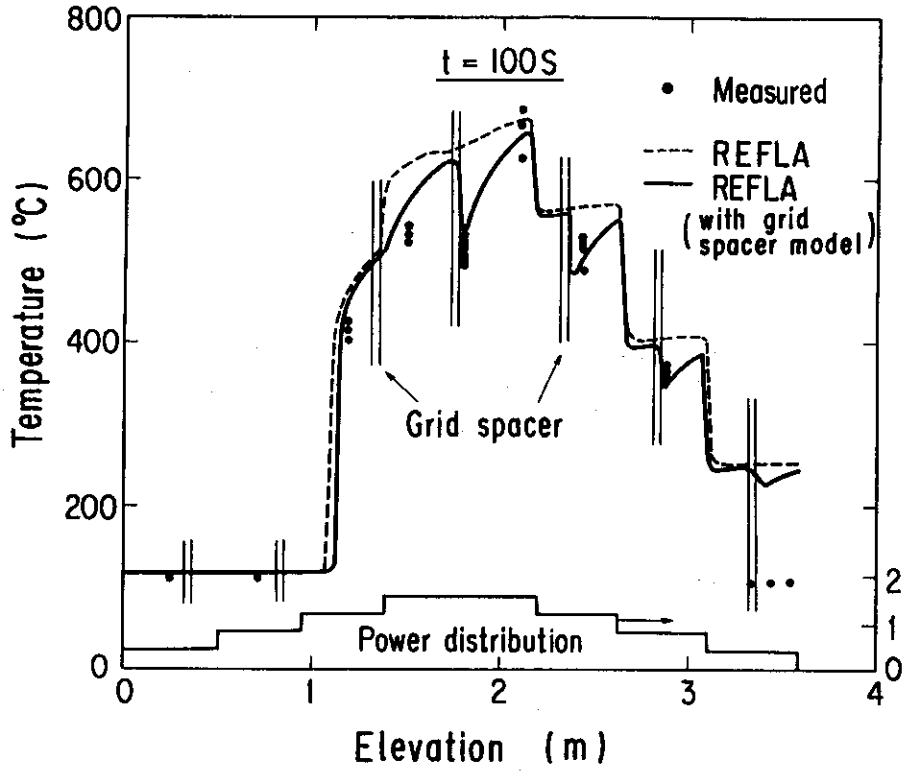

Fig. 3.13 Comparison of calculated and measured axial temperature distributions (15x15 rod bundle geometries)[at inverted slug flow condition]

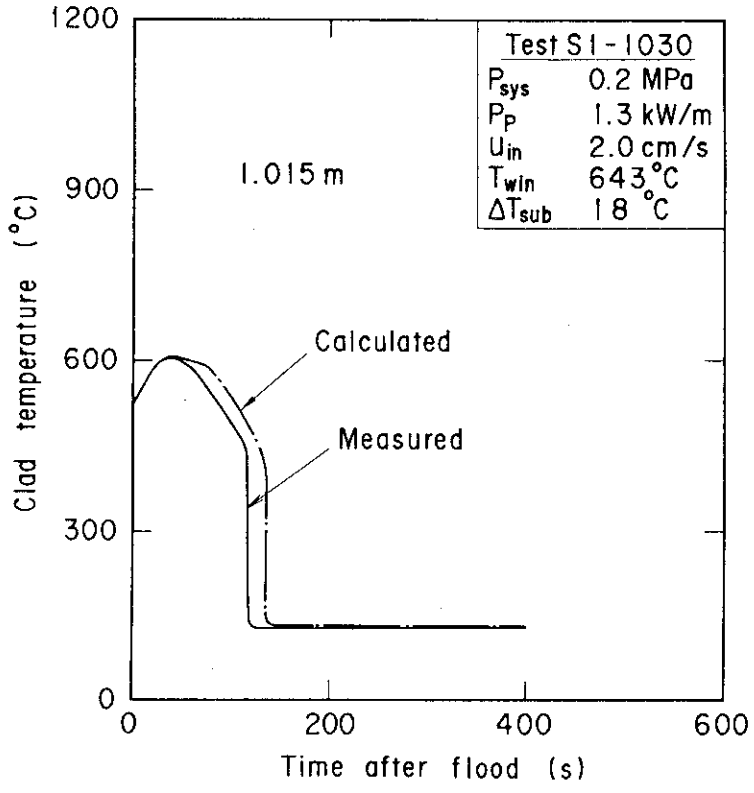

Fig. 3.14 Comparison of calculated and measured temperature histories at 1.015 m elevation (17x17 rod bundle geometry)

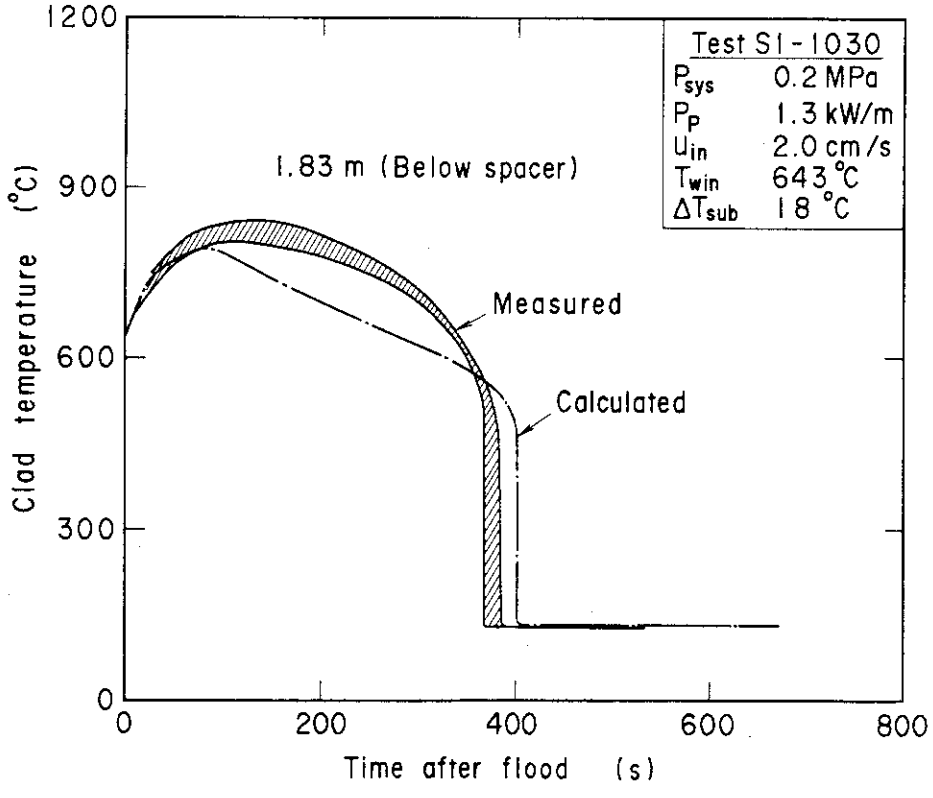

Fig. 3.15 Comparison of calculated and measured temperature histories at 1.83 m elevation (17x17 rod bundle geometry)

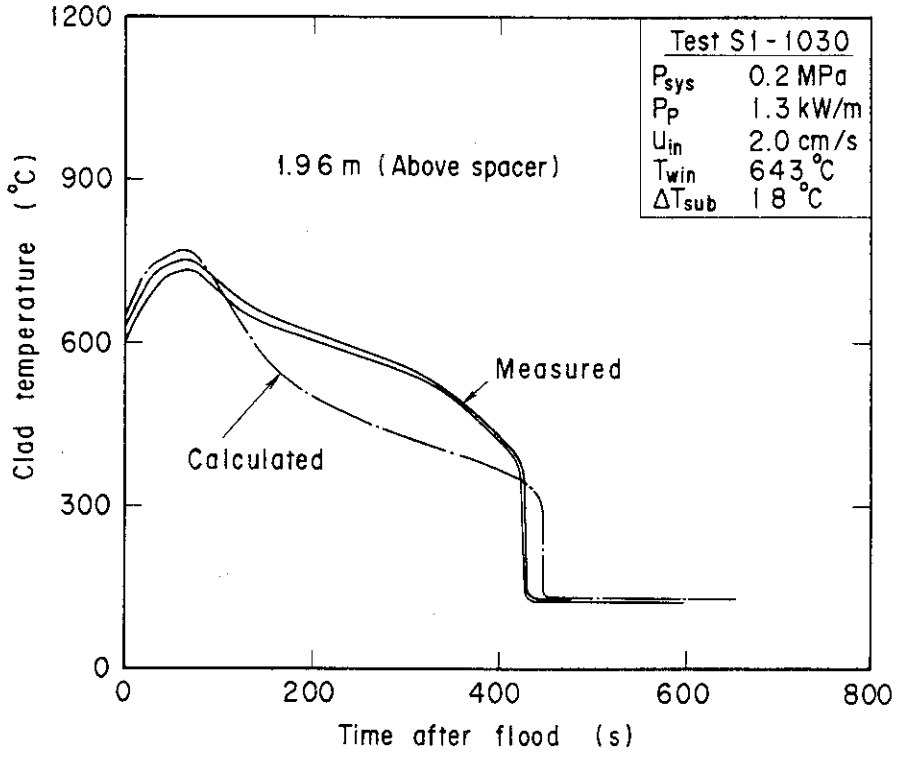

Fig. 3.16 Comparison of calculated and measured temperature histories at 1.96 m elevation (17x17 rod bundle geometry)

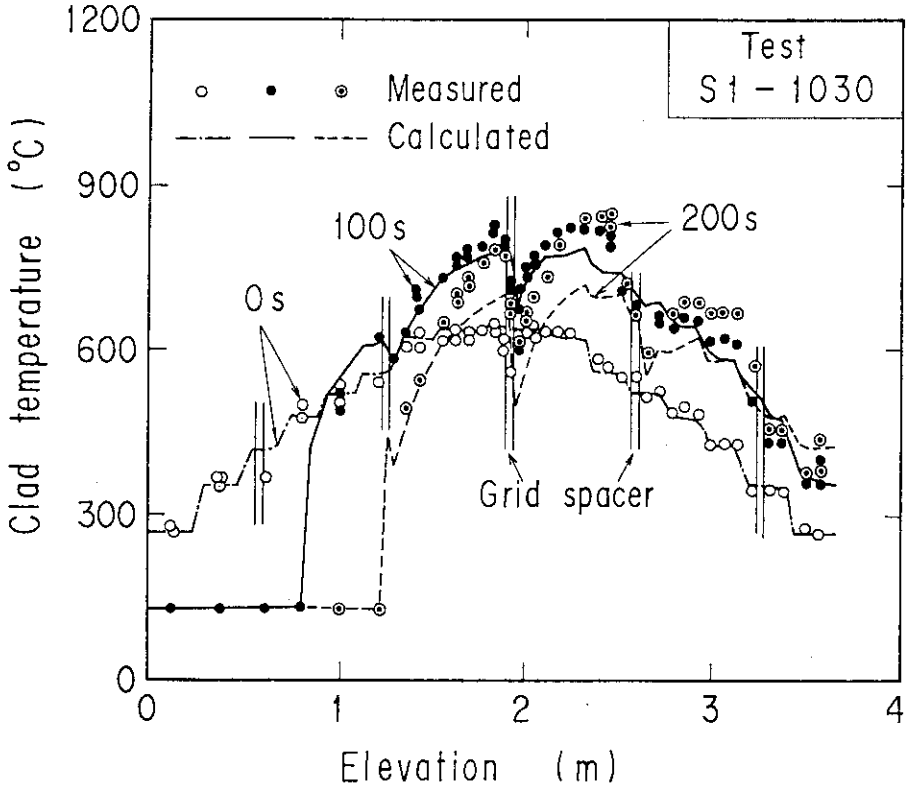

Fig. 3.17 Comparison of calculated and measured axial temperature distributions (17x17 rod bundle geometry)

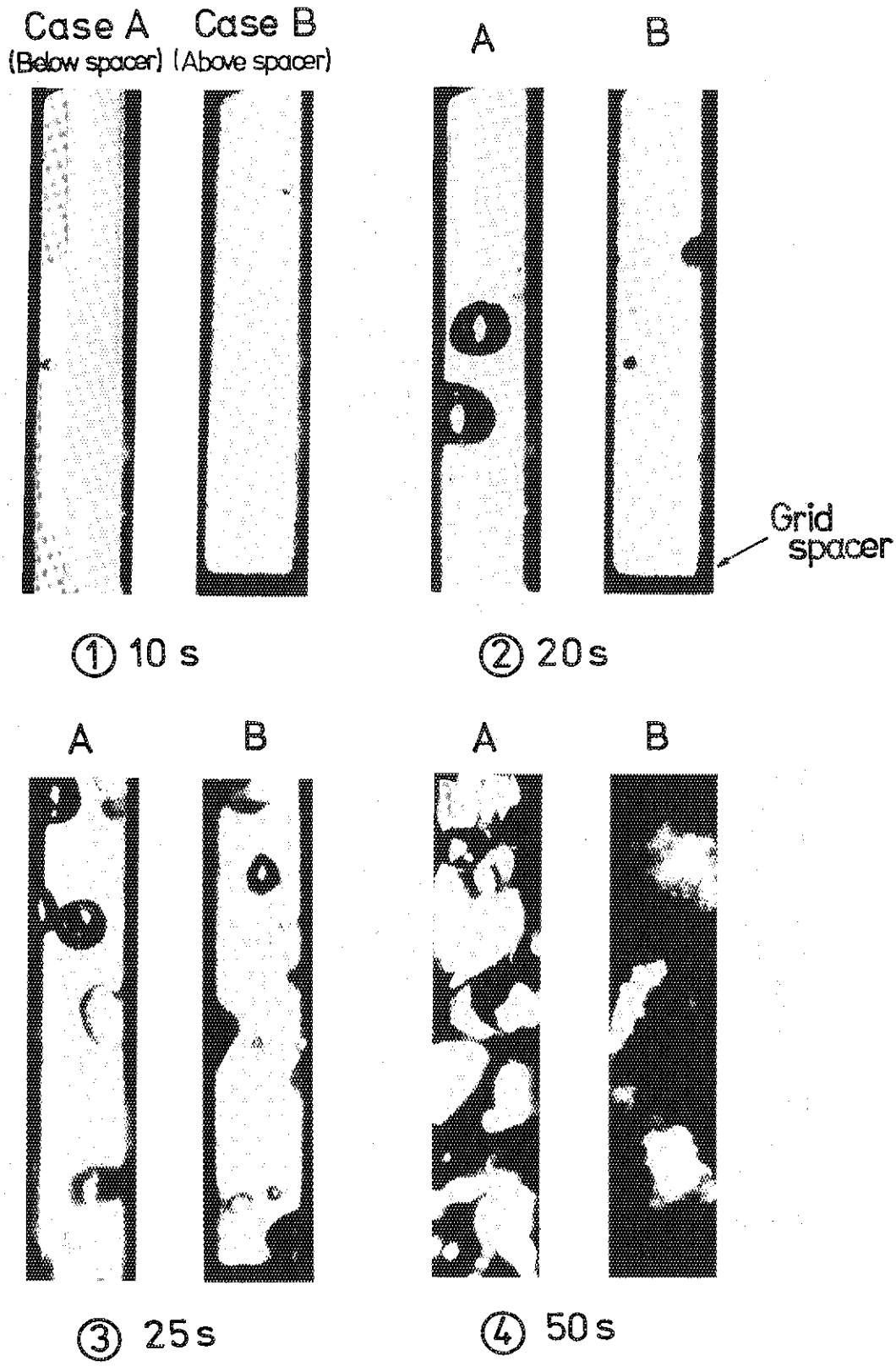

Photo. 3.1 Comparison of flow pattern between below and above the central grid spacer observed at midplane (15x15 rod bundle geometry; 16 mm movie camera)

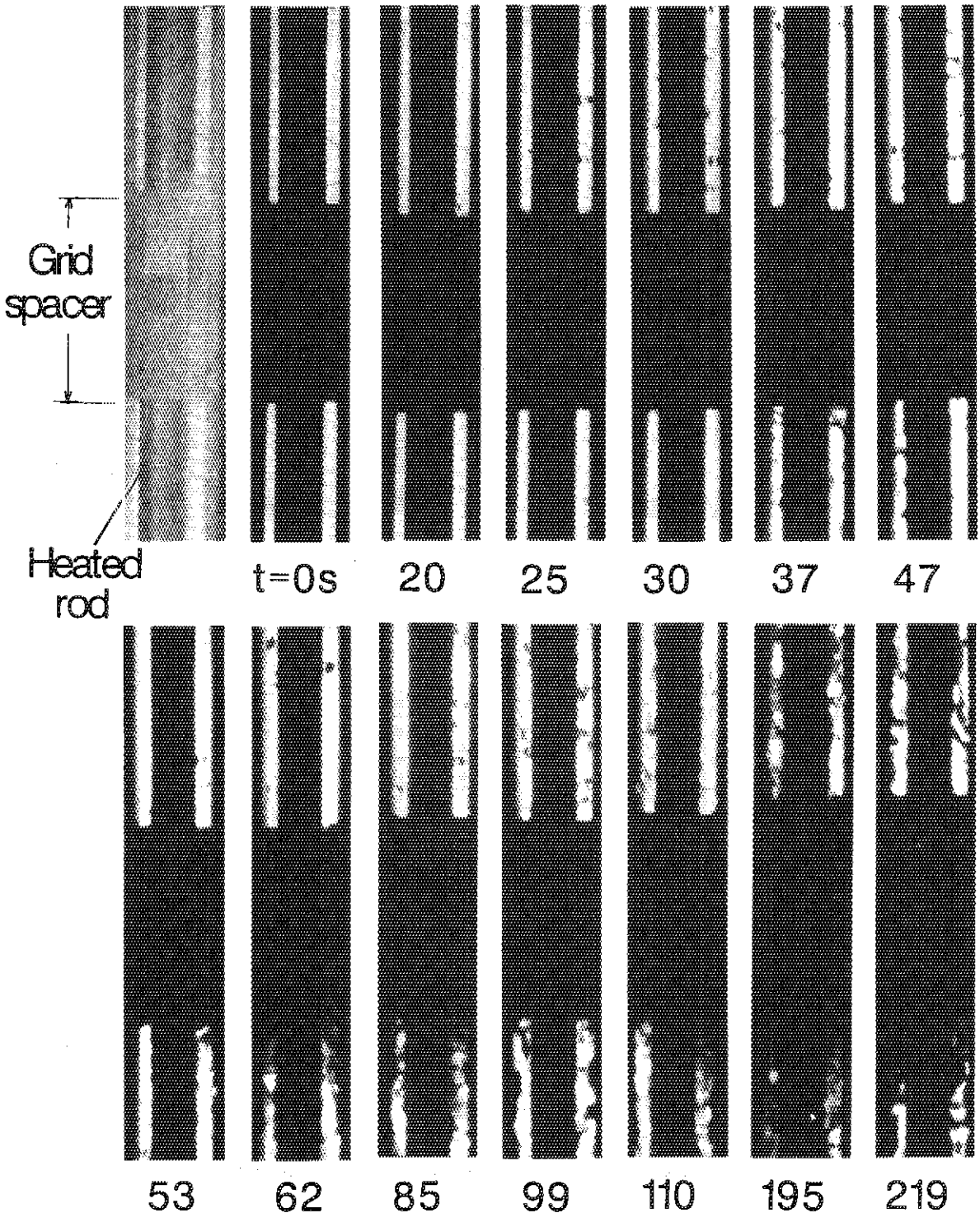

Photo. 3.2 Flow pattern near the central grid spacer (17x17 rod bundle geometry; 16 mm movie camera)

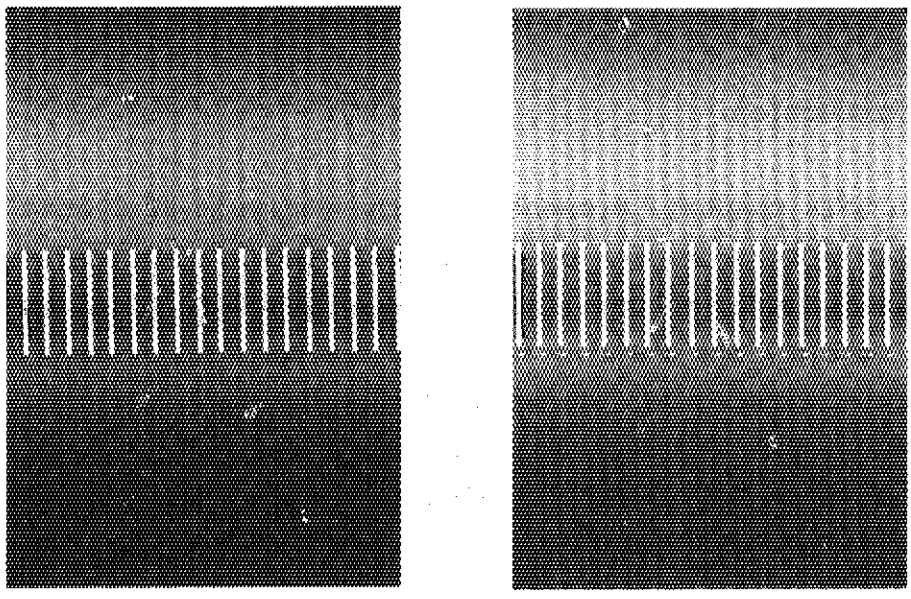

Case 1 (Split into two portions)
Strobe light t : 12 ms
Droplet diameter : 4.1 mm
Droplet velocity : 3.0 m/s

Case 2 (Droplet on spacer edge)
Strobe light t : 12 ms
Droplet diameter : 3.9 mm
Droplet velocity : 3.1 m/s

Photo. 3.3 Trace of water droplets obtained with streak camera (Model experiment)

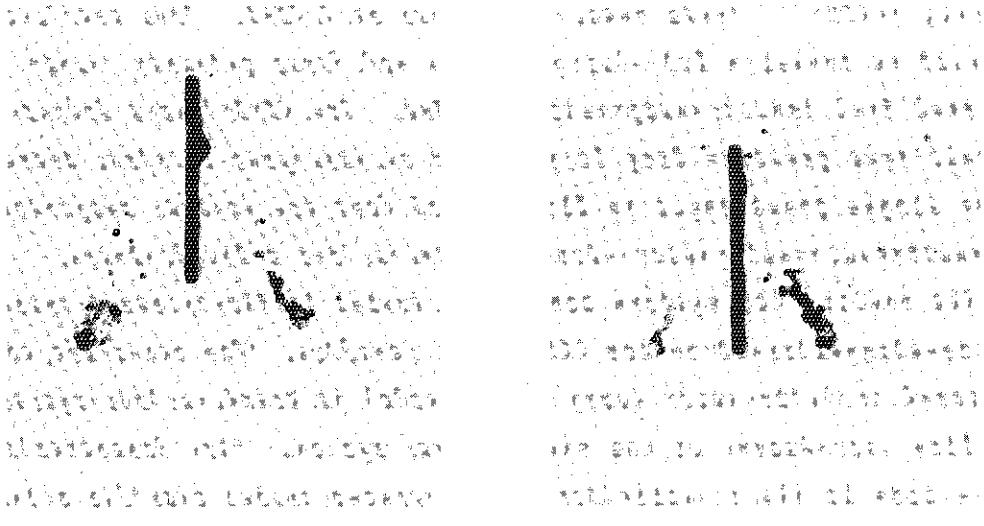

Case 1
Breakup into two major portions

Case 2
Breakup into large and small sizes of droplets with fine droplets

Photo. 3.4 Droplets breakup obtained with 16 mm movie camera (Model experiment)

4. Analysis of Thermo-hydraulic Behavior in Primary System[1]

4.1 Introduction

In this chapter, presented is the analysis of system thermo-hydraulic behavior using a system analysis code, which consists of the one-dimensional reflood analysis code REFLA-1D[2] and multi-loop system models. The coupling method of the core and system models, an application example and the calculated results are described. It has been shown that the core cooling during reflood is significantly enhanced with the higher flooding rate due to the increased vapor generation rate and liquid entrainment[3][4]. The flooding rate, on the other hand, is controlled by the balance between the driving head of the downcomer which forces the water into the core, and the back pressure in the upper plenum created by the steam-water mixture flowing from the core exit to the break. This back-pressure or "steam binding" tends to retard the core flooding rate during reflood phase. Thus the core thermo-hydraulics is strongly linked with the system thermo-hydraulics.

In order to investigate the core and system behaviors during reflood phase, the integral tests with the Cylindrical Core Test Facility (CCTF)[5] have been conducted at JAERI. The facility is designed to model a full-height core and four primary loops with simulated full active components of PWRs. The CCTF tests showed that the main loop pressure drop is realized at the pump section where the almost single phase vapor is flowing and that the system responses can be regarded as nearly quasi-steady state in the reflood phase.

The multi-loop system component model in the present code has been developed based on the CCTF test results. The coupling of the core model with the multi-loop system model is based on the equivalent loop flow resistance in the single loop system. The characteristics of the code is its simplicity of the system model and the solution method that enables the fast running of the code and the easy reflood analysis. The code can be utilized to improve and to testify the models as a pilot code for the further integral system analysis code.

4.2 Model description

In the present system analysis code, the coupling of the core and the multi-loop system component models is simply accomplished by the use of the equivalent K-factor in the single loop. This is based on the CCTF test results[5], i.e., the main loop pressure drop is realized at the pump section where the almost single phase vapor is flowing and the system responses can be regarded as nearly the quasi-steady state. This means that the loop flow resistance can be approximately expressed by an equivalent K-factor in the simplified single loop with the single phase vapor due to the slow transient in the reflood phase.

(1) Basic assumption

The present code utilizes the same scheme shown in Fig. 4.1 as in the REFLA-1D system code[6], in which the following are assumed:

i) Single phase liquid forms a U-tube column between the lower part of the core and the downcomer through the lower plenum.

ii) The motion of the water column in a reactor vessel is one-dimensional.

iii) Both ends of the water column are connected with a primary loop where the single phase vapor is flowing.

In the present code, the energy equation is considered for the multi-loop system in order to calculate the temperature of the two-phase flow. The mass and momentum equations are based on the single loop system shown in Fig. 4.1. The multi-loop system is related to the single loop system through the equivalent K-factor of the primary loop. This scheme allows a simple treatment of the solution of the momentum equation. The direct leak path or the vent valve path from the upper plenum to the downcomer can easily be modeled in this scheme. The core or system thermo-hydraulic model can easily be verified due to the simplicity and the fast running of the code.

(2) Basic equations

The basic equations for the single loop system shown in Fig. 4.1 are given in the following.

Conservation equations of the mass in the downcomer and the core are

$$W_D^I = A_D \rho_\ell \dot{x} + A_I \rho_\ell U_I + W_{\ell D} \tag{4-1}$$

$$A_I \rho_\ell U_I = A_c \rho_\ell \dot{y} + W_{gc}^o + W_{\ell c}^o \tag{4-2}$$

where W_D^I is the sum of the injected mass flow rate into the lower part of the downcomer; W_{gc}^o and $W_{\ell c}^o$ are the steam and liquid mass flow rates at the core outlet, respectively; The downcomer overflow rate $W_{\ell D}$ is expressed using the maximum downcomer length x_{max}. The time derivative of x is denoted by $\dot{x}$ in the above expression.

Conservation equations of the momentum in the primary loop, the downcomer, the lower plenum (downcomer-core connecting port) and the core are as follows;

$$P_U - P_s = (K_L/2\, \rho_{g\ sat})(W_L/A_L)^2 \tag{4-3}$$

$$\rho_\ell \frac{d}{dt}(x\dot{x}) = P_D - P_s - \rho_\ell g x - K_D(\rho_\ell/2)|\dot{x}|\dot{x} \tag{4-4}$$

$$\rho_\ell \frac{d}{dt}(L_I U_I) = P_D - P_I - K_I(\rho_\ell/2)|U_I|U_I \tag{4-5}$$

$$\rho_\ell \frac{d}{dt}(y\dot{y}) = P_I - P_U - \Delta P_U - \rho_\ell g y - K_c(\rho_\ell/2)\left|\frac{A_I}{A_C}U_I\right|\frac{A_I}{A_C}U_I \tag{4-6}$$

where L_I is the horizontal length between downcomer and core, and ΔPu is the differential pressure in upper plenum.

In the above formulation, the acceleration loss is neglected in the primary loop pressure drop, since the vapor density is much smaller than the liquid density in the reflood phase. The total frictional pressure loss is assumed to be represented by a K-factor loss coefficient.

In the upper plenum, the simple ideal gas equation is assumed for the saturated steam, i.e.,

$$V_U \frac{dP_U}{dt} = R\, T_U\, (W_{gc}^o - W_L) \tag{4-7}$$

where V_U and T_U are the volume and the temperature of the upper plenum, respectively, R the gas constant of the steam.

The unkown five variables in Eqs. (4-3) through (4-7) are combined into a vector X defined as

$$X = X(x,\ y,\ U_I,\ P_D,\ P_I) \tag{4-8}$$

The core outlet variables W^o_{gc} and $W^o_{\ell c}$ are calculated by the core component model, and the differential pressure ΔP_U in the upper plenum is calculated by the upper plenum component model. Also the injected mass flow rate W^I_D and the system pressure P_S are given as a boundary condition. Thus the simultaneous differential equations described above are solvable.

(3) Solution method

The basic equations given in Eqs. (4-1) through (4-7) can be converted into a simple form:

$$\begin{aligned}\ddot{x} = {} & \{P_U + \Delta P_U - P_S)/\rho_\ell + (y - x)g + \dot{y}^2 - \dot{x}^2 \\ & + \frac{1}{2}\left(K_I|U_I|U_I + K_C\left|\frac{A_I}{A_C}U_I\right|\frac{A_I}{A_C}U_I - K_D|\dot{x}|\dot{x}\right) \\ & + \frac{1}{g\,\rho_\ell}\left\{\left(\frac{L}{A_I} + \frac{y}{A_C}\right)\frac{d}{dt}W^I_D - \frac{y}{A_C}\frac{d}{dt}(W^o_{gc} + W^o_{\ell c})\right\} \\ & /\left(x + y\frac{A_D}{A_C} + L\frac{A_D}{A_I}\right),\end{aligned} \tag{4-9}$$

Here U_I can be expressed as a function of x using Eq. (4-1). Therefore, if we define the variable $y_i (i=1 \sim 4)$ such that,

$$y_1 = x,\ y_2 = \dot{x},\ y_3 = y,\ y_4 = P_u$$

Eqs. (4-1), (4-2), (4-7) and (4-9) can be written in the following form:

$$\frac{d}{dt}y_i = F_i(y_1,\ y_2,\ y_3,\ y_4) \tag{4-10}$$

This is a simultaneous differential equation concerning $y_i (i = 1 \sim 4)$. The Runge-Kutta-Gill method is adopted in the code to numerically solve the differential equation (4-10).

(4) Coupling of single and multi-loop system

The method of coupling of single and multi-loop systems is

described in the following. The schematic diagram is shown in Fig. 4.2. The single phase vapor is assumed to flow in the primary loop except for the broken cold leg nozzle. The pressure drop across the broken cold leg nozzle ΔP_{BCN} ($=P_S - P_O$) is calculated with the component model described in Appendix.

The differential pressure between the upper plenum and the upper part of the downcomer strongly affects the core flooding rate, and hence it must be conserved between the two schemes:

$$P_u - P_s = \frac{1}{2\rho_g} \cdot K_L \cdot \left(\frac{W_L}{A_L}\right)^2 = \frac{1}{2\rho_g} \cdot K_{Ii} \cdot \left(\frac{W_{Ii}}{A_{Ii}}\right)^2 \quad (i = 1 \sim N) \tag{4-11}$$

where K_L is the equivalent K-factor in the single loop system, K_{Ii} the K-factor of i-th intact loop and N the total number of the intact loops in the multi-loop system.

The total mass effluent rate from the upper plenum should also be conserved between the two scheme i.e.,

$$W_L = W_B + \sum_{i=1}^{N} W_{Ii} = W_B + W_I \quad . \tag{4-12}$$

The differential pressure between the upper plenum and the break location in the multi-loop system is expressed as,

$$\frac{1}{2\rho_g} K_B \left(\frac{W_B}{A_B}\right)^2 = \frac{1}{2\rho_g} K_{Ii} \left(\frac{W_{Ii}}{A_i}\right)^2 + \Delta P_{BCN} \quad . \tag{4-13}$$

The equivalent K-factor K_L of the single loop is easily derived from Eqs. (4-11) through (4-13) as,

$$K_L = K_I \frac{1}{\left[1 + \sqrt{\frac{K_I}{K_B}} \left(\frac{A_B}{A_L}\right) \sqrt{1 + \Delta P_{BCN} \Big/ \left\{\frac{1}{2\rho_g} K_I \left(\frac{W_I}{A_L}\right)^2\right\}}\right]^2} \tag{4-14}$$

where K_I is the K-factor of a combined intact loop defined by

$$\frac{1}{\sqrt{K_I}} = \frac{1}{A_L} \sum_{i=1}^{N} \frac{A_{Ii}}{\sqrt{K_{Ii}}} \quad . \tag{4-15}$$

The injected mass flow rate W_D^I in Eq. (4-1) is related to the mass flow rates of the multi-loop system as,

$$W_D^I = W_{ECCLP} + W_o + W_{FB} \quad , \tag{4-16}$$

where W_{ECCLP} is the mass injection rate into lower plenum, W_o the mass velocity from the downcomer annulas into downcomer, and W_{FB} the mass fall-back rate.

The calculation procedure used in the code is shown in Fig. 4.3. The system variable X in the single loop at time t + Δt is calculated by explicitly solving Eq. (4-10). The core outlet variables W_{gc}^o and $W_{\ell c}^o$ at the previous time t and the equivalent K-factor determined by Eq. (4-14) are used in this step. The multi-loop system variables at time t + Δt are then calculated by solving the mass and energy equations with the multi-loop system component model. Finally, the core thermo-hydraulic variables at time t + Δt are updated with the core model. In this step, the flooding rate W_c^I, the inlet water temperature $T_{\ell c}^I$ and the pressure at the core inlet P_I are used as a core inlet boundary condition.

(5) System component model

The primary loop system components modeled in the present system analysis code are the upper plenum, the coolant pump, the ECC injection port, the broken cold leg nozzle, the downcomer annulus and the downcomer. Each component model is formulated on the mass, momentum and energy balances. The present version selects the simplest model based on the characteristic features observed in the reflood system experiments[7][8]. The detailed description of each component model is given in Appendix of this paper.

4.3 Application to large-scale integral reflood test

In order to evaluate the dynamic and static characteristics of present system analysis code, the code was applied to a large-scale integral reflood test, Cylindrical Core Test Facility (CCTF)[5][8]. The CCTF at Japan Atomic Energy Research Institute has a four-loop

primary system with active steam generators and a full hight 2048 rod core. The general description of CCTF tests is given in this section.

(1) Test facility

The CCTF is designed to simulate the flow conditions in the primary system of a PWR during the refill and reflood phases of a LOCA. The vertical dimensions of the system components are nearly the same as those of a 1000 MW-PWR with four primary loops. The flow area of the system components is based on the core flow area scaling ratio of 1:21.4.

The pressure vessel consits of an annular downcomer, upper and lower plenums, and a non-nuclear core. The core has thirty-two 8x8 rod bundles. Figure 4.4 shows the cross section of the pressure vessel and the arrangement of the instrumented heater rods in the core. The core is divided into three power zones, namely A(high power), B(medium power) and C(low power) regions, respectively, as shown in the figure. In order to simulate a local powr distribution, a bundle is modeled with three types of heater rods, namely X, Y and Z rods, respectively. The heated length and the outer diameter of the heater rods are 3.66 m and 10.7 mm, respectively. The axial power profile is modeled with a 17 step chopped cosine, having the axial peaking factor of 1.49.

The facility has three intact loops and a broken loop. Each loop consists of hot leg and cold leg pipings, an active steam generator and a pump simulator. A 200% cold leg break is simulated for the broken cold leg. The broken cold leg is connected to two containment tanks. ECCS consists of an accumulator (Acc) and a low pressure coolant injection (LPCI) system. The injection points are at each cold leg and at the lower plenum. Figure 4.5 shows the schematic diagram of CCTF and the definition of the system variables. The scaled dimensions of the component are given in Table 4.1.

(2) Test procedure

The test procedures of the base case were as follows: The lower plenum was initially filled with saturated water to 0.9 m from the bottom of the vessel. The electric power was then applied to the heater rods in the core. When a specified clad temperature was reached, the injection of the Acc water into the lower plenum was

initiated. The power input to the rods began to decay at the reflood initiation when the water reached the bottom of the heated length of the heater rods (2.1 m from the bottom of the vessel). The injection port was changed from the lower plenum to the three intact cold leg ECC ports at about 5 s after the reflood initiation. At about 13 s, the ECC injection mode was changed from an accumulator (Acc) to a low pressure coolant injection (LPCI). These procedures are all for the reasonable simulation of the initial portion of reflood; otherwise the strong steam condensation would cause the unphysical pressure oscillation. The generated steam and the entrained water flowed via broken and intact loops to the containment tanks. The pressure of the containment tank was kept constant during the test. When all heater rod temperatures showed complete cooling of the core, the power supply to the heater rods was turned off, terminating the test.

(3) Test conditions

Table 4.2 gives the major test conditions for the CCTF base case test. In the CCTF parametric effect test series, only one test parameter was varied from the base case test. The test condition of the CCTF parametric effect tests in the present code application are shown in Table 4.3.

4.4 Calculated results and discussion

(1) Base case calculation

The base case calculation was performed in order to evaluate the thermo-hydraulic models used in the code and to further investigate the effect of the calculative parameters on the overall system responses. The analytical calculation performed was for CCTF Test C1-5, which is the base case test in CCTF Core I test series.

Overall system responses

The calculated flooding rate and collapsed water levels in the core, downcomer and upper plenum are compared with the measured data in Fig. 4.6. The flooding rate in the experiment was estimated with the mass balance in the system using the smoothed differential pressure measurement. As shown in Fig. 4.6, the calculated results

agree well with the measured data on an average. However, the calculated water level in the core before about 25 s is higher than the experiment. This is primarily due to the calculated lower steam generation rate and carry-over water before 25 s in the core region than the experiment. This then causes the smaller steam binding in the primary loop, resulting in the higher flooding rate into the core before 25 s than the experiment as shown in Fig. 4.6. The water accumulation in the upper plenum initiates after about 25 s, showing the delayed water carry-over at the exit of the core.

Figure 4.7 shows the calculated and measured pressure drops across the primary loop. The calculation generally agrees well with the measured on an average. The calculated broken and intact loop pressure drops are lower than the measured before about 25 s. This calculated smaller steam binding is again due to the smaller steam generation and carry-over in an early reflood transient.

Figure 4.8 shows the measured and calculated fluid temperatures at the core inlet. Although the calculated temperature is about 10 K lower than the measured, the overall tendency is well predicted. Also shown in the figure is the measured core inlet temperature in the CCTF test with the cold downcomer. The downcomer temperature of the cold downcomer test was about the saturation temperature. The calculated core inlet temperature agrees better with the case of the cold downcomer test after about 100 s through the transient. This is therefore due to the lack of the heat generation model from the downcomer wall in the present code. It is considered, however, that the effect of the inlet subcooling in this range is negligible on the overall core and system behaviors. The slightly higher core inlet temperature before 100 s is not fully understood. This is probably due to the unhomogeneous mixing of the water in a complicated configuration of the structure in the lower plenum, which is not modeled in the code.

Figure 4.9 shows the measured and calculated temperature histories of the heated rod in the core. The overall temperature histories are well prediced by the code. The calculted turnaround temperature is lower than the measured in the upper part of the core. It is considered that this is due to the sudden core cooling at about 10 s shown by an arrow in Fig. 4.9 due to the higher core flooding rate shown in Fig. 4.6. The calculated quench time tends to be

slightly later than the measured in the upper part of the core. This can be attributed to the lack of the appropriate top-down quenching model in the present code.

The void fraction in the core is shown in Fig. 4.10. The measured void fraction was obtained with the sectional differential pressure in the core neglecting the frictional pressure loss. The calculated void fraction shows good agreement with the measured except for the top part of the core. Before about 20 s of the transient, the calculated void fraction is much lower than the measured. This is due to the calculated higher initial core flooding rate shown in Fig. 4.6. The cause of the calculated smaller water accumulation in the top of the core is due to the core inlet flow oscillation, which tends to sweep the accumulated water in the region of the high void fraction.

Upper plenum de-entrainment

The effect of the de-entrainment coefficient η_U in Eq. (A-4) in Appendix on the water accumulation in the upper plenum was investigated. As shown in Fig. 4.11, the water accumulation in the upper plenum is lower with the larger η_U especially in the early reflood transient before about 150 s. However the effect of η_U is not sensitive in the range between 0.4 to 0.8. Also the effect of η_U on the core collapsed water level is almost negligible as shown in Fig. 4.11. The recommended value of 0.6[9] is adopted for η_D in the present base case calculation.

Loop K-factor

The loop K-factor K_{Li} in Eq.(A-12) in Appendix was parametrically varied in order to analytically estimate K_{Li} in CCTF. The loop pressure dorp is slightly higher with the higher loop K-factor as shown in Fig. 4.12. However the effect on the core cooling is not dominant as shown in the figure. The slightly worse core cooling for K_L=20 is due to the larger oscillation. The estimated loop K-factor is in the range between 20 to 30 according to the mass balance calculation. Tentatively a value of 25 is adopted in the base case calculation.

Downcomer carry-over

The downcomer carry-over coefficient η_{Do} in Eq. (A-21) in

Appendix was parametrically varied in the calculation. The carry-over in the downcomer, which may be the characteristic feature of the annular type downcomer as in a PWR vessel, is larger with the larger η_{Do} resulting in the lower water level in the downcomer as shown in Fig. 4.13. The calculation with η_{Do}=0.5 gives a better agreement with the measurement as shown in Fig. 4.13, and hence it is used in the calculation.

Broken cold leg

The K-factor of the broken cold leg nozzle K_{BCN} in Eq. (A-29) includes all the loss coefficients of the broken cold leg between the top part of the downcomer and the containment. The parametric calculation was performed to analytically estimate K_{BCN} in CCTF. As shown in Fig. 4.14, the value of 4.5 gives better agreement with the measured pressure drop across the broken cold leg.

Core inlet flow oscillation

The calculated core flooding rate generally oscillates in the present U-tube type schematic shown in Fig. 4.1. The source of the oscillation is the numerical fluctuation of the outlet variables such as W^{o}_{gc} and $W^{o}_{\ell c}$ in Eq. (4-2). This then causes the U-tube flow oscillation of the fluid between the downcomer and the core. The period of the oscillation is determined with the length of the liquid column. The oscillation can be enhanced due to the resonance of the U-tube flow and the core outlet flow oscillations.

Since the core model has been developed with the constant feed experiment, the oscillation with a small amplitude is favorable for the core thermo-hydraulic calculation. It is considered that the flow oscillation in the core is effectively damped in an actual reactor vessel due to the three-dimensional configuration. However, the typical value of the amplitude is uncertain.

The parametric calculation was performed in order to investigate the effect of the flow oscillation on the core heat transfer. In the calculation, the primary system was decoupled and the oscillatory core inlet flow was fed as a core boundary condition. The amplitudes of the oscillation tested were 0, 2 and 4 cm/s and the periods of the oscillation were 3 and 5 sec with the average flooding rate of 3 cm/s.

As shown in Fig. 4.15, the calculated maximum temperature is higher with the larger amplitude, but it is only slightly higher with

the shorter period of oscillation. The quench time tends to be later with the larger amplitude in the upper part of the core. According to the experiments at ERSEC[10], the core heat transfer is not much affected by the flow oscillation. By comparing the calculation with the temperature transient obtained in CCTF test, it is indicated that the large core inlet flow oscillation should be avoided to reasonably predict the temperature response with the present core model.

(2) Parametric effect

The parametric calculation was performed in order to evaluate the thermo-hydraulic models concerning the parametric effect of the system variables on the reflood behaviors. The analytical calculation performed was for CCTF parametric effect tests lited in Table 4.3.

System pressure

Figure 4.16 shows the effect of the system pressure on the differential pressure across the loop. As shown in the figure, the loop pressure drop is lower with the higher system pressure primarily due to the larger vapor density. Although the calculated loop pressure drop is lower before about 50 s than the measured, the overall tendency is well predicted by the code on an average.

The quench envelope in the core is compared with the data in Fig. 4.17. The core cooling is enhanced with the larger system pressure both in the experiment and the calculation. The quench time at the midplane (1.83 m) is fairly well predicted. However the calculated quench time tends to be slightly later in the upper part of the core. It is considered that this is due to the effect of the top-down quenching observed in the test, which is not effectively modeled in the present core model. However, this is not a fatal problem for the safety analysis, since the bottom quenching region is dominant where the peak clad temperature is realized.

ECC flow rate

Figure 4.18 shows the effect of the ECC flow rate on the collapsed water level in the downcomer. The ECC flow rate affects the water accumulation in the downcomer. As shown in Fig. 4.18, the water level in the downcomer is higher with the higher LPCI flow rate. The observed water accumulation in CCTF downcomer is well predicted as

shown in Fig. 4.18.

Initial peak clad temperatrue

Figure 4.19 shows the effect of the initial peak clad temperature on the temperature history at the midplane. The higher initial peak clad temperature resulted in the higher turnaround temperature and the later quench time as show in Fig. 4.19. Although the calculated quench time agrees well with the measured, the calculated turnaround temperature is underpredicted. This is partly because of the higher initial flooding rate and partly because of the overpredicted heat transfer coefficient near the turnaround. Therefore the heat generation in an early transient and also the heat transfer model should be reviewed in detail for the better prediction.

4.5 Summary

(1) The system analysis code was developed for the analysis of the system thermo-hydraulic behaviors during reflood. The code consists of a one-dimensional non-equilibrium two-phase flow core model and a multi-loop system model. The system components modeled are upper plenum, downcomer, ECC injection port and broken cold leg nozzle. The coupling between the one-dimensional core model and the multi-loop system model is accomplished by the use of the equivalent flow resistance in a single loop with saturated steam.

(2) The code was applied to the Cylindrical Core Test Facility (CCTF) tests. A fairly good agreement with experiments was obtained for the water accumulations in the downcomer, core and upper plenum, and for the thermo-hydraulic behavior in the core. Also obtained was a qualitatively good agreement for the parameters of the system pressure, ECC flow rate and the initial clad temperature.

(3) Several shortcomings of the code, however, were pointed out for further code improvements based on the present analytical investigation by comparing calculation with CCTF data. For the application to an actual PWR, it is further necessary to model the nuclear fuel such as the gap conductance between the cladding and the fuel element, which could affect the quench front movement. This will be discussed in chapter 5.

Reference

(1) Sugimoto, J., et al.: JAERI-M 83-147, (1983).
(2) Murao, Y.: J. Nucl. Sci. Technol., 16[11], 802 817 (1979).
(3) Murao, Y., et al.: JAERI-M 6982 (in Japanese)(1977).
(4) Cermak, J.O., et al.: WCAP-7435, (1970).
(5) Murao, Y., et al.: JAERI-M 82-073 ,(1982).
(6) Murao, Y. and Sugimoto, J.: JAERI-M 9780, (1981).
(7) Waring, J.P., et al.: WCAP-8583, (1975).
(8) Murao, Y., et al.: J. Nucl. Sci. Technol., 19[9] pp.705 719 (1982).
(9) Iguchi, T., et al.: J. Nucl. Sci. Technol., 20[6], 453 466 (1983).
(10) Clement, P., et al.: Presented at European Two Phase Flow Group Meeting, Paris, (1982).

Table 4.1 Scaled dimensions of the CCTF components

	PWR	CCTF	Ratio
‹ Length(m) ›			
Heated length	3.66	3.66	1/1
Diameter of heated rod	10.7×10^{-3}	10.7×10^{-3}	1/1
Diameter of non-heated rod	13.8×10^{-3}	13.8×10^{-3}	1/1
Rod pitch	14.3×10^{-3}	14.3×10^{-3}	1/1
Distance from the bottom of cold leg nozzle to the bottom of the heated core	4.849	4.849	1/1
Distance from the top of the heated core to the top of the core support plate	0.357	0.357	1/1
Downcomer length	6.066	6.066	1/1
Distance from the bottom of the vessel to the bottom of the heated core	-	2.1	
‹ Flow area (m^2) ›			
Core	5.29	0.260	1/20.3
Downcomer	2.47	0.197	1/21.4
Core baffle	1.76		
Upper plenum	11.10	0.678	1/16.4
Containment tank 1	-	4.906	
Primary loop	0.487 0.383	0.019	1/25.8 1/20.3
‹ Volume (m^3) ›			
Lower plenum*	29.6	1.38	1/21.44
Upper plenum	43.6	2.04	1/21.44

* included the downcomer region below the bottom of core.

Table 4.2 Test conditions of the CCTF base case test

Item	Values
System pressure	0.2 MPa
Initial average linear power	1.4 kW/m
Radial power factor	1.15
Axial power factor	1.49
Local power factor	1.1
Total peaking factor	1.885
Decay curve of power	Based on ANS-5.1 standard*
Maximum initial clad temperature	873 K
Downcomer wall temperature	471 K
Other wall temperature	392 K
Steam generator secondary side water temperature	538 K
K factor of primary loop	25
ECC injection conditions	
Acc flow rate	$7.78 \times 10^{-2} m^3/s$
Acc water temperature	308 K
Acc injection period	14 sec
LPCI flow rate	$8.33 \times 10^{-3} m^3/s$
LPCI water temperature	308 K

Note * ANS-5.1:Decay Energy Release Rates following Shutdown of Uranium-fueled Thermal Reactors, October(1971).

Table 4.3 Parametric effect tests in CCTF

Test parameter		Test number
System pressure (MPa)	0.15	C1-10
	0.20	C1-5
	0.30	C1-12
ECC injection rate ($x10^{-3} m^3/s$)		
Acc	77.2(x14 s)	C1-5
LPCI	8.3	
High LPCI	17.2	C1-6
Low LPCI	4.7	C1-9
Initial peak clad temperature (K)	873	C1-5
	973	C1-7
	1073	C1-14

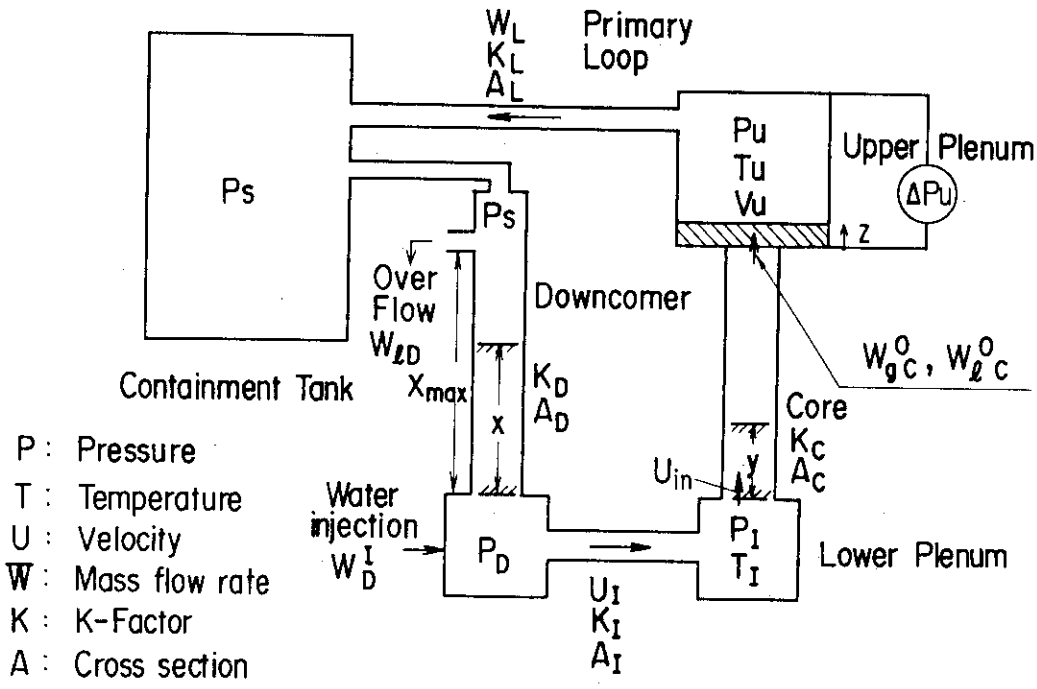

Fig. 4.1 Schematic of one-dimensional system

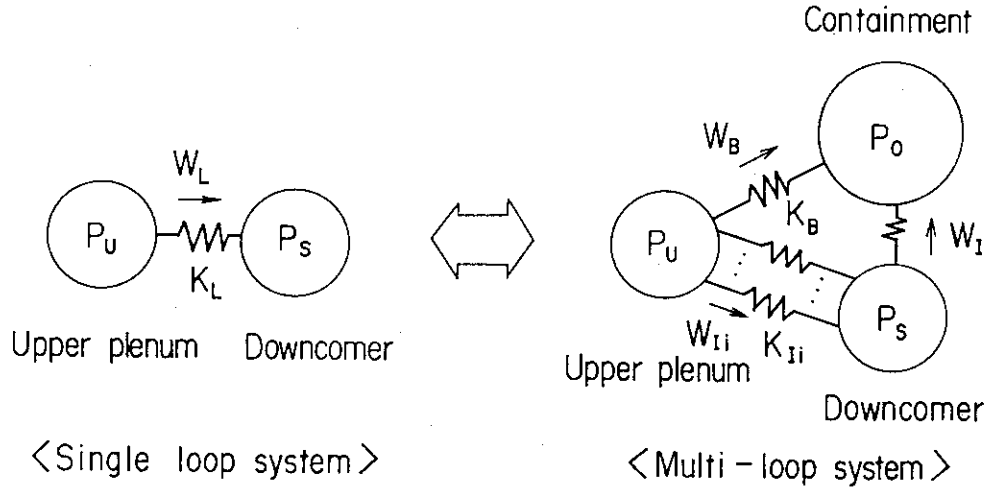

Fig. 4.2 Coupling of single and multi-loop system

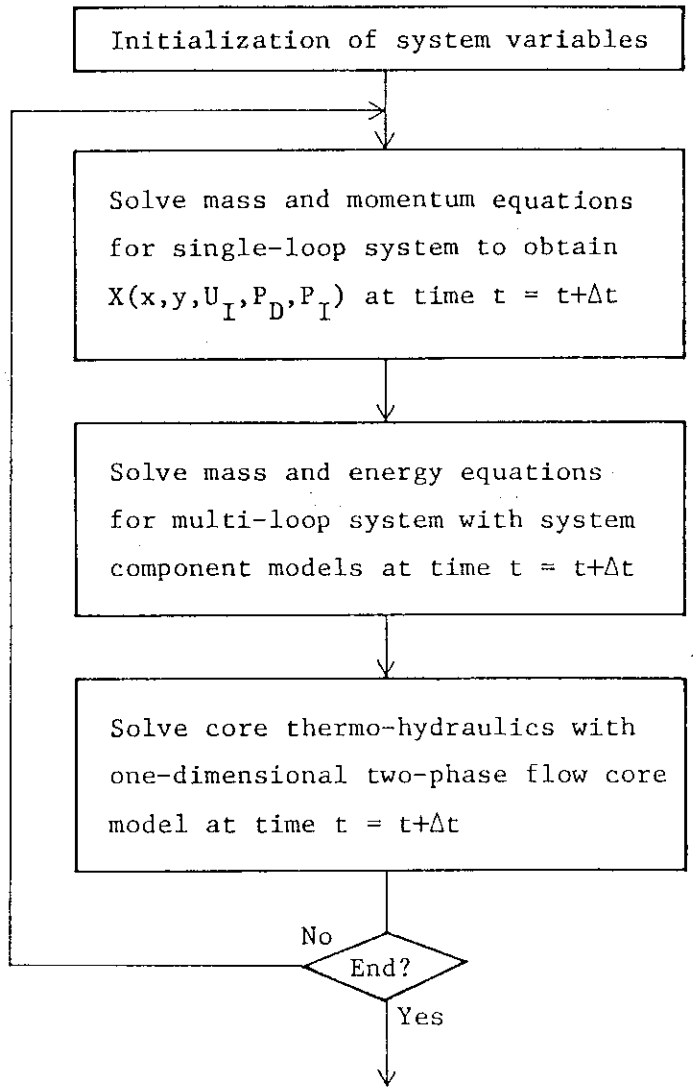

Fig. 4.3 Flow diagram of calculational procedure

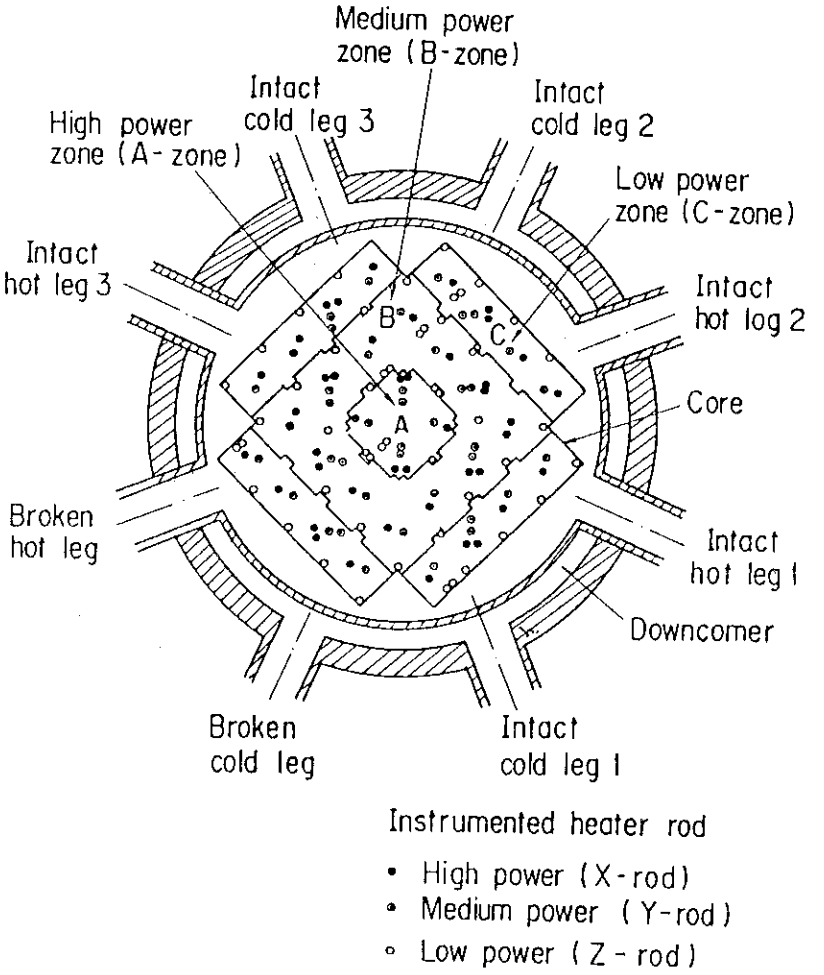

Fig. 4.4 Cross section of CCTF pressure vessel

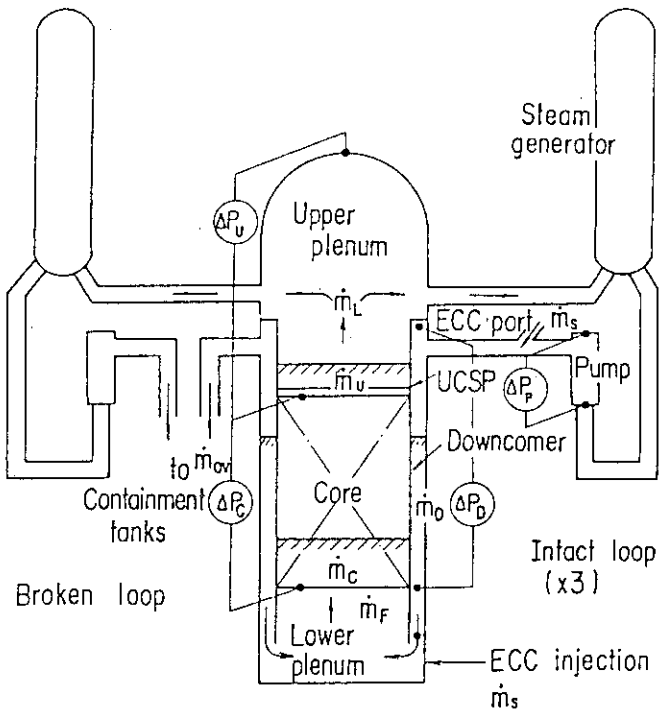

Fig. 4.5 Schematic of CCTF system and locations of differential pressure measurement

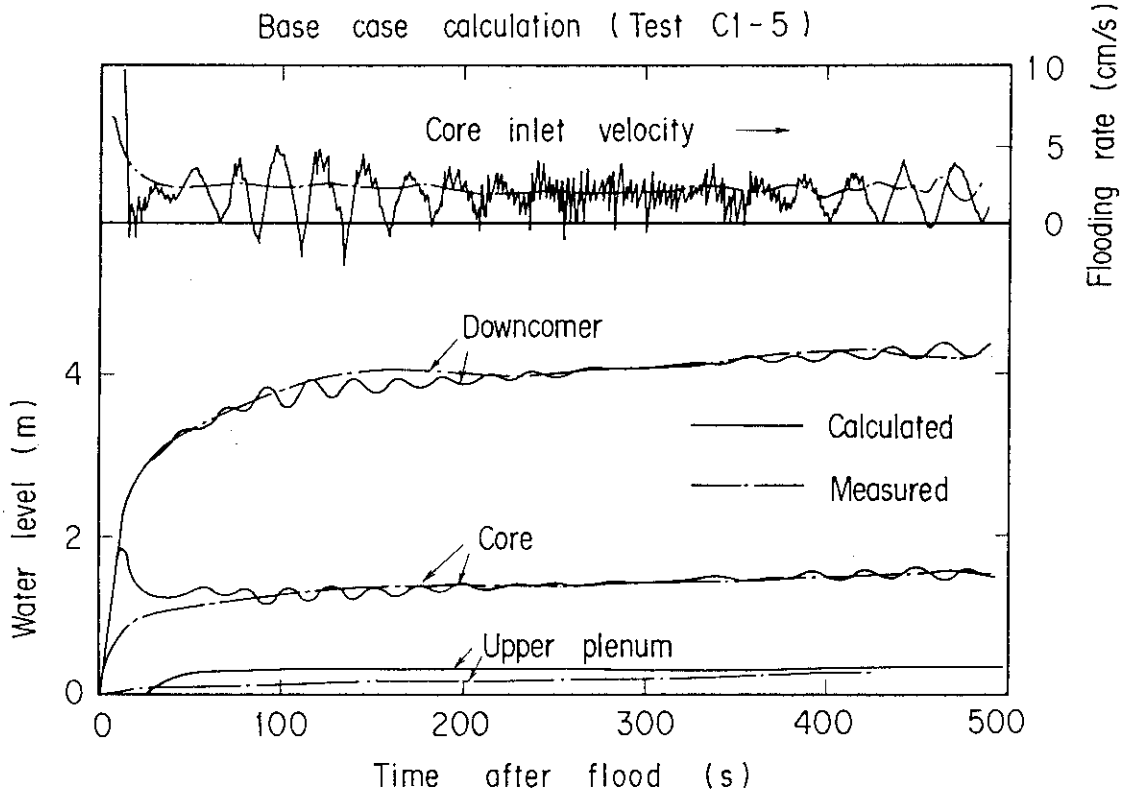

Fig. 4.6 Core flooding rate and water levels in base case calculation

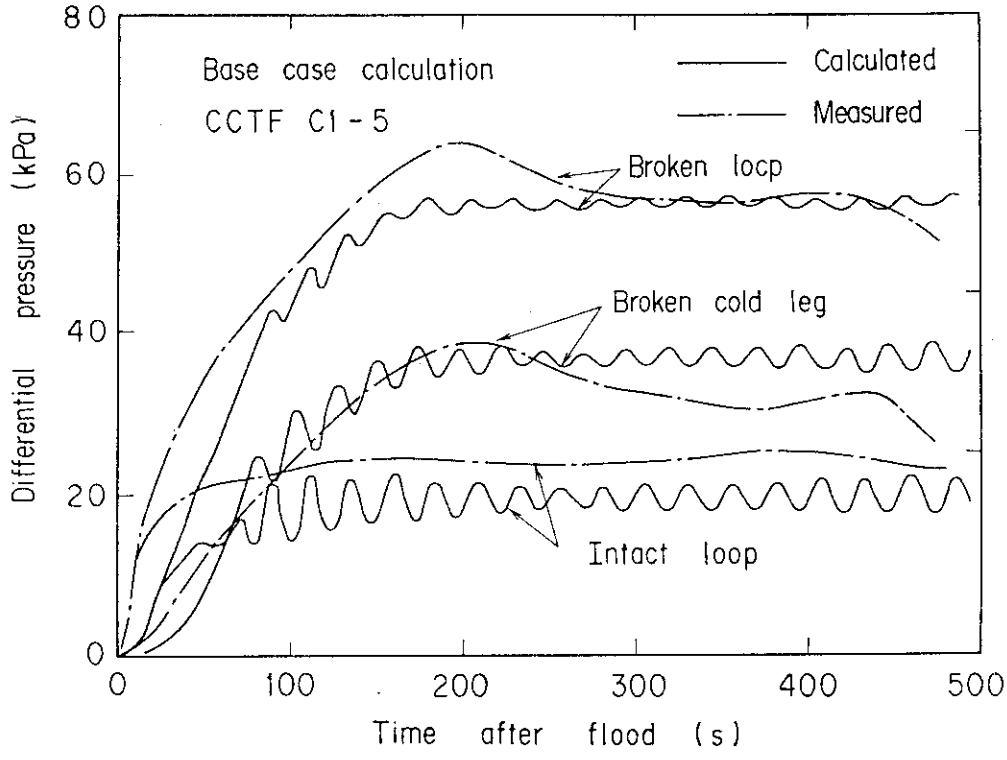

Fig. 4.7 Loop pressure drops in base case calculation

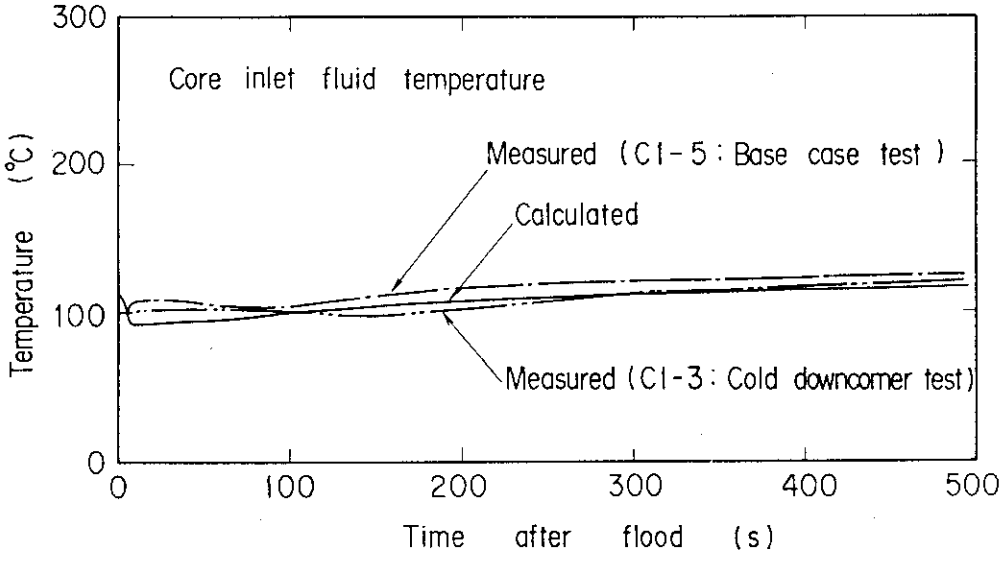

Fig. 4.8 Fluid temperature at core inlet in base case calculation

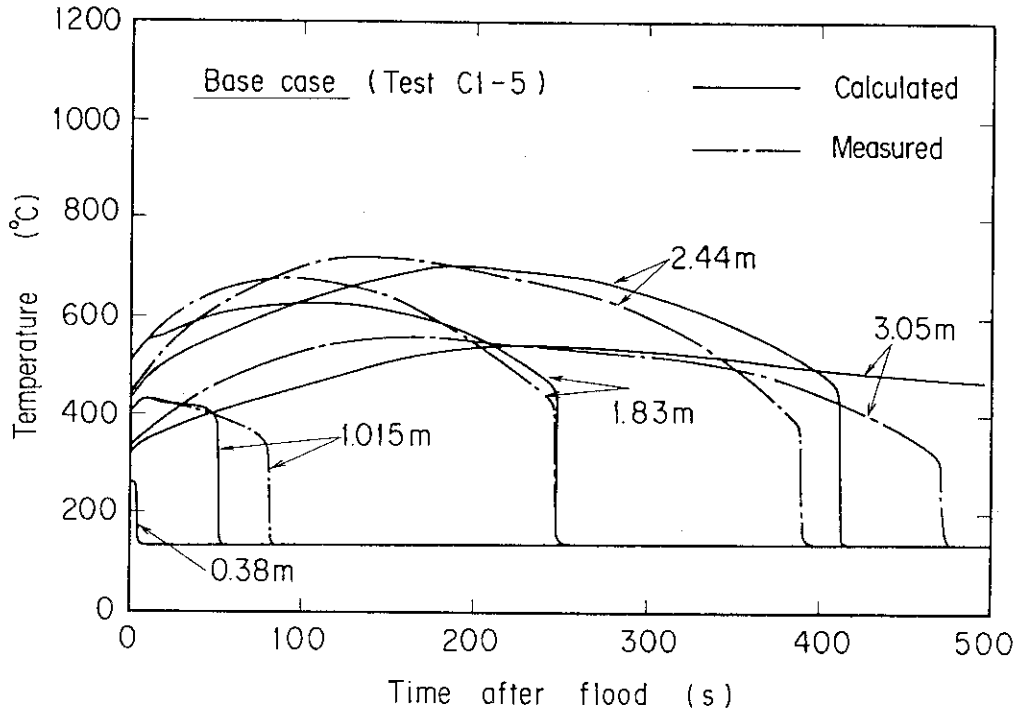

Fig. 4.9 Clad temperature in core in base case calculation

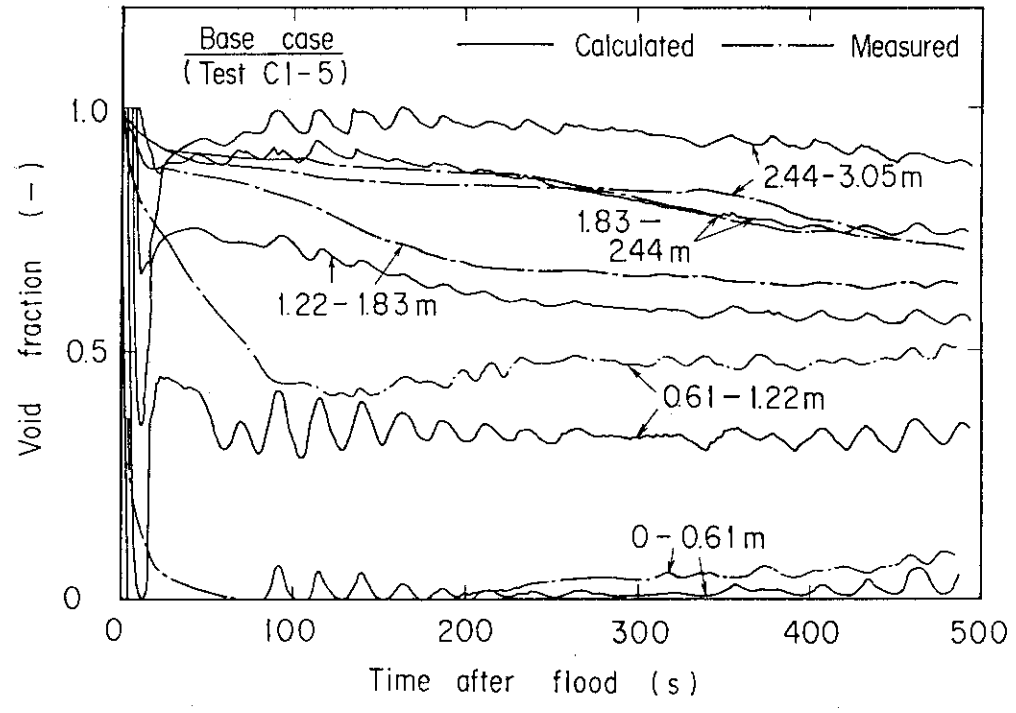

Fig. 4.10 Void fraction in core in base case calculation

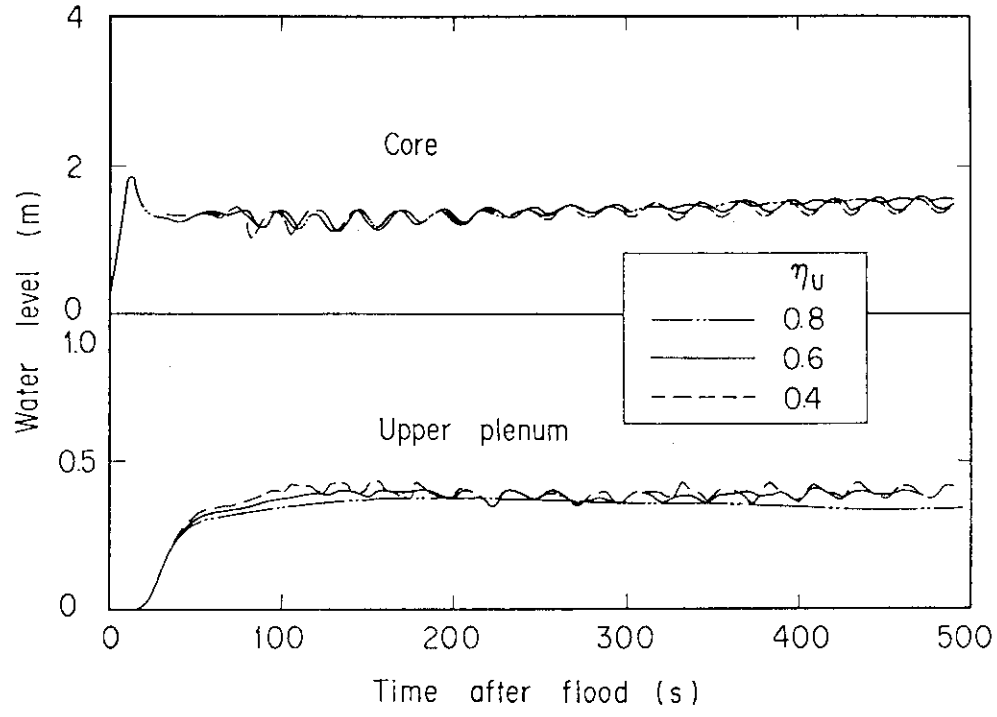

Fig. 4.11 Effect of de-entrainment coefficient on water accumulation in upper plenum

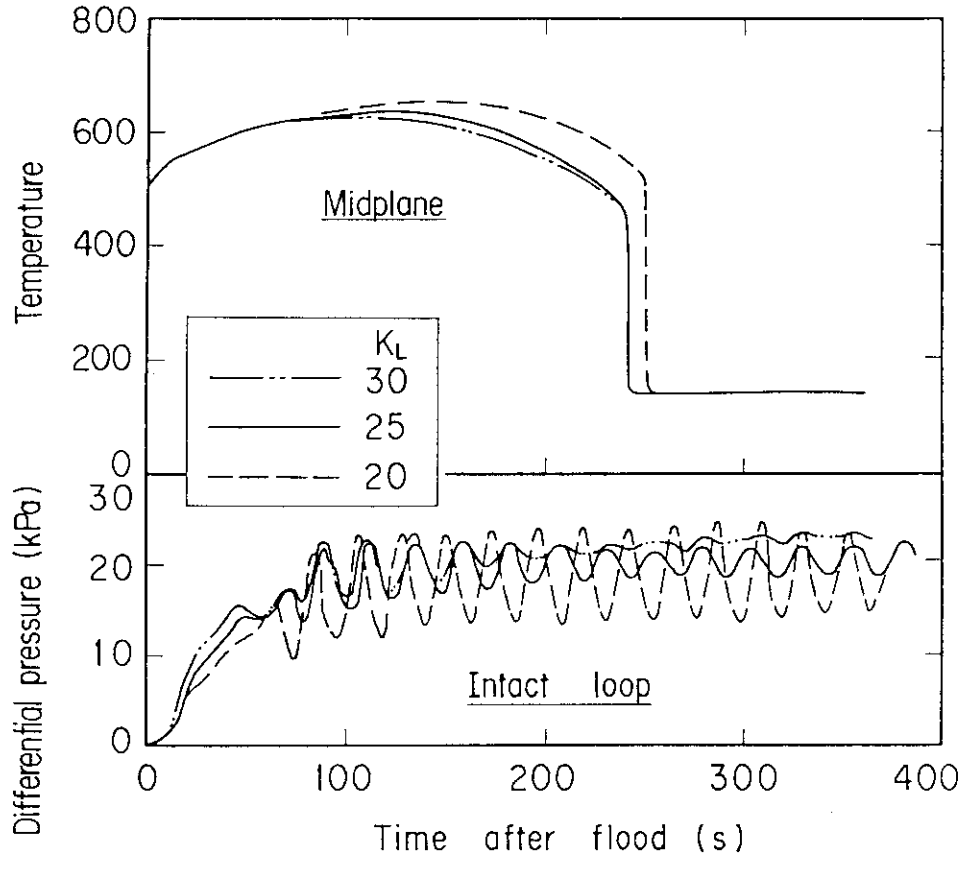

Fig. 4.12 Effect of loop K-factor on core cooling and loop pressure drop

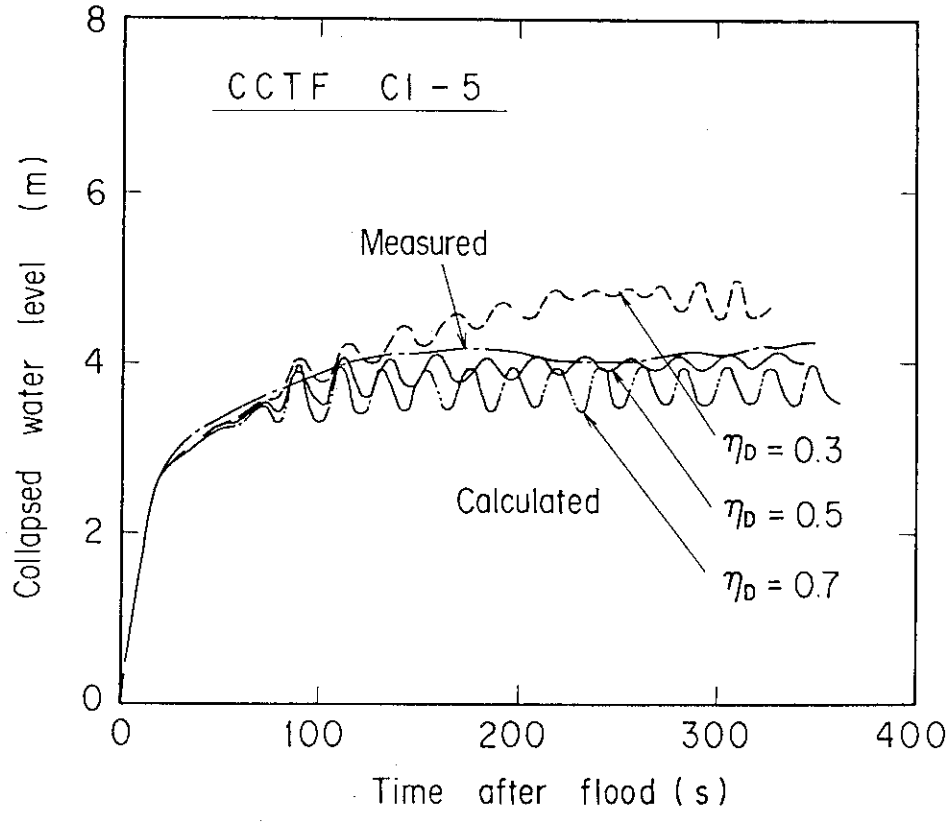

Fig. 4.13 Effect of downcomer carry over coefficient on water level in downcomer

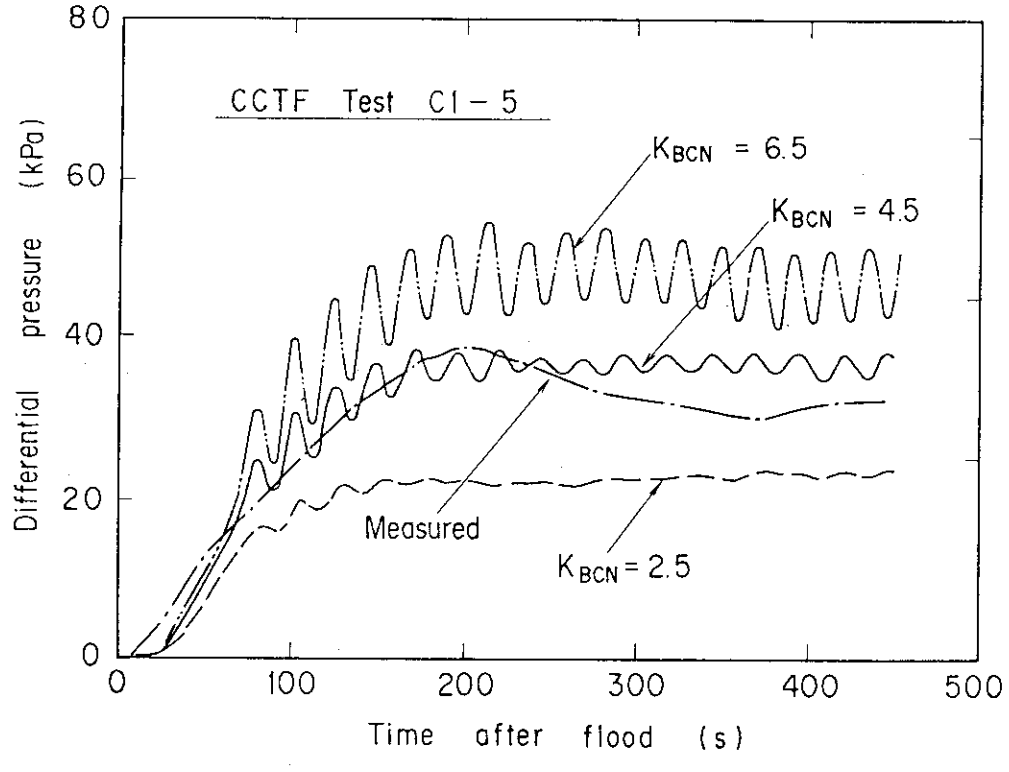

Fig. 4.14 Effect of K-factor of broken cold leg on broken cold leg pressure drop

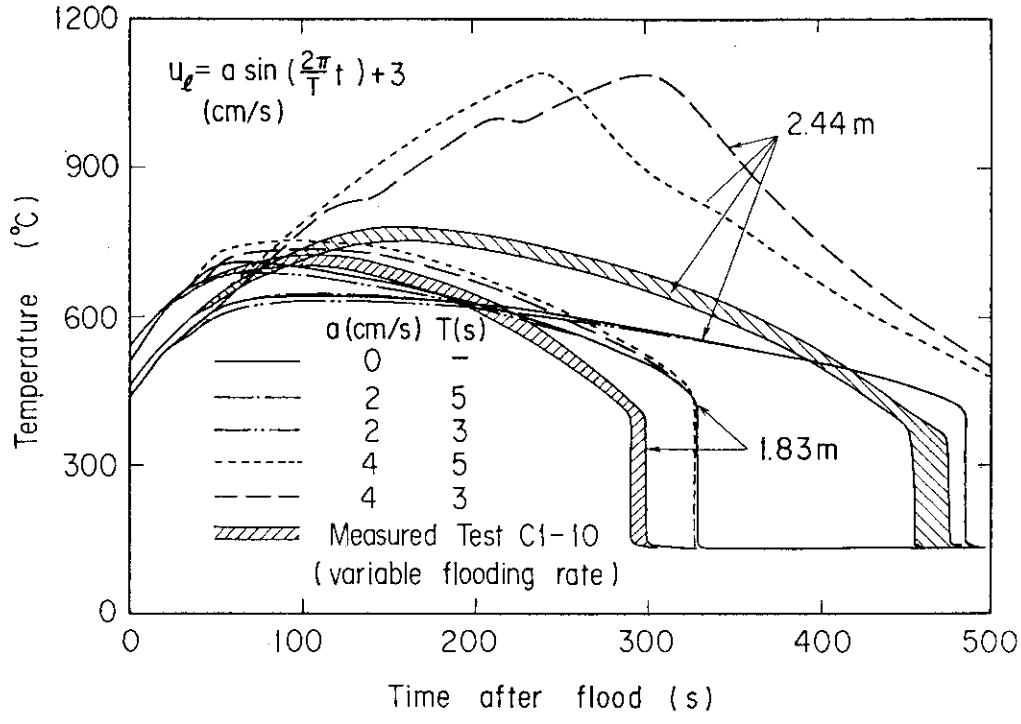

Fig. 4.15 Effect of oscillation on core cooling

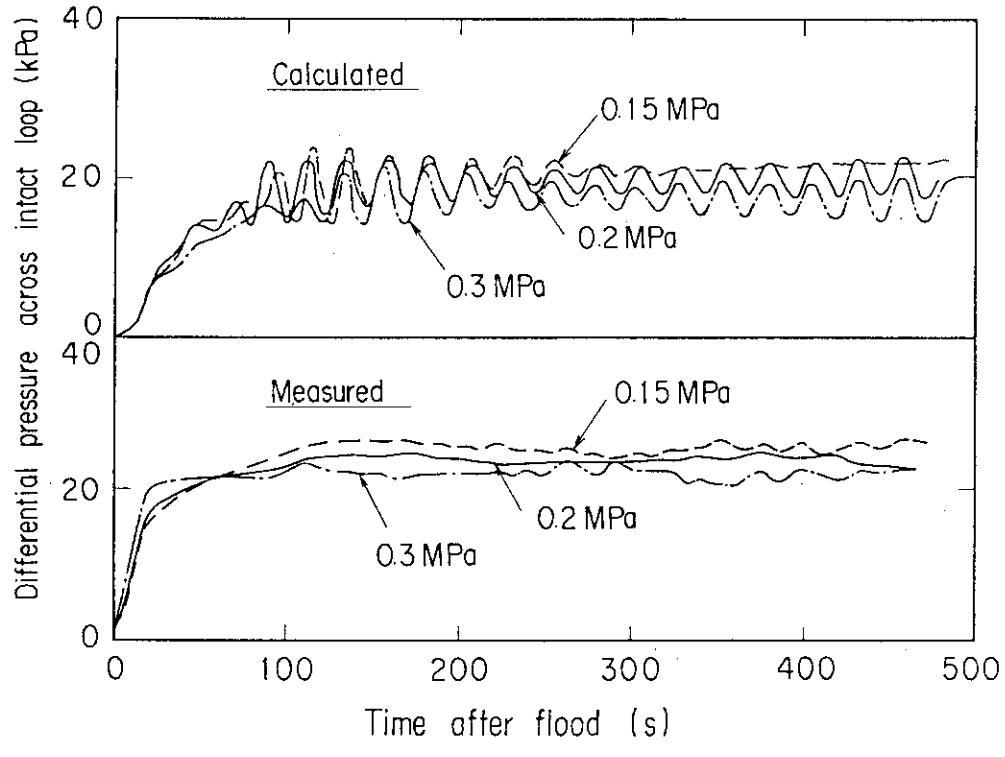

Fig. 4.16 Effect of system pressure on intact loop pressure drop

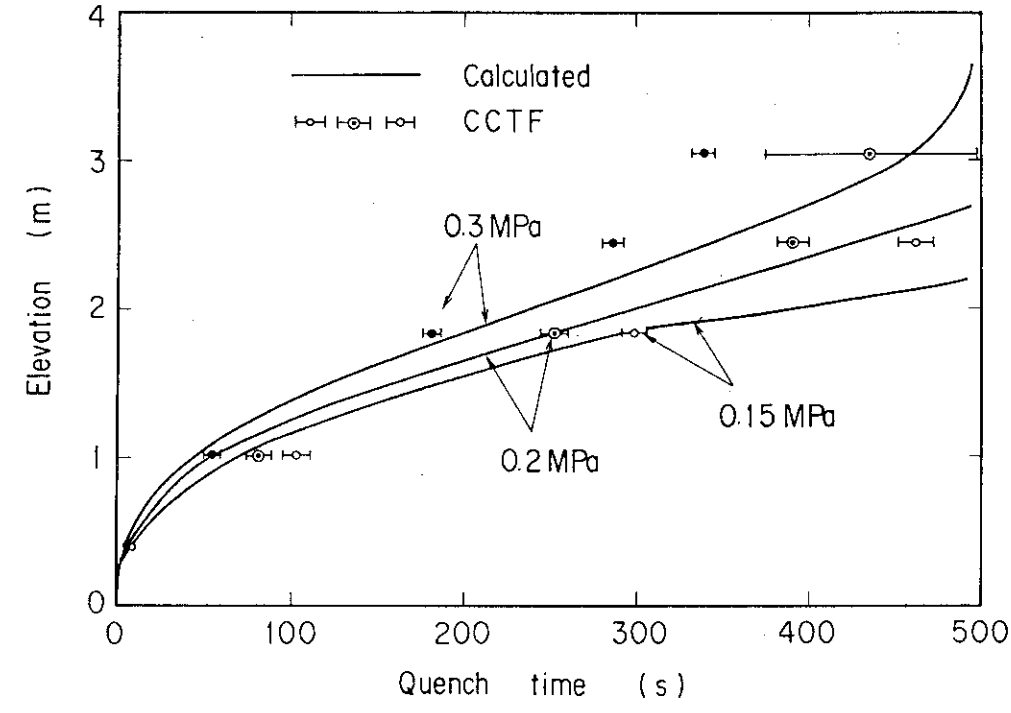

Fig. 4.17 Effect of system pressure on quench envelope

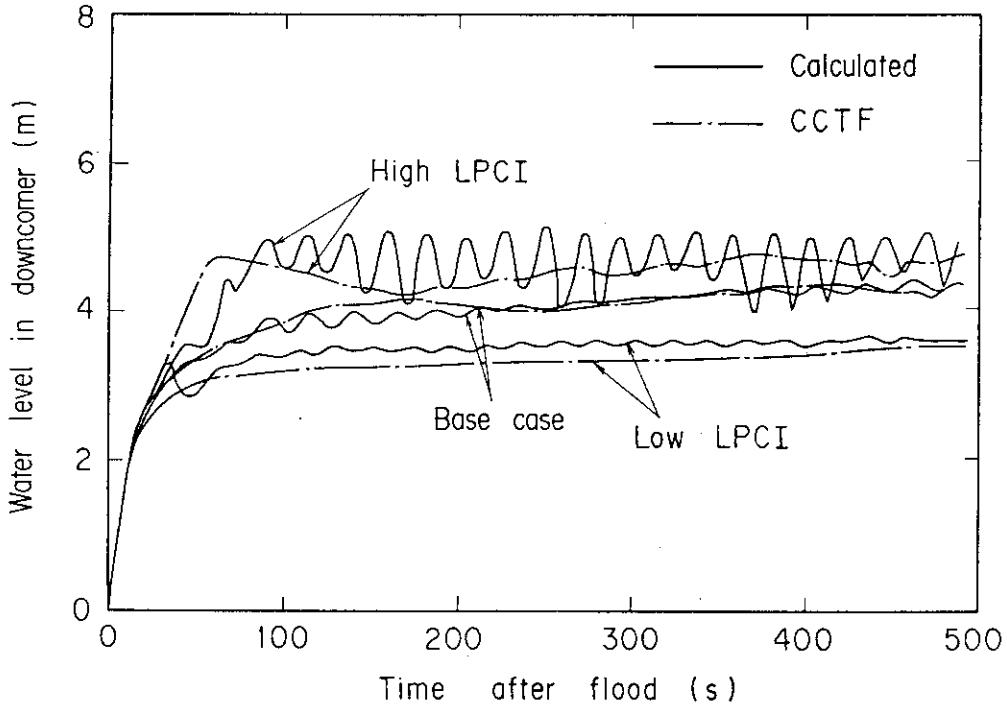

Fig. 4.18 Effect of ECC flow rate on water level in downcomer

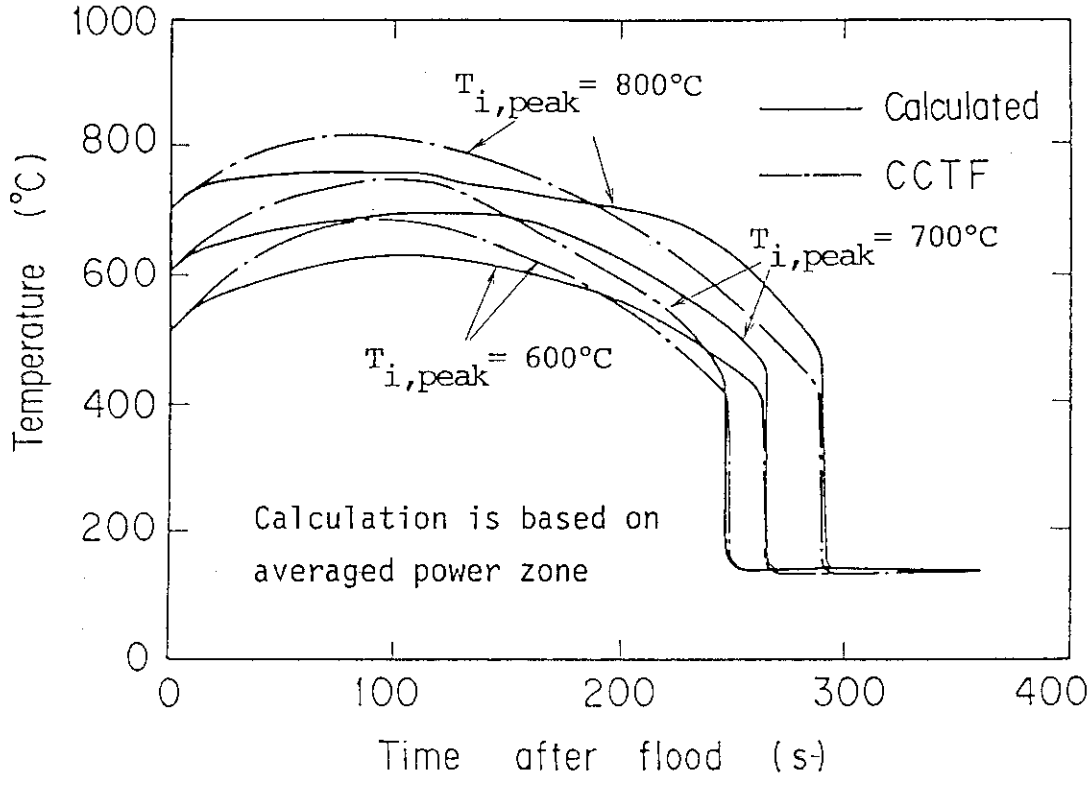

Fig. 4.19 Effect of initial peak clad temperature on clad temperature at midplane

5. Thermal Response Similarity between Simulated Heated Rods and Nuclear Fuel Rods[1]

5.1 Introduction

In most LOCA experiments, electrically heated rods are used for simulating fuel rods because of the ease of handling and cost benefit. As already shown in Fig. 1.5, the nuclear fuel rod typically has a gap, which is initially filled with He between the Zircaloy cladding and the UO_2 fuel pellets. In contrast the electrically heated rod mainly consists of a non-Zircaloy cladding, heater element and insulating material with no clad-to-fuel gap. Since the rod geometry and physical properties of the materials are considerably different between electrically heated and nuclear fuel rods, the typicality of non-nuclear rods is a concern for the safety evaluation of reactors in applying experimental results to a nuclear reactor.

There are, however, a limited number of works on the typicality of a simulated heated rod in a reflood transient condition. Piggott & Duffy[2] have shown that Zircaloy quenched faster than stainless steal in their re-wetting experiments on single tubes and rods. This trend has been confirmed by Dhir & Catton[3] with a 4-rod bundle using a radio-frequency skin heating facility. Nishida[4], using an electrically heated single rod with Zircaloy cladding, has shown that the quench front propagated faster with a smaller clad-to-fuel gap conductance.

Recently, Ihle et al.[5] have conducted 5x5-rod reflood experiments with two types of heated rods, i.e. Zircaloy cladding heated rod with a He filled gap and stainless steel cladding heated rod without a gap. They have found that the reflood transient is faster and cooling is better for fuel rod simulators. In an analytical field, Malang[6] has proposed an on-line process computer method to simulate fuel rod temperature response with an electrically heated rod based on simplified rod boundary conditions. Sudoh[7] has analyzed the typicality of electrically heated rods and the effect of fuel-to-clad gap conductance on clad temperature using the assumed boiling curve. In these works, however, not much attention has been paid to the coupling between the experiments and the analysis.

In this chapter presented is the quantitative evaluation of the

applicability of the thermal response of an electrically heated rod during LOCA experiments to that of a nuclear fuel rod in a typical reflood condition. A model of the temperature field in the rod is developed and incorporated into the reflood analysis code REFLA[8] to supply probable rod boundary conditions. First studied are the sensitivity of supposed time constant of heat release in the model, and the effects of both gap conductance and cladding material on the temperature response of the fuel rod. Data of existing experiments are then compared with the calculation to assess the present model and finaly to quantitatively evaluate the applicability of the electrically heated rod to the nuclear fuel rod.

5.2 Analytical model

(1) General description of reflood analysis code

In the present analysis, the thermo-hydraulics of fluid in the core subchannel is given by REFLA code[8]. The code incorporates non-equilibrium two-phase flow associated with several flow regimes in the core region as illustrated in Fig. 1.2. The assumed flow regimes are single-phase liquid and vapor flows, a saturated two-phase flow, a transition flow, a subcooled film boiling and a dispersed flow regions. The specific thermo-hydraulic relations are flow-regime dependent, which are mostly developed based on reflood experiments[9][10]. The finite differential equations and constitutive equations are numerically solved by the explicit scheme.

The REFLA code can be characterized by the use of a correlation for quench front velocity[11]; The velocity v_Q of quench front is assumed to be expressed as

$$v_Q^{-1} = KC_p\rho \qquad (5\text{-}1)$$

where C_p is the specific heat of the cladding material, ρ the density of the cladding material and the coefficient K is a function of clad wall temperature, system pressure, and local liquid subcooling. The correlation of quench front velocity in Eq. (5-1) can be applied to the case of very low temperature, in which the contact of water can be regarded as a statistical process. It is noted that the quench

velocity in Eq.(5-1) is inversely proportional to the heat capacity of the cladding material.

(2) Analytical model of fuel rod

The fuel model in the REFLA code was one-point approximation with flat radial temperature distribution in the rod. This assumption seems practically valid for the analysis of a simulated fuel rod, in which the thermal conductivity is relatively large. However, for the analysis of the thermal behavior of nuclear fuel rods, the radial temperature distribution in the rod should be considered because of the small thermal conductivity of the fuel and the existence of a fuel-to-clad gap. The following models for the temperature distribution and heat release from the quenched region are developed for that purpose to be incorporated into REFLA code.

Temperature field in rod

In the reflood phase, the azimuthal and axial heat conduction in the rod could be neglected, since the temperature transient is relatively slow except in the vicinity of the quench front. Hence the following radially one-dimensional heat conduction equation in the rod is considered:

$$C_p \rho \frac{\partial T}{\partial t} = q + \frac{1}{r} \cdot \frac{\partial}{\partial r} \left(\lambda r \frac{\partial T}{\partial r} \right) \quad , \tag{5-2}$$

where T indicates the temperature field, q the heat generation rate and λ the thermal conductivity.

In the present scheme, an explicit integration method with the finite element used in HETRAP by Malang[12] is adopted. From the finite differential form of Eq. (5-2), the temperature T^{n+1} of i-th node at a new time step n+1 is expressed with temperature at the old time step n as

$$\frac{T_i^{n+1} - T_i^n}{\Delta t} (C_p \rho V)_i = \frac{T_{i-1}^n - T_i^n}{R_{i,i-1}} + \frac{T_{i+1}^n - T_i^n}{R_{i,i+1}} + q_i^n V_i \quad , \tag{5-3}$$

where Δt is the time increment, $R_{i,i-1}$ the thermal resistance and V_i the volume of i-th node. The thermal resistance $R_{i,i-1}$ in Eq. (5-3) is generally expressed with a combination of conduction, contact and

radiation heat resistance as

$$\frac{1}{R_{i,i-1}} = \frac{1}{\frac{\ln(r_{i-1}/r_i)}{\lambda} + \frac{1}{h_{gap}\, r_s}} + \varepsilon E_i r_s \frac{T_i^4 - T_{i-1}^4}{T_i - T_{i-1}} \qquad (5\text{-}4)$$

where r_i is the radius of i-th node, h_{gap} the gap heat transfer coefficient, r_s the gap width of either contact or radiation heat transfer, ε the Stefan-Boltzmann constant and E_i the emissivity.

In the present code, the mean value $r_{i,i-1}$ in calculating volume V_i associated with i-th node in a rod is given by

$$r_{i,i-1} = \sqrt{(r_{i-1}^2 - r_i^2)/\{2\ln(r_{i-1}/r_i)\}} \quad , \qquad (5\text{-}5)$$

using two adjacent radii r_i and r_{i-1}. The volume Vi per unit length is expressed as

$$Vi = \pi (r_{i,i-1}^2 - r_{i+1,i}^2) \quad , \qquad (5\text{-}6)$$

This is so that the calculated temperature at any node will agree with the analytical solution regardless of the total noding number[12].

The gap conductance between the cladding and the fuel element is treated in the code as a sum of the contact heat transfer and the radiation heat transfer to the total thermal resistance. Only the contact heat transfer coefficient is an input. The radiation heat transfer is automatically calculated in the code.

The boundary condition at the rod surface (i=1) is expressed as

$$T_1^{n+1} = \frac{T_2^{n+1} - T_f}{hr_1 R_2} + T_f \quad , \qquad (5\text{-}7)$$

assuming the coolant temperature T_f is connected to the second node to avoid a too small calculating time step[12]. The heat transfer coefficient h at the cladding surface is given by thermo-hydraulic relations used in the REFLA code. Usually the maximum time increment for stable calculation of temperature field in the rod is smaller than that required for the thermo-hydraulic calculation of the core subchannel. Therefore the temperature field calculation independently

advances until the time step reaches that of thermo-hydraulic calculation.

Heat release from quenched region

For comparison with the previous REFLA model, a schematic of the present model for the heat release from the quenched region is illustrated in Fig. 5.1. In the previous model of one-point approximation for the fuel temperature, fraction A_{st}, which corresponds to the ratio of cladding area to rod area, is assumed to be instantaneously quenched due to quench propagation. The remaining fraction $(1-A_{st})$ is assumed to release the stored heat to the coolant with time constant.

In the present model, a similar but more detailed treatment is adopted as shown in Fig. 5.1. The heat release rate q_I per unit length due to the instantaneous quenching of the cladding is calculated using the radial temperature distribution as

$$q_I = (\overline{C_p\rho S})_c (T_{Q1} - T_{Q2}) \frac{\Delta z_Q}{\Delta t \Delta Z} \qquad (5\text{-}8)$$

where the clad heat capacity $C_p\rho S$ is averaged between the old and new time steps, T_{Q1} is the clad surface temperature just before the quenching, T_{Q2} the clad surface temperature just after the quenching, Δz_Q the advanced length of the quench front between time step Δt, and ΔZ the axial fluid cell increment in the core.

The gradual heat release rate $q_{Gj}(t)$ per unit length of the stored energy at j-th fluid cell is given as

$$q_{Gj}(t) = \Sigma\{(C_p\rho ST)^O_{ij} - (C_p\rho ST)^N_{ij}\} \frac{1}{\tau} \exp(-t_{Qj}/\tau) \quad , \qquad (5\text{-}9)$$

where the sum is taken over the nodes in the fuel element, superscripts O and N indicate the times just before and after the quench front passed the j-th fluid cell, respectively, t_{Qj} is the time after quench front passed the j-th fluid cell.

It should be noted that the release of the stored energy after the quenching is calculated independently on the temperature field calculation using the heat transfer coefficient and the fluid

temperature. This is to avoid a too detailed axial and radial heat conduction calculation resulting from fine noding near the quench front, which will unnecessarily increase the calculational time.

5.3 Analysis and application to experiments

In order to assess the present model, an anlaytical calculation was performed for both electrically heated and nuclear fuel rods. A parametric calculation was first performed to investigate the sensitivity of the geometrical and calculational parameters on core thermo-hydraulics. Data of existing LOCA reflood experiments were then compared with the calculation to quantitatively evaluate the applicability of electrically heated rod to the fuel rod.

In the calculation, the core was axially devided into 90 fluid cells for the thermo-hydraulic calculation in the flow channel. The rod was radially divided into 12 nodes for the temperature field calculation. It is noted that the present calculation is based on a fixed boundary condition at the core inlet (the feed-back of the system is excluded).

(1) Parametric effect

The core boundary and initial conditions shown in Table 5.1 are used in this parametric calculation. The conditions are mostly based on typical reflood conditions with slight simplification to facilitate the evaluation of tested parameters. The rod geometry used in the calculation is based on that of the nuclear fuel rod shown in Fig. 1.5(a).

The base input for the time constant in Eq. (5-9) is evaluated with Fourier number given by

$$F_0 = \lambda t / C_p \rho d_f^2 \quad , \tag{5-10}$$

to represent the characteristic time constant as

$$\tau = C_p \rho d_f^2 / \lambda \quad , \tag{5-11}$$

where the physical properties of the fuel element are used, and d_f is

the radius of the fuel element.

The h_{gap} is also an input in the present code. The typical value of h_{gap} in a reflood condition has not been well understood. Generally the gap heat transfer coefficient tends to be larger with the operation time after the refueling due to the supposed clad creep. A tentative value of 580 $W/m^2.K$, which is close to the reference value used in a PWR-LOCA licensing safety analysis, is used as a base input.

Effect of time constant of heat release

Figure 5.2 shows the effect of the time constant, which is required in Eq. (5-9), on the calculated temperature transients at 1.83 and 2.44 m elevations. Although the temperature tends to be slightly higher and quench time slightly longer for a larger time constant, its effect on the overall transient is very small as shown in Fig. 5.2. Especially the turnaround (maximum) temperature is only slightly affected by the time constant in the wide range of 5～50 s.

Figure 5.3 shows the effect of the time constant on the calculated average void fractions between 1.22 and 1.83 m, and between 1.83 m and 2.44 m elevations. With a larger time constant, the calculated void fraction tends to be slightly lower early in the transient, but it tends to be higher later in the transient as shown in Fig. 5.3. This is due to the reversed nature of the heat generation between instantaneous and gradual heat releases below the quench front as it relates to the time constant. The difference in void fraction, however, is very small for a wide range of time constants as shown in Fig. 5.3. All these results show that the present simple method of calculating the heat release from the quenched region using the time constant does not much affect the thermo-hydraulic characteristics. The method therefore has an advantage by reducing the computing time by avoiding too detailed axial heat conduction calculation.

Effect of gap conductance

Figure 5.4 shows the effect of h_{gap} on the calculated temperature transients at 1.83 and 2.44 m elevations. With larger h_{gap} (infinite in the case of no gap) the calculated temperature is higher and the quench time is longer. This shows that the effect of gap conductance heat transfer is significant for the core cooling behavior. In the

case of small h_{gap}, especially, the temperature rise tends to be retarded early in the transient at about 15 s when the steam generation rate increases. This shows that the heat release from the cladding occurs more rapidly with a smaller h_{gap}.

The temperature distribution in the fuel rod is shown in Fig. 5.5. Four casse of h_{gap} are compared at time 0, 80 and 160 s after reflood initiation. With smaller h_{gap}, the temperature difference across gap and fuel temperature are higher as expected. It is noted that the outer clad temperature is lower with smaller h_{gap}. This indicates that the smaller gap heat transfer causes better cooling of the clad, while retaining more stored energy in the fuel element. This, in other words, shows that only the clad tends to be cooled when the gap heat transfer is considerably small. It is also noted that the initial clad temperature was set 540°C in all cases. Consequently the initial stored energy is higher with smaller h_{gap} as shown in Fig. 5.5. Even so, Fig. 5.4 shows the strong effect of gap conductance heat transfer on the core cooling.

Effect of cladding material

The effect of cladding material on quench front movement is shown in Fig. 5.6. The quench front for Zircaloy cladding moves much faster than that for Inconel cladding, which is widely used in non-nuclear core LOCA experiments. This is primarily due to the smaller heat capacity of Zircaloy than Inconel because the quench front velocity shown in Eq. (5-1) is inversely proportional to the heat capacity in the present scheme. Although the heat capacity of Zircaloy is about one-half of Inconel, the calculated quench front velocity of Zircaloy shown in Fig. 5.6 is only about 30% faster than that of Inconel cladding. This discrepancy can be attributed to the less improved heat transfer above the quench front in the Zircaloy cladding case. The faster quench front movement produces a larger steam generation due to the release of the stored energy, which results in the higher void fraction and smaller heat transfer to retard the quench front movement. Thus the effect of cladding material has a feed-back nature between the quench front movement and heat transfer.

Figure 5.8 shows the effect of cladding material on the calculated clad temperature history. Although the quench time is faster for cladding material with smaller heat capacity, as discussed

above, the temperature transient near the turnaround is not affected by the cladding material. As a result, when compared with the time constant of heat release or the cladding material, the effect of gap conductance was found to be the dominant factor in the evaluation of the maximum clad temperature.

(2) Application to experiments

The calculation was then performed to assess the present model by comparing the calculation with existing experiments and finaly to quantitatively evaluate the applicability of electrically heated rod to the fuel rod in a typical reflood condition.

SEFLEX test

In the SEFLEX program[5], the effects of cladding material and clad-to-fuel gap conductance have recently been investigated in 5x5 rod bundle reflood experiments. Figure 5.8 shows the comparison of heated rods used in the experiments. As shown in Fig. 5.8, Type 1 rod has a stainless steel cladding with no gap, whereas Type 2 rod has a Zircaloy cladding with a He filled gap between cladding and Al_2O_3 insulating pellets.

The tests applied for the present calculation were performed with 0.2 MPa of the system pressure, 3.8 cm/s of the flooding rate, and the 2.44 kW/m of the initial peak liner power followed by 120% ANS decay heat for both types of rod bundles shown in Fig. 5.8. In the present calculation, the estimated time constant of 10 s is used for both types of rod bundles, and the gap heat transfer coefficient of 580 $W/m^2.K$ is used for Type 2 He gap.

The comparison of clad temperature responses between the calculation and experiment is shown in Fig. 5.9. Although the calculated clad temperature tends to be lower than the experiment (especially for Type 1), the overall tendency is reasonably predicted with the present model. The underestimated clad temperature might be due to the experimental procedure with an initially extremely high wall temperature of the flow housing, which is not modeled in the present scheme.

Figure 5.10 shows the comparison of measured and calculated quench front movement for both types of heated rods. Although the calculated quench front moves slightly later than the experiments for both cases, the overall tendency of the quench front movement is well

predicted. This shows that the present model is reasonable concerning the cladding material and also the fuel-to-clad gap conductance.

CCTF test

The CCTF described in 4.3 is an integral reflood experiment facility with 2,048 rods and active primary system components. With the full simulation of the primary system, the facility could supply a reasonable core inlet flow condition which can be expected in a typical reflood phase of PWRs. Furtheremore the large number of simulated rods in the core are supposed to eliminate the unwilling effect of surrounding test vessel wall. Figure 5.11 compares the heated rod used in CCTF, nuclear fuel rod, and two simulating heated rods having clad-to-pellet gap; one with Inconel and the other with Zircaloy claddings.

The calculation for rod geometries shown in Fig. 5.11 was performed to first assess the present model and finaly to quantitatively evaluate the applicability of thermal response of electrically heated rods to that of fuel rods. In the present calculation, the time-varying boundary conditions at the core inlet were only provided from the test evaluation[13]. The rod surface condition was supplied by the calculated heat transfer coefficient and not by the measured one to ensure the whole effect of the difference in rod geometries shown in Fig. 5.11.

The calculated and measured temperature histories at the midplane of the core are shown in Fig. 5.12. The calculation for CCTF case is in favorable agreement with the experiments, again indicating a reasonable modeling in the present analysis. It is noted that the temperature response near the turnaround in CCTF is better predicted by the code than that in SEFLEX shown in Fig. 5.9. In CCTF the initial temperature of the flow housing was about 120°C, which is much lower than SEFLEX (about 700°C). The effect of the flow housing is also much smaller in CCTF than SEFLEX, due to about 80 times larger size of the core. These could explain the difference of the prediction between SEFLEX and CCTF.

Due to smaller heat capacity, the calculated temperature of a nuclear fuel rod rises faster than a CCTF heated rod. It then decreases rapidly due to the existence of the gap between clad and fuel. As a result, the calculated temperature of a nuclear fuel rod

tends to be lower than the CCTF heated rods during most of the reflood transient. The obtained lowering of the peak clad temperature is about 80 K in the average powered rod. This shows that the test results of non-nuclear core LOCA experiments are conservative when applying them to nuclear reactors.

For the two cases of simulating heated rods with gap, the temperature transient in an early reflood transient is more similar to a nuclear fuel rod than a CCTF heated rod. Especially the temperature behavior of the heated rod with a gap and Zircaloy cladding is almost the same as that of a nuclear fuel rod. This implies that a better simulation could be made if a heated rod with a gap and the appropriate materials are chosen.

The present analysis is based on the modified REFLA code, which is best-estimate oriented. The code was assessed against the existing reflood experiments including a bundle experiment with Zircaloy cladding and the largest integral experiment with active and full primary system components. Using those data the conservatisms of the LOCA experiments were quantitatively evaluated.

5.4 Summary

(1) Analysis was performed to investigate the thermal response similarity between an electrically heated rod in LOCA experiments and a nuclear fuel rod in a PWR reflood condition. A model describing the radial temperature field in the rod was developed based on the scheme of HETRAP code by Malang and incorporated into a reflood analysis code, REFLA.

(2) The maximum clad temperature of the fuel rod was found to be much affected by the gap conductance heat transfer as a limiting heat resistance. Whereas it was little affected by the time constant of the heat release from the quenched region or the cladding material. In the application to SEFLEX and CCTF tests, good agreement with experiments were obtained, which shows the validity of the present model.

(3) It is expected that the nuclear fuel rod gives a lower clad temperature and a sooner quench time than the electrically heated rod in a typical reflood condition. This is mainly due to a

smaller clad-to-fuel gap heat transfer and a smaller heat capacity of the cladding material of nuclear fuel rods than electrically heated rods.

References

(1) Sugimoto, J., et al.: J. Nucl. Sci. Technol., 23 [4], 315~325 (1986).
(2) Piggott, B.D.G. and Duffey, R.B.: Nucl. Eng. Des., 41, 165～173 (1977).
(3) Dhir, V.K. and Catton, I.: EPRI-NP-1277, (1979).
(4) Nishida, M.: KfK 3786 B, (1984).
(5) Ihle, P., et al.: Presented at 1st Int. Workshop on Fundamental Aspects of Post-dryout Heat Transfer at Salt Lake City, (1984).
(6) Malang, S.: ORNL-TM-4712, (1975).
(7) Sudoh, T.: JAERI-M 9533, (1981).
(8) Murao, Y.: J. Nucl. Sci. Technol., 16[11], 803～817 (1979).
(9) Murao, Y., et al.: ibid., 19[8], 613～627 (1982).
(10) Murao, Y. and Sugimoto, J.: ibid, 18[4], 275～284 (1981).
(11) Murao, Y.: ibid., 15[12], 875～885 (1978).
(12) Malang, S.: ORNL-TM-4555, (1974).
(13) Murao, Y., et al.: JAERI-M 83-029, (1983).

Table 5.1 Core boundary and initial conditions for parametric calculation

Condition	Value
Pressure at core inlet	0.2 MPa
Initial peak linear power	2.0 kW/m
Axial power profile	17 step chopped cosine
Peaking factor	1.49
Power decay type	ANSx1.2 + Actinide*
Core flooding rate	3 cm/s
Inlet water temperature	373 K
Initial peak clad temperature	777.5 K

Note * ANS 5.1: Decay Energy Release Rates following Shutdown of Uranium-fueled Thermal Reactors, October (1971).

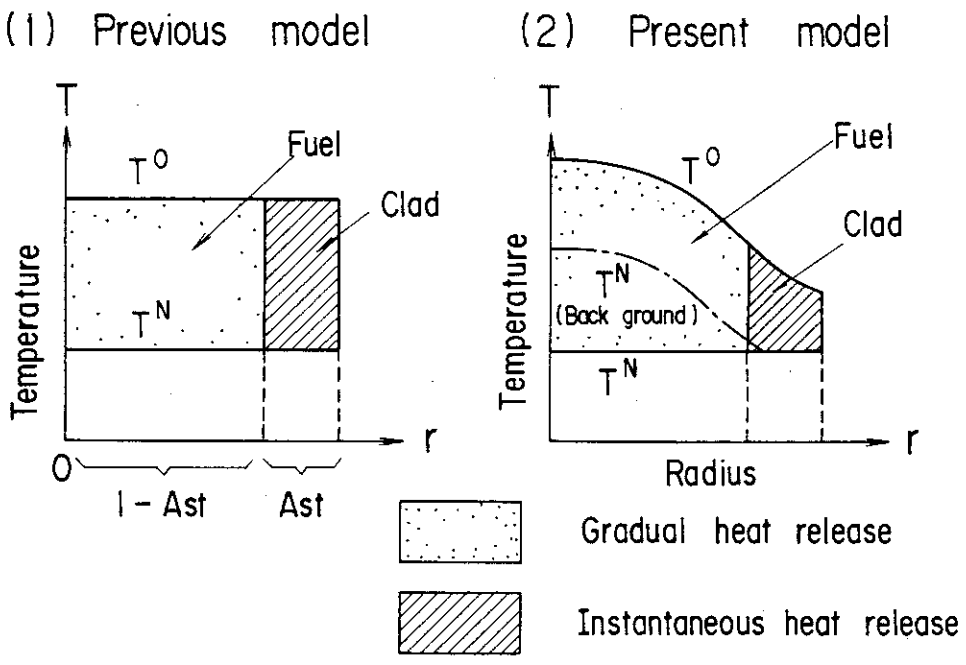

Fig. 5.1 Schematic of heat release from quenched region

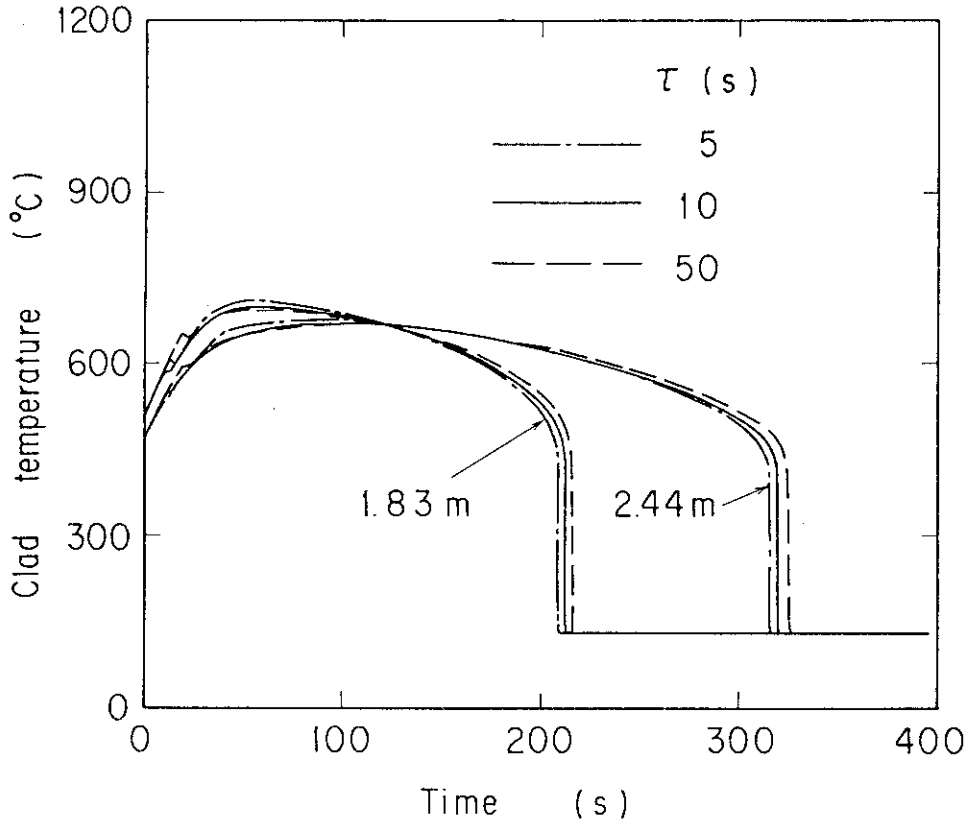

Fig. 5.2 Effect of time constant of heat release on calculated clad temperature history

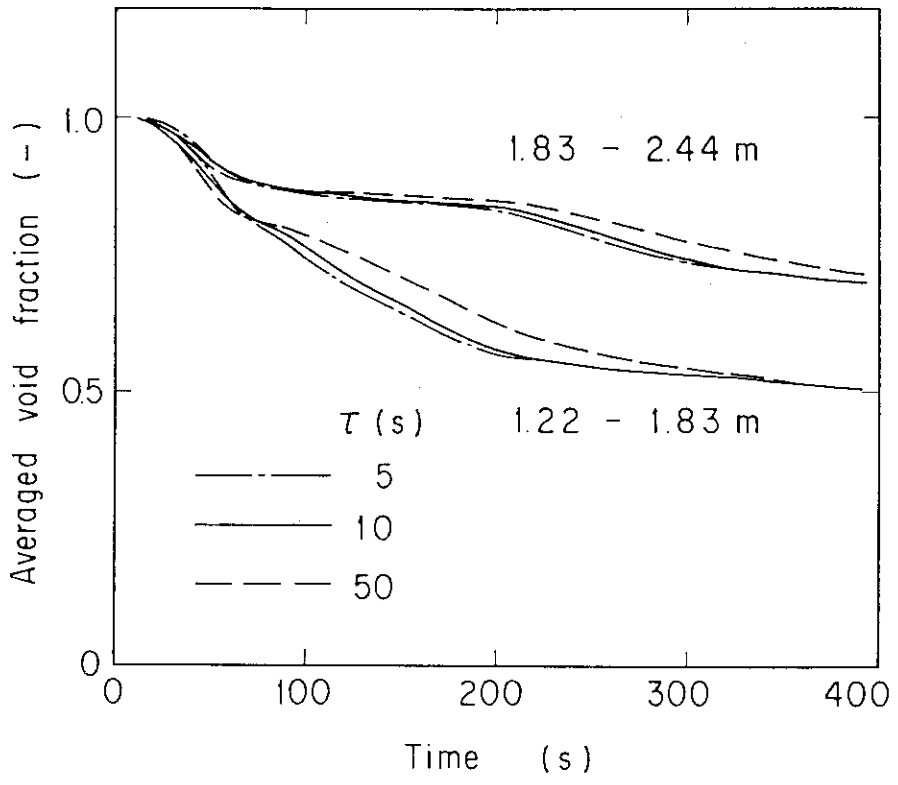

Fig. 5.3 Effect of time constant of heat release on calculated void fraction

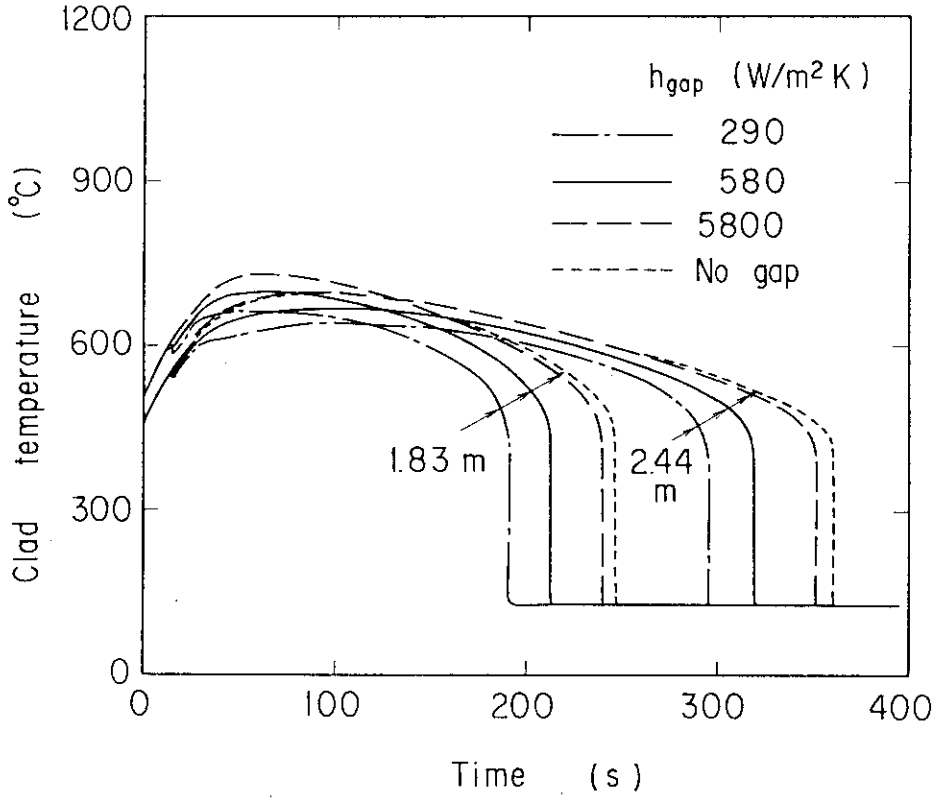

Fig. 5.4 Effect of gap conductance on calculated clad temperature history

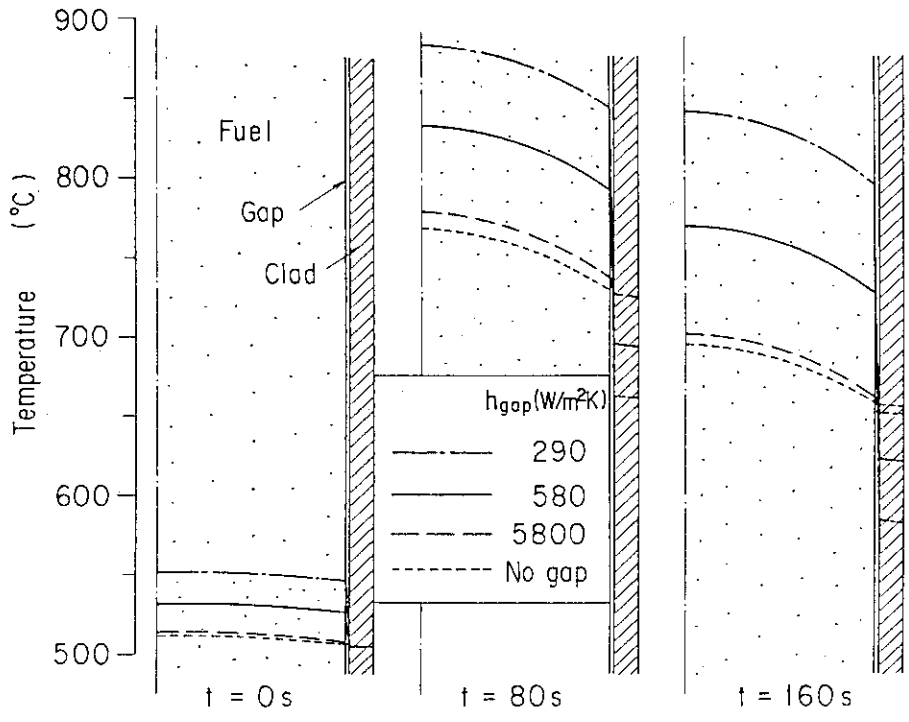

Fig. 5.5 Effect of gap conductance on calculated temperature field in rod

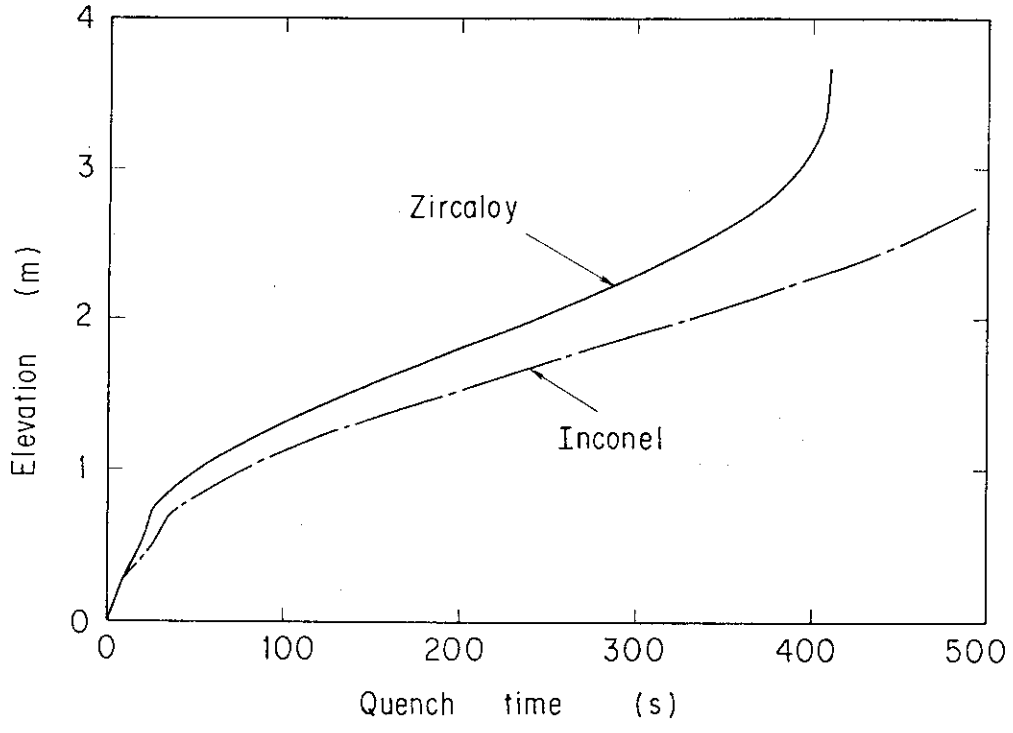

Fig. 5.6 Effect of cladding material on calculated quench front movement

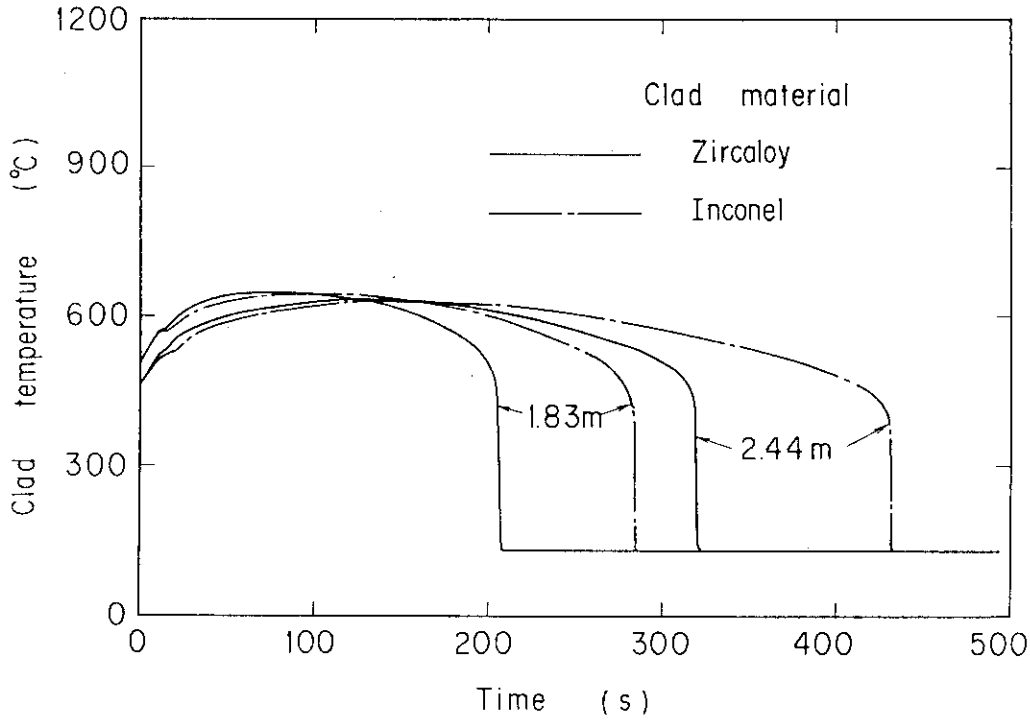

Fig. 5.7 Effect of cladding material on calculated clad temperature history

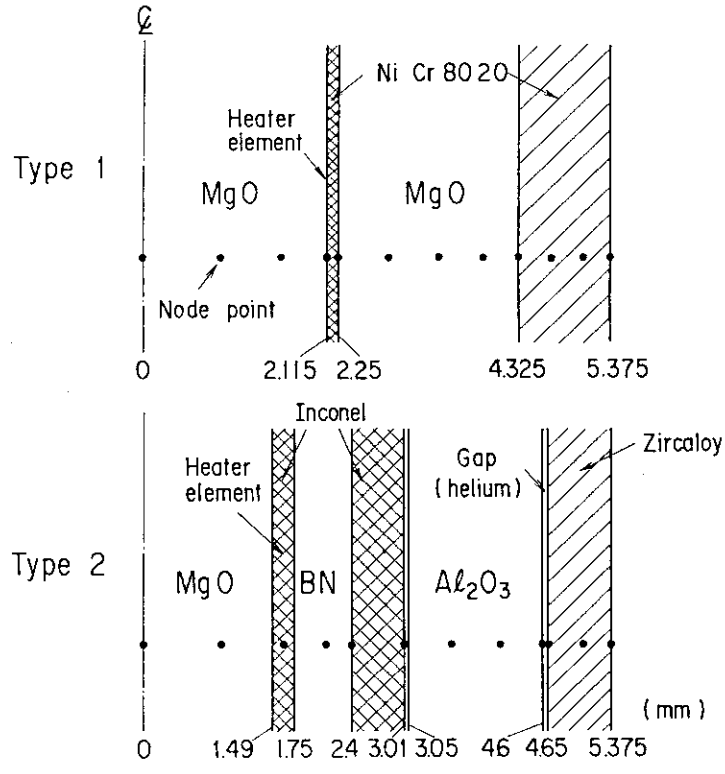

Fig. 5.8 Comparison of type 1 and 2 electrically heated rods used in SEFLEX test[5]

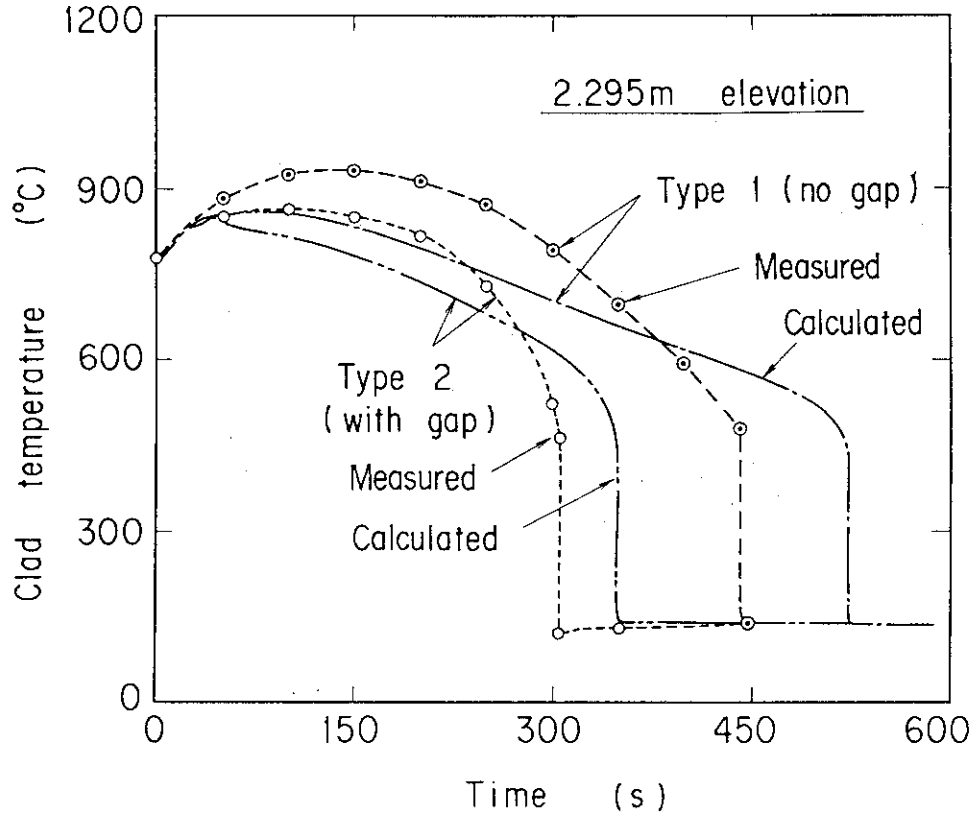

Fig. 5.9 Calculated and measured clad temperature responses in SEFLEX test[5]

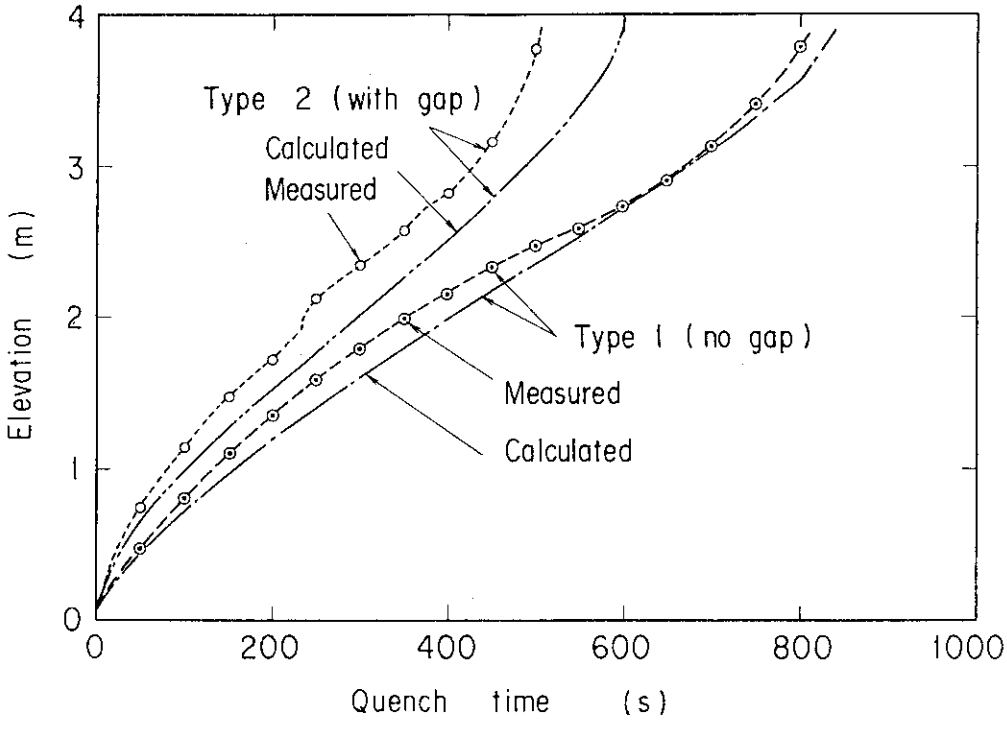

Fig. 5.10 Calculated and measured quench front movements in SEFLEX test[5]

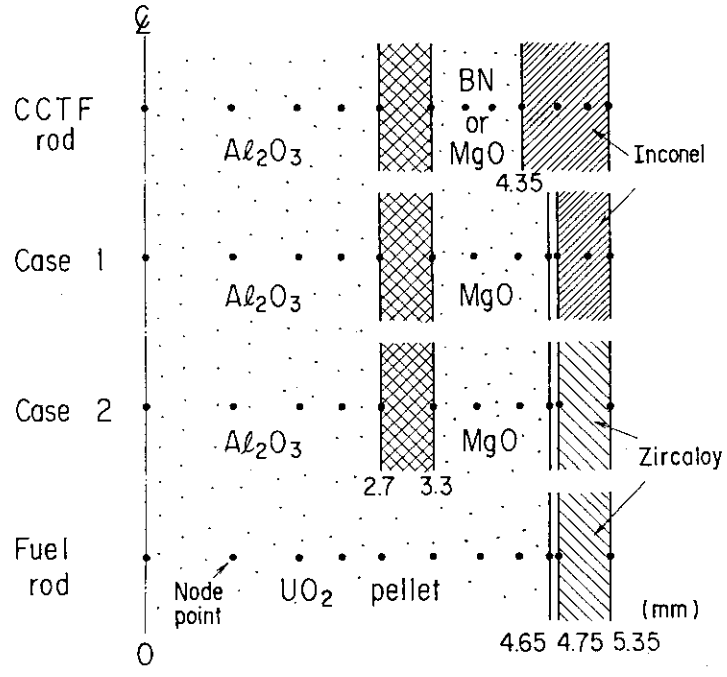

Fig. 5.11 Comparison of heated rod used in CCTF test, nuclear fuel rods, and two cases of simulated electrically heated rods

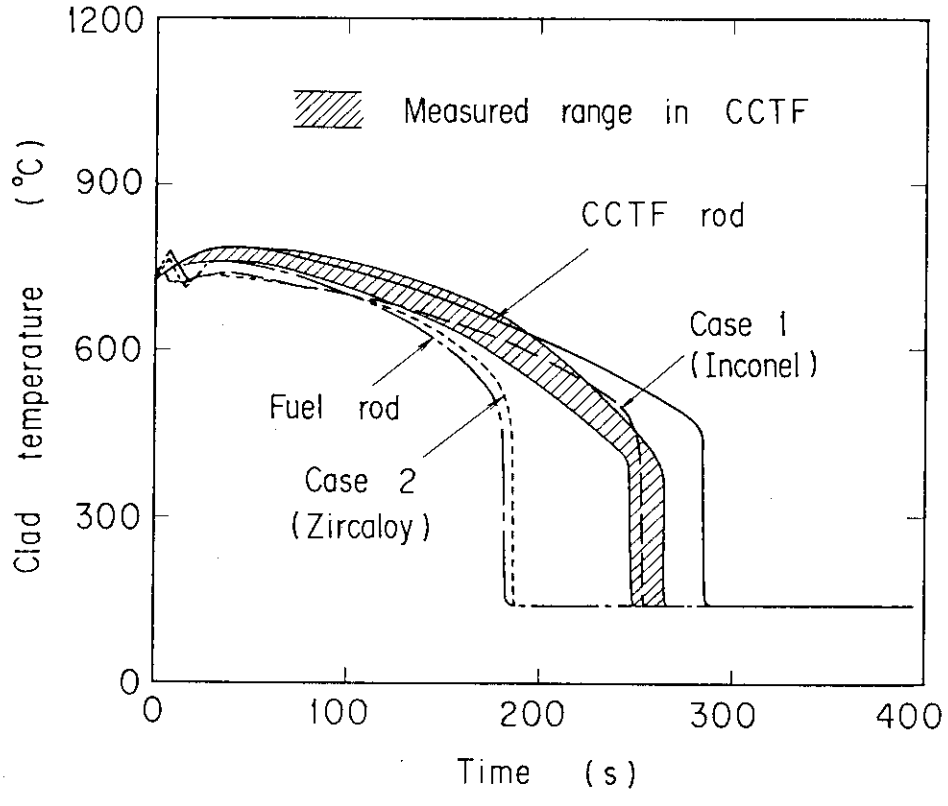

Fig. 5.12 Calculated and measured clad temperature responses at midplane in CCTF test[13]

6. Conclusions

The effectiveness of an emergency core cooling system (ECCS) in a postulated loss-of-coolant accident (LOCA) has long been a concern from the point of nuclear safery. The reflood phase is defined as the ultimate process to flood the heated core in the later part of LOCA transient. Since the peak cladding temperatures of the fuel rods are expected to be realized in the reflood phase, the precise description of reflood core cooling behavior has great importance in a safety evaluation.

In the early reflood phase, the injected ECC water cannot easily contact the fuel cladding due to a combinatien of low water level in the core and with high core temperature. At this time core cooling is accomplished through flowing steam with entrained water droplets. Entrained water droplets carried into the steam generators, however, are evaporated by the higher temperature of secondary side water. This increases the flow resistance at the primary coolant pumps which reduces the net core inlet flow. The core inlet flow, however, is essential to core cooling. The thermo-hydraulic behavior of the reflood process is thus complex and contains an element of negative feedback.

In this paper, the thermo-hydraulic behavior during the reflood phase of a PWR-LOCA has been studied experimentary and analytically to better predict the reflood transient in a nuclear safety analysis. Specifically the following four themes have been described in detail:

(i) Characteristics of saturated film boiling heat transfer in core region

(ii) Effect of grid spacers on core thermo-hydraulics

(iii) Characteristics of the thermo-hydraulic behavior in the primary system

(iv) Thermal response similarity between a nuclear fuel rod and a simulated heated rod

An analytical model for each item has been developed based on the physical understanding of the reflood phenomena or simple model experiments. The developed model has then been compared with existing bundle or integral experiments to evaluate the model

The following summarizes the results obtained from this study:

(1) In chapter 1, the LOCA sequence and reflood behavior have been described and illustrated. Previous work concerning the reflood thermo-hydraulic behavior has been reviewed. The four specific items described above have been selected to be investigated. The objective of this study has been clarified and the procedure to achieve this goal has been identified.

(2) In chapter 2, a new heat transfer correlation has been developed for the saturated film boilig region based on a 4 x 4-rod experiment. The correlation is expressed as the sum of the Bromley-type film boiling heat transfer and the radiative heat transfer, with consideration for the effect of void fraction and the distance from the quench point. The correlation gives good agreement with the data from both small scale JAERI and FLECHT experiments within an error band of about 20 %. The correlation also provides good agreement with data from the large-scale reflood experiments conducted at JAERI. The possible effects of grid spacers on core thermo-hydraulics has been described.

(3) In chapter 3, an analytical model has been developed, based on the flow observations and model experiments, to characterize the effect of grid spacers on core thermo-hydraulics. The breakup of water droplets by grid spacers in dispersed flow has been formulated in simple form. This provides increased vapor-to-liquid heat transfer. Increased water accumulation above the grid spacer in the inverted slug flow, not addressed by previous work, has been modeled. The two-phase flow behavior near the grid spacer, especially enhanced heat transfer downstream of grid spacers, was predicted well with the proposed model. Further work, however, is required for more mechanistic modeling of the flow near the grid spacers and to correct the overestimated heat transfer coefficient for 17 x 17 rod bundle geometry (compared to 15 x 15 rod bundle geometry).

(4) Chapter 4 presents a system analysis code developed by coupling a one-dimensional core model (REFLA) and a multi-loop primary system component model. The system components modeled are upper plenum, downcomer, ECC injection port and broken cold leg nozzle. The coupling of the core and the multi-loop system models is accomplished by the use of the equivalent flow resistance in a single loop with saturated steam. The code agrees fairly well

with thermo-hydraulic system behavior obtained in the large-scale integral reflood experiment with active primary system components. Several shortcomings of the code, which require further improvement, were identified. For application to a PWR, the need for model assessment of the cladding-to-fuel gap conductance was suggested.

(5) In chapter 5, an analytical model has been developed to investigate the thermal response similarity between nuclear fuel rods and electrically heated rods used in experiments. A model describing the radial temperature field in the rod was developed based on the scheme of Malang's HETRAP code and incorporated into the reflood analysis code REFLA. The model has been verified with the existing experiments, and it was found that the nuclear fuel rod will give a lower cladding temperature and an earlier quench time than the electrically heated rod in a typical reflood condition.

It was found that the analytical models described in this paper are satisfactory for most typical reflood conditions. It was also determined some defects remain which require further correction or applicational limits. It is concluded that the present analytical models have adequate predictability to be useful for nuclear safety analysis.

Acknowledgements

The author would like to express his sincere gratitude to Professor I. Michiyoshi, Professor H. Nishihara and Assistant Professor A. Serizawa of Kyoto University for hearty suggestions and encouragement.

He is also much grateful to Professor S. Takeno of Kyoto Technical University for continuons encouragement.

He is deeply indebted to Dr. Y. Murao of Japan Atomic Energy Research Institute (JAERI) for his guidance and stimulating discussions throughout the course of the present study.

He would like to express his appreciation to Dr. K. Hirano of JAERI for his guidance and encouragement.

He is also indebted to his colleagues at JAERI, Dr. H. Adachi, Mr. T. Iguchi, Mr. T. Sudoh, Mr. Y. Niitsuma, Dr. Y. Sudo, Dr. H. Akimoto and Mr. T. Okubo for their experimental and analytical supports.

Literature

The contents of the present study have been published in part in the following:

(1) Murao, Y. and Sugimoto, J.: Correlation of heat transfer coefficient for saturated film boiling during reflood phase prior to quenching, J. Nucl. Sci. Technol., 8[4], 275-284 (1981).

(2) Sugimoto, J., et al.: Effect of grid spacers on reflood heat transfer in PWR-LOCA, J. Nucl. Sci. Technol., 21[2], 103-114 (1984).

(3) Sugimoto, J., et al.: Heat transfer enhancement and water accumulation near grid spacers during reflood, 3rd Int. Conference on Reactor Thermal Hydraulics, Newport, Oct. (1985).

(4) Sugimoto, J., et al.: Investigation of reflood models by coupling REFLA-1D and multi-loop system models, JAERI-M 83-147, (1983).

(5) Sugimoto, J., et al.: Analytical study of thermal response similarity between simulated fuel rods and nuclear fuel rods during reflood phase of a PWR-LOCA, J. Nuc. Sci. Technol., 23[4], 315 - 325 (1986).

The following open reports by the author et al. have been referred in the present study:

(1) Sugimoto, J.: Study on thermocouple attachment method in reflood experiment, JAERI-M 6985, (in Japanese), (1977).

(2) Sugimoto, J., et al.: Data report on Series 5 reflood experiment, JAERI-M 7450, (in Japanese), (1978).

(3) Sugimoto, J., et al.: Data report on reflood experiment VIII (Series 6, heat transfer data), JAERI-M 8169, (in Japanese), (1979).

(4) Sugimoto, J.: TRAC-PD2 posttest analysis of CCTF Test C1-16 (RUN025), LA-8471-MS, NUREG/CR-1991, (1981).

(5) Sugimoto, J., et al.: Preliminary analysis of the effect of the grid spacers on the reflood heat transfer, JAERI-M 9992, (1982).

(6) Sugimoto, J.: Assessment of TRAC-PD2 reflood core thermo-hydraulic model by CCTF Test C1-16, JAERI-M 82-116, (1982).

(7) Sugimoto, J., et al.: Experimental study of effect of initial clad temperature on reflood phenomena during PWR-LOCA, J. Nucl. Sci. Technol., 20[8], 656-67 (1983).

(8) Sugimoto, J., et al.: Evaluation report on CCTF Core-I reflood tests C1-5 (Run 14), C1-7 (Run 16) and C1-14 (Run 23) - Effects of initial clad temperature -, JAERI-M 83-026, (1983).

(9) Sugimoto, J. et al.: Evaluation report on CCTF Core-II reflood tests C2-AC1 (Run 51) and C2-4 (Run 62) - Effect of initial clad temperature -, JAERI-M 84-026, (1984).

(10) Sugimoto, J., et al.: Report on reflood experiment of grid spacer effect, JAERI-M 84-131, (1984).

Appendix Details of system component model[1][2]

(1) Upper plenum

The schematic of the upper plenum is shown in Fig. A.1. The mass balance relation is written as,

$$W^{o}_{gc} + W^{o}_{\ell c} = \dot{M}_{U} + W^{I}_{gL} + W^{I}_{\ell L} + W_{FB} \quad , \tag{A-1}$$

where the core outlet vapor and liquid mass flow rates W^{o}_{gc} and $W^{o}_{\ell c}$, respectivley are calculated with the core model described in 4.1. It is assumed that the two-phase mixture in the upper plenum is thermally equilibrium. The loop mass flow rates W_{gL} and $W_{\ell L}$ are expressed with the total loop mass flow rate W_{L} in Eq. (4-3).

$$W^{I}_{gL} + W^{I}_{\ell L} = W_{L} \quad . \tag{A-2}$$

The water fall back mass flow rate W_{FB} in Eq. (4-16) is calculated with the correlation developed by Bankoff et al.[3] which is expressed as

$$W_{FB} = (2.0 - H_{g}^{\frac{1}{2}})^{2} \quad , \tag{A-3}$$

where

$$H_{g} = \frac{W^{o}_{gc}}{(g\,\rho_{g})\cdot A_{h}} \left[\rho_{g}/\{g\,w(\rho_{\ell} - \rho_{g})\}\right]^{\frac{1}{2}}$$

$$w = D_{h}^{1-\beta} \left[\sigma/\{g(\rho_{\ell} - \rho_{g})\}\right]^{\frac{\beta}{2}}$$

$$\beta = \tanh\left(\frac{2\pi}{d_{h}}\frac{A_{c}}{A_{h}}\right)$$

Here A_{h} denotes the total flow area of the holes at the upper tie plate, D_{h} the dimeter of the hole, d_{h} the thickness of the hole and A_{c} the core flow area.

The liquid carry-over $W^{I}_{\ell L}$ from the upper plenum to the hot legs is calculated with the upper plenum model developed by Iguchi et al.[4] The carry-over mass flow rate consists of two terms. One is the contribution of the core outlet liquid, and the other expresses the re-entrainment from the water pool in the upper plenum.

The correlation is written as follows:

$$W_{\ell L}^{I} = W_1 + W_2 \quad , \tag{A-4}$$

where

$$W_1 = \eta_U \cdot (1 - a_1) \cdot W_{\ell C}^{o} \quad ,$$

$$a_1 = \frac{M_U}{h_1 \cdot \rho_\ell \cdot A_U} \quad ,$$

and

$$W_2 = \begin{cases} W_{\ell C}^{o} - W_{FB} & (\Delta P_U > \Delta P_{max}) \\ \eta_U \cdot \dfrac{\Delta P_U}{\Delta P_{max}} \quad \dfrac{\rho_\ell \cdot A_U}{300} & (\Delta P_U < 0.9\ \Delta P_{max}) \\ \text{Interpolation} & (0.9\ \Delta P_{max} \leq \Delta P_U \leq \Delta P_{max}) \end{cases}$$

where η_U is the upper plenum de-entrainment coefficient and h_1 the critical water level for which W_1 is effective. The maximum differential pressure in the upper plenum ΔP_{max} is defined as,

$$\Delta P_{max} = L_{U\ max}\ \rho_\ell (1 - \alpha) \quad , \tag{A-5}$$

where L_{Umax} is the maximum water level in upper plenum and the void fraction α in the upper plenum is expressed by the correlation developed by Wilson et al.[5]:

$$\alpha = \max\ (\alpha_1, \alpha_2) \quad , \tag{A-6}$$

where

$$\alpha_1 = 0.851\ X^{0.4382} / \left(\frac{\rho_\ell}{\rho_g}\right)^{0.1798} \left(D_U / \sqrt{\sigma / g(\rho_\ell - \rho_g)}\right)^{0.1067} \quad ,$$

$$\alpha_2 = 0.488\ X^{0.6403} / \left(\frac{\rho_\ell}{\rho_g}\right)^{0.1151} \left(D_U / \sqrt{\sigma / g(\rho_\ell - \rho_g)}\right)^{0.0683} \quad ,$$

$$X = V_{go} / \sqrt{g\ \sqrt{\sigma / g(\rho_\ell - \rho_g)}}$$

$$V_{go} = W_{gc}^{o} / (A_U\ \rho_\ell) \quad .$$

Here D_U denotes the hydraulic diameter of the upper plenum.

The water accumulation rate $\dot{M}_U$ in the upper plenum can then be

written using Eqs. (A-1) and (A-2) as

$$\dot{M}_U = W^o_{gc} + W^o_{\ell C} - W_L - W_{FB} \quad . \tag{A-7}$$

The accumulated water at the new time step M_U^{n+1} is calculated using Eq. (A-7) i.e.,

$$M_U^{n+1} = M_u^{\,n} + \Delta t \cdot \dot{M}_U \quad . \tag{A-8}$$

The mixture water level h' and the differential pressure in the upper plenum ΔP_u are calculated using the updated mass M^{n+1};

$$h' = \frac{M_U^{\,n+1}}{A_U \cdot \rho_\ell \cdot (1 - \alpha)} \quad , \tag{A-9}$$

$$\Delta P_U = h' \cdot \rho_\ell \cdot (1 - \alpha) \quad . \tag{A-10}$$

It is noted that the differential pressure ΔP_U used in the calculation of W_2 in Eq. (A-4) is evaluated at the previous time step n in the code.

(2) Steam generator

An almost complete superheat of the fluid without water droplets at the outlet of the steam generator has been observed in CCTF test[6]. This is due to the heat transfered from the secondary side to the primary side of the steam generator. In the present code, the fluid in the primary side is assumed to be all evaporated through the steam generator as the zeroth-order approximation. The steam temperature at the outlet of the steam generator is set equal to the average temperature of the fluid in the secondary side.

This allows an easy treatment of the momentum and energy balance calculation of the primary loop. The fine water droplets, however, may still be present in the superheated steam flow as observed in the FLECHT-SET experiment[7]. This effect on the system responses is to be carefully investigated. However, the water droplet dispersed flow situation downstream the steam generator can also be considered in a similar manner described in the following sections.

(3) Pump

The primary loop coolant pump acts as a main flow resistance

during reflood phase. This steam binding effect is enhanced by the complete evaporation of the water droplets through the steam generators. In the present code, the pressure drops across the pump ΔP_{Pi} and the loop ΔP_{Li} are assumed to be expressed by the K-factors of the pump and the loop, respectively:

$$\Delta P_{Pi} = \frac{K_{pi}}{2\rho_{gi}} \left(\frac{W_{gLi}}{A_{Li}} \right)^2 \tag{A-11}$$

$$\Delta P_{Li} = \frac{K_{Li}}{2\rho_{gi}} \left(\frac{W_{gLi}}{A_{Li}} \right)^2 \tag{A-12}$$

where suffix i denotes the i-th loop, K_{pi} and K_{Li} are the K-factor of the i-th pump, and loop, respectively, W_{gLi} the steam mass flow rate through the loop. The main contribution to K_{Li} is due to the pump flow resistance K_{pi}.

(4) ECC injection port

The schematic of the ECC injection port at the cold leg is shown in Fig. A.2. The flow rate and the temperature downstream the ECC injection port are calculated based on the following assumptions:

1) The superheated steam from the steam generator is completely mixed with injected ECC water to form a thermally equilibrium condition.
2) No reverse flow occurs from the ECC injection port to the steam generator.

$$W^{I}_{gLi} + W_{ECCi} = W^{o}_{gLi} + W^{o}_{\ell Li}$$

$$C_{p\ell i}(\bar{T}_i - T_{sat})(W^{o}_{gLi} + W^{o}_{\ell Li}) \tag{A-13}$$

$$= W^{o}_{gLi}\{H_{fg} + C_{pgi}(T^{o}_{gLi} - T_{sat})\} + W^{o}_{\ell Li}\, C_{p\ell i}(T^{o}_{\ell Li} - T_{sat}) \tag{A-14}$$

$$= W^{I}_{gLi}\{H_{fg} + C_{pgi}(T^{I}_{gLi} - T_{sat})\} + W_{ECCi}\, C_{p\ell i}(T_{ECCi} - T_{sat})$$

The mixture temperature $\bar{T}_i$ defined above can easily be derived using Eqs. (A-13) and (A-14):

$$\bar{T}_i = \frac{W^I_{gLi}\{H_{fg}+C_{p\ell i}\,T_{sat}+C_{pgi}(T^I_{gLi}-T_{sat})\}+W_{ECCi}\,C_{p\ell i}\,T_{ECCi}}{C_{p\ell i}(W^I_{gLi}+W_{ECCi})} \qquad \text{(A-15)}$$

(a) If $\bar{T}_i$ is less than T_{sat} i.e. the mixture is subcooled,

$$\begin{aligned} W^o_{gLi} &= 0 \\ W^o_{\ell Li} &= W^I_{gLi} + W_{ECCi} \\ T^o_{gLi} &= T_{sat} \\ T^o_{\ell Li} &= \bar{T}_i \end{aligned} \qquad \text{(A-16)}$$

(b) If $\bar{T}_i$ is greater than T_{sat}, evaporation of the mixture is considered. The energy flux X of the mixture evaluated at the saturation temperature is expressed as,

$$X = W^I_{gLi}\,C_{pgi}(T^I_{gLi}-T_{sat}) - W_{ECCi}\,\{H_{fg}+C_{p\ell}(T_{sat}-T_{ECCi})\}$$

(i) If, further, X is greater than zero, the liquid is all evaporated to generate superheated steam flow:

$$\begin{aligned} W^o_{gLi} &= W^I_{gLi} + W_{ECCi} \\ W^o_{\ell Li} &= 0 \\ T^o_{gLi} &= T_{sat} + \frac{X}{C_{pg}(W^I_{gLi}+W_{ECCi})} \\ T^o_{\ell Li} &= T_{sat} \end{aligned} \qquad \text{(A-17)}$$

(ii) If X is less than zero, the mixture is a saturated two-phase flow i.e.,

$$\begin{aligned} W^o_{gLi} &= W^I_{gLi} + W_c \\ W_{\ell Li} &= W_{ECCi} - W_c \\ T^o_{gLi} &= T^o_{\ell Li} = T_{sat} \end{aligned} \qquad \text{(A-18)}$$

where

$$W_c = \frac{W^I_{gLi}\, C_{pgi}(T^I_{gLi} - T_{sat}) + W_{ECCi}\, C_{p\ell i}(T_{ECCi} - T_{sat})}{H_{fg}} \qquad \text{(A-19)}$$

(5) Downcomer annulus

The schematic of the downcomer annulus is shown in Fig. A-3. The two-phase mixture from the the intact cold legs is discharged into the upper part of the annular downcomer region. The horizontal flow path from the intact cold leg to the broken cold leg is fairly long (~ 6m) and expanded in the upper downcomer annulus region in a reactor vessel. It is therefore expected that the water in the upper part of the downcomer is partly entrained to the broken cold leg by the flowing two-phase mixture even when the water level in the downcomer is below the cold leg nozzle. This bypass phenomena observed in CCTF tests[6], is considered in the code using the downcomer carry-over coefficient η_D:

$$\begin{aligned} W^o_{gA} &= W^I_{gA} + W_{gD} \\ W^o_{\ell A} &= \eta_D\, W^I_{\ell A} + W_{\ell D} \\ W_o &= (1 - \eta_D) W^I_{\ell A} \end{aligned} \qquad \text{(A-20)}$$

where

$$W^I_{gA} = \sum_{i=1}^{N} W_{gLi}$$

$$W^I_{\ell A} = \sum_{i=1}^{N} W_{\ell Li}$$

and Wo is net liquid mass flow rate into down comer.

The variables W_{gD} and $W_{\ell D}$ is the vapor and liquid mass flow rates from the downcomer to the broken cold leg, respectively. The downcomer carry-over coefficient η_D is given as,

$$\eta_D = \begin{cases} 0 & (x < x_0) \\ \eta_{DO} & (x \geq x_0) \end{cases}, \qquad \text{(A-21)}$$

where x is the liquid level in the downcomer, x_0 the critical liquid

level above which the liquid carry-over occurs. The temperature of the two-phase flow to the broken cold leg is calcualted assuming the same complete homogeneous mixing as the ECC injection port.

(6) Downcomer

In the present code, the downcomer component includes the downcomer and the lower plenum portion as illustrated in Fig. A.4. The overflowing liquid mass flow rate $W_{\ell D}$ from the downcomer to the broken cold leg nozzle is evaluated by,

$$W_{\ell D} = \begin{cases} 0 & (x < x_{max}) \\ W_o - W_c^I + W_{ECCLP} + W_{FB} & (x \geq x_{max}) \end{cases} \qquad \text{(A-22)}$$

where x_{max} is the maximum length of the downcomer i.e. the distance from the downcomer bottom to the lower edge of the cold leg nozzle.

The steam mass flow rate W_{gD} is tentatively set equal to zero, assuming no voiding of the water in the downcomer as the zeroth-order approximation.

The temperature of the downcomer liquid $T_{\ell DC}$ is calculated by the mass and energy balances in the downcomer:

$$\frac{d}{dt} M_D = W_o - W^* - W_{\ell D} \quad , \qquad \text{(A-23)}$$

$$\frac{d}{dt} \{M_D C_{p\ell}(T_{\ell D} - T_{sat})\} = W_o C_{p\ell}(T_{\ell A} - T_{sat}) - W_{\ell D} C_{p\ell}(T_{\ell D} - T_{sat}) - W^* C_{p\ell}(T^* - T_{sat}) \qquad \text{(A-24)}$$

where $W^* = W_C^I - W_{ECCLP} - W_{FB}$,

$$T^* = \begin{cases} T_{\ell D} & (W^* \geq 0) \\ T_{\ell LP} & (W^* < 0) \end{cases}$$

Using the finite differential scheme, the downcomer liquid temperature at the next time step $T_{\ell D}^{n+1}$ is expressed as

$$T_{\ell D}^{n+1} = L \cdot T_{\ell D}^{n} + M \cdot T_{\ell A}^{n} + N \cdot T_{\ell Lp}^{n} \quad . \qquad \text{(A-25)}$$

The coefficients L, M and N are given as follows:

$$L = \begin{cases} \dfrac{2M_D - \Delta t\, W_o}{2M_D + \Delta t\, W_o} & (W^* \geq 0) \\ \dfrac{2M_D - \Delta t(W_o - W^*)}{2M_D + \Delta t(W_o - W^*)} & (W^* < 0) \end{cases}$$

$$M = \begin{cases} \dfrac{2\Delta t \cdot W_o}{2M_D + \Delta t\, W_o} & (W^* \geq 0) \\ \dfrac{2\Delta t\, W_o}{2M_D + \Delta t(W_o - W^*)} & (W^* < 0) \end{cases} \qquad \text{(A-26)}$$

$$N = \begin{cases} 0 & (W^* \geq 0) \\ \dfrac{-2\Delta t\, W^*}{2M_D + \Delta t(W_o - W^*)} & (W^* < 0) \end{cases}$$

The lower plenum is assumed to be full of liquid during the reflood phase. The energy balance in the lower plenum is then written as,

$$M_{LP}\, C_{p\ell}\, \frac{d}{dt}\,(T_{\ell LP} - T_{sat})$$

$$= C_{p\ell}\, W^*(T_1^* - T_{sat}) + C_{p\ell}\, W_{FB}(T_{\ell U} - T_{sat})$$

$$+ C_{p\ell}\, W_{ECCLP}(T_{ECCLP} - T_{sat}) - C_{p\ell}\, W_C^I(T_2^* - T_{sat}) \qquad \text{(A-27)}$$

where T_1^* and T_2^* are the liquid temperature at the upstream i.e.,

$$T_1^* = \begin{cases} T_{\ell D} & (W^* \geq 0) \\ T_{\ell LP} & (W^* < 0) \end{cases}$$

$$T_2^* = \begin{cases} T_{\ell LP} & (W_c^I \geq 0) \\ T_{\ell c} & (W_c^I < 0) \end{cases} \qquad \text{(A-28)}$$

The liquid temperature $T_{\ell Lp}$ in Eq. (A-27) is calculated in a similar manner as in Eq. (A-24) by using the finite differential scheme.

(7) Broken cold leg nozzle

The two-phase mass flow rate and the fluid temperatures at the broken cold leg are calculated with the downcomer annulus component described in (5). The pressure drop across the broken cold leg nozzle ΔP_{BCN} is the differential pressure between the top of the downcomer and the exit of the broken cold leg nozzle. A farily large ΔP_{BCN} was observed in CCTF and hence it does affect the overall system responses. The ΔP_{BCN} can be expressed by using the K-factor for the dynamic pressure drop of the two-phase mixture:

$$\Delta P_{BCN} = \{ \frac{1}{2} \cdot \rho_g \cdot u_g^2 \alpha + \frac{1}{2} \rho_\ell u_\ell^2 (1 - \alpha) \} K_{BCN} \quad , \qquad \text{(A-29)}$$

where the void fraction α, the vapor velocity u_g and the liquid velocity u_ℓ are given assuming the homogeneous flow with no slip:

$$\alpha = \frac{\rho_\ell W^o_{gA}}{\rho_\ell W^o_{gA} + \rho_g W^o_{\ell A}} \quad ,$$

$$u_\ell = \begin{cases} \dfrac{W^o_{\ell A}}{\rho_\ell \cdot \frac{\pi}{4} \cdot D_{BCN}^2 (1 - \alpha)} & (\alpha \neq 1) \\ 0 & (\alpha = 1) \end{cases} \qquad \text{(A-30)}$$

$$u_g = \begin{cases} \dfrac{W^o_{gA}}{\rho_\ell \cdot \frac{\pi}{4} \cdot D_{BCN}^2 \alpha} & (\alpha \neq 0) \\ 0 & (\alpha = 0) \end{cases}$$

and K_{BCN} is the K-factor of the broken cold leg nozzle. In the present code, the differential pressure across the broken cold leg includes all pressure losses between the top part of the downcomer and the containment (break point). This additional pressure loss is included in the K-factor K_{BCN}, which is the input of the code.

References in Appendix

(1) Sugimoto, J. et al.: JAERI-M 83-147, (1983).
(2) Akimoto, H.: Private communication.
(3) Bankoff, S.G., et al.: Presented at 7th Water Reactor Safety Research Information Meeting, Washington D.C. (1979).
(4) Iguchi, T., et al.: J. Nucl. Sci. Technol., 20[6], 453～466 (1983).
(5) Wilson, J.F., et al.: Trans. ANS, Vol. 5, 151, (1962).
(6) Murao, Y., et al.: J. Nucl. Sci. Technol., 19[9], 705～719 (1983).
(7) Waring, J.P., et al.: WCAP-8583, (1975).

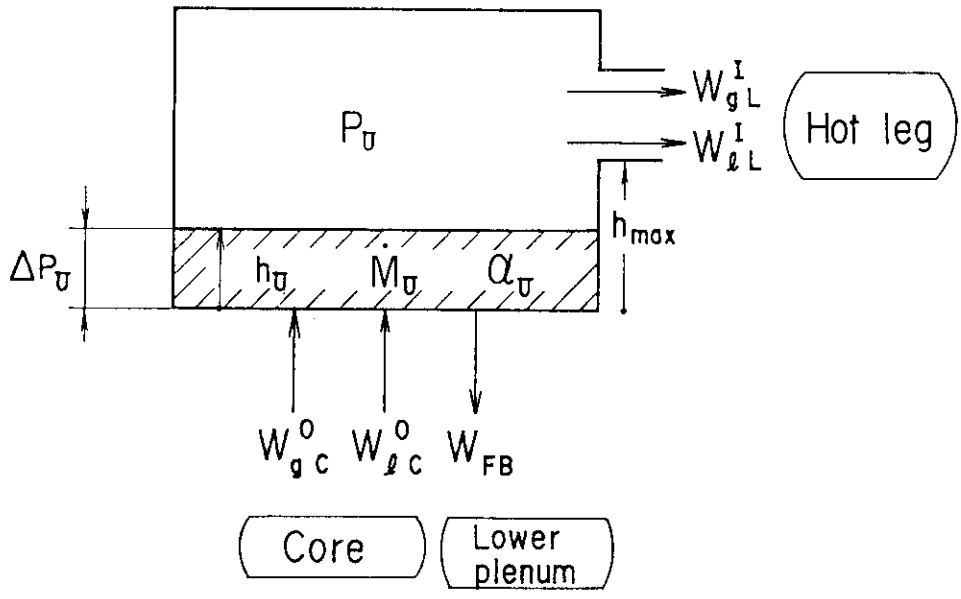

Fig. A.1 Schematic of upper plenum

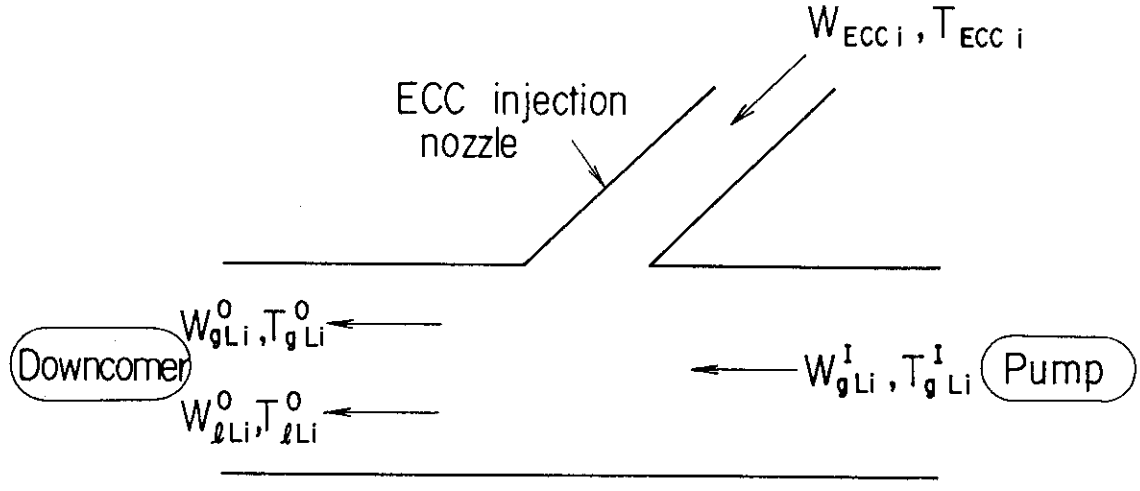

Fig. A.2 Schematic of ECC injection port

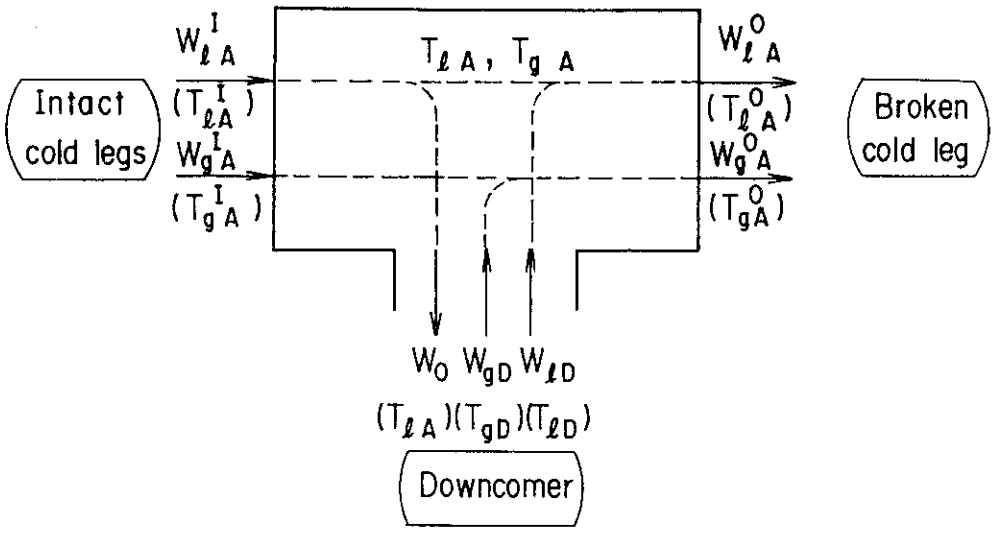

Fig. A.3 Schematic of upper annular port to downcomer

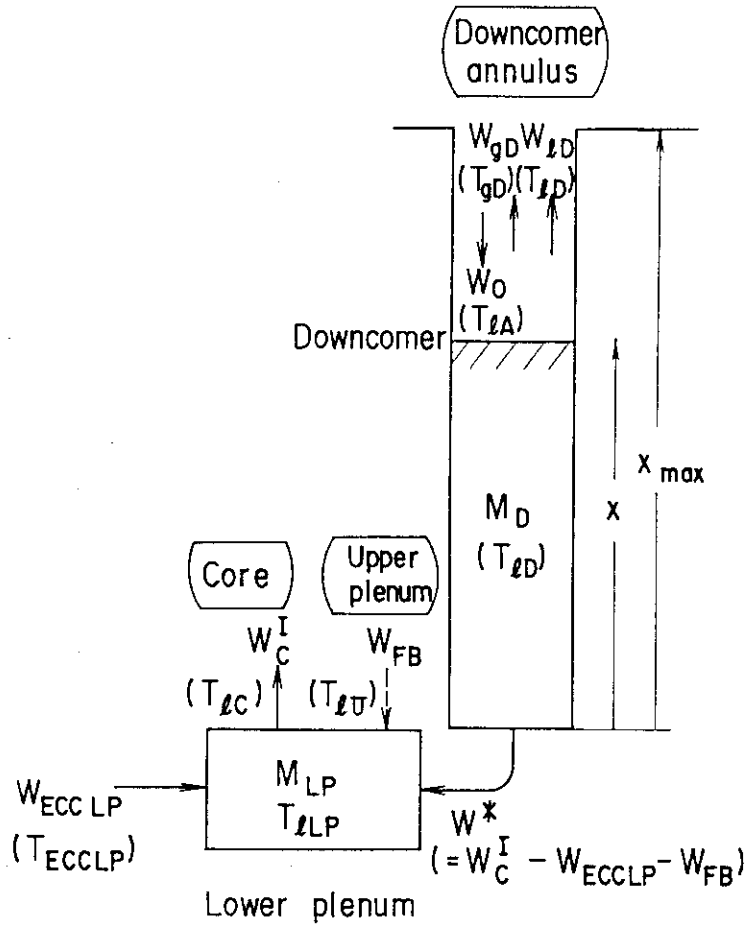

Fig. A.4 Schematic of downcomer and lower plenum